ALGERIAN DEMOCRATIC AND POPULAR REPUBLIC
MINISTRY OF HIGHER EDUCATION AND SCIENTIFIC RESEARCH

ABDELHAMID IBN BADIS UNIVERSITY - MOSTAGANEM
FACULTY OF SCIENCE AND TECHNOLOGY
DEPARTMENT OF ELECTRICAL ENGINEERING

THESIS

PRESENTED TO OBTAIN

LMD DOCTORATE DEGREE

Specialty: Electronics

Option: Electronics of Embedded Systems

By

MOULEBHAR Samia

PERFORMANCE ENHANCEMENT OF FLEXIBLE THIN-FILM ORGANIC SOLAR CELLS

Publicly defended on 14/05/2025 before the jury composed of:

Mr. HADRI Baghdad	Professor	Chair	UMAB - Mostaganem
Mr. CHOUIAH Abdelkader	Professor	Examiner	UMAB - Mostaganem
Mrs. RAHAL Wassila Leila	Professor	Examiner	UMAB - Mostaganem
Mr. BOUGUETAIA Tahar	M.C.A	Examiner	ESGE - Oran
Mrs. BENDENIA Chahrazed	M.C.A	Supervisor	UMAB - Mostaganem
Mrs. MERAD-DIB Hanaa	M.C.A	Co-Supervisor	UMAB - Mostaganem
Mrs. BENDENIA Souhila	Professor	Guest of honor	UMAB - Mostaganem

Academic Year: 2025-2026

Acknowledgement

I would like first and foremost to thank **Allah the Almighty**, who has always been with me in both the easy and difficult moments of life, granting me strength, patience, and perseverance throughout my journey.

This research work was carried out within two research laboratories**, Laboratory of Electromagnetism and Guided Optics and Analysis**, **Modeling, Advanced Materials for Renewable Energies Laboratory**, **University Abd El Hamid Ibn Badis**, **Mostaganem**.

I would like to express my deepest gratitude and sincere thanks to my supervisor, **Dr. BENDENIA Chahrazed**, for her continuous support, valuable guidance, and encouragement throughout the course of this work. Her scientific advice and constant availability were essential to the success of this thesis.

I also extend my warm appreciation to **Prof. HADRI Baghdad**, head of the doctoral program, for his trust, valuable guidance, and continuous encouragement throughout my doctoral studies.

My deepest thanks also go to him, in his role as **Chair of the jury**, for the honor of supervising this defense session and for the genuine interest he has shown in my work.

My special thanks go as well to my co-supervisors, **Prof. BENDENIA Souhila** and **Dr. MERAD-DIB Hanaa**, for their insightful advice, generous support, and kind encouragements that greatly contributed to the completion of this work.

I would like to express my sincere gratitude to the members of the jury who kindly accepted to evaluate my work and attend this defense.

I wish to offer my heartfelt thanks and deep appreciation to **Prof. CHOUIAH Abdelkader**, and **Prof. RAHAL Wassila Leila**, Professor at Abd El Hamid Ibn Badis University Mostaganem, also to **Dr. BOUGUETAIA Tahar**, Lecturer at ESGE Oran, who kindly agreed to examine and evaluate this work.

Their availability, scientific rigor, and insightful contributions have greatly improved this thesis. I am truly grateful to all of them. A very special thanks goes to **Prof. INANC Ibrahim**, Director of the **KITAM Laboratory at Ondokuz Mayis University (OMU)**, as well as to his PhD student **HUSSEIN BUSHIR Rakan**, and to **Prof. DEGE Necmi** and his PhD student **BERRIN POYRAZ Emine**, for welcoming me into their laboratory and for the great efforts they made to ensure the smooth progress of my internship. It was a real honor to work under their guidance and benefit from their knowledge and generosity.

I wish to thank my friend, **BENAHMEDI Lakhdar**, for his valuable help and support throughout my journey. My warm thanks also go to my dear friends, **Merabet Sarra**, **Sid Ahmed Khantar**, **Ali Aissani**, and all the others who stood by me with their encouragement and kindness, as well as to all my classmates from the **2023 promotion**.

Finally, I extend my sincere thanks to all those who, directly or indirectly, contributed to the realization of this work.

Dedication

To my beloved parents, for their endless love, their countless sacrifices, and the noble values they have instilled in me, which have guided and inspired me throughout this journey.

To my dear sisters, **Ibtissem**, **Fatima Zohra**, and **Nour El Imane**, for their kindness, encouragement, and comforting presence, in moments of doubt as well as in times of joy.

A special dedication to my cherished friend **Lakhdar Benahmedi**, for his invaluable professional and personal support, and for his sincere and unwavering friendship.

To my dear friends, **Mouna**, **Safaa**, **Manar**, **Amina**, and **Aida**, and to their beloved children, for the joy, encouragement, and warmth they have brought into my life.

To my dearest cousins, **Ines** and her little **Julia**, **Soufana**, **Khadidja**, **Bouchra**, **Hanane**, **Fadela**, **Rania**, **Amel**, **Amina**, and **Sarra**, whose affection and support have been a constant source of strength.

To my beloved aunts, **Halima**, **Djamila**, **Houria**, **Wissem**, **Lila**, **Saadia**, and **Houaria**, for their tenderness, prayers, and encouragement that have always accompanied me.

To my **whole family**, an invaluable support and a true pillar of my success.

Finally, to all those who, directly or indirectly, contributed to the completion of this work, I extend my deepest gratitude and profound respect**.**

Samia

Table Of Contents

Table of Contents

Chapter II

COMPUTATIONAL METHODS FOR DEVICE SIMULATION AND ML PREDICTIONS

Chapter III

SIMULATION AND OPTIMIZATION OF ORGANIC TANDEM SOLAR CELLS USING SCAPS-1D

Chapter IV

MACHINE LEARNING-GUIDED DESIGN OF DUAL ETLS FOR ORGANIC SOLAR CELLS

Chapter V

ORGANIC ELECTRONICS FOR EMBEDDED AND PORTABLE APPLICATIONS

Nomenclature

Nomenclature

Symbols	Meaning	Units
V_{OC}	Open-circuit voltage	V
J_{SC}	Short-circuit current density	mA/cm²
FF	Fill factor	%
η / PCE	Power conversion efficiency	%
R_S	Series resistance	Ω·cm² or Ω
R_{SH}	Shunt resistance	Ω·cm² or Ω
Eg	Bandgap energy	eV
χ	Electron affinity	eV
ε_r	Relative permittivity	– (dimensionless)
N_C, N_V	Effective density of states in conduction/valence bands	cm^{-3}
N_D, N_A	Donor/acceptor doping concentration	cm^{-3}
d	Layer thickness	nm or cm
μ_e, μ_h	Electron/hole mobility	$cm^2 \cdot V^{-1} \cdot s^{-1}$
τ_e, τ_h	Electron/hole lifetime	s
L_e, L_h	Diffusion length of carriers	cm
N_t	Trap density	cm^{-3}
Et	Trap energy level	eV
σn, σp	Electron/hole capture cross section	cm²
Sfront, Sback	Front/rear surface recombination velocity	cm/s
ΔEc (CBO)	Conduction band offset	eV
ΔEv (VBO)	Valence band offset	eV
ΦB	Metal–semiconductor barrier height	eV
Φwork	Electrode work function	eV
HOMO / LUMO	Highest occupied / lowest unoccupied molecular orbital	eV
QE(λ)	External quantum efficiency	%
SR(λ)	Spectral responsivity	A/W
α(λ)	Absorption coefficient	cm^{-1}
n(λ), k(λ)	Refractive index / extinction coefficient	– (dimensionless)
AM1.5G	Standard solar spectrum (100 mW/cm²)	W/cm²
T	Operating temperature	K or °C
Bias V	Applied voltage	V
C–V	Capacitance–Voltage	F/cm²
Admittance	AC admittance	S (Siemens)
MAE	Mean absolute error	– (numeric value)
RMSE	Root mean square error	– (numeric value)
MSE	Mean squared error	– (numeric value)
R^2	Coefficient of determination	– (0–1)
MAPE	Mean absolute percentage error	%
MPPT	Maximum Power Point Tracking	V, mA/cm², or mW/cm²
MOSFET (Q1)	Power transistor in DC-DC converter	A, V, W
L, C_0, C_1, D1	Inductor, capacitors, diode in DC–DC converter	H

List of Figures

CHAPTER I

CHAPTER II

CHAPTER III

CHAPTER IV

List of Tables

General Introduction

General Introduction

The global energy transition represents one of the major challenges of the 21st century, driven by the urgent need to reduce CO_2 emissions and mitigate the impact of climate change **[1,2]**. The gradual depletion of fossil fuels and the environmental consequences of their use have led to growing interest in renewable energies, which are emerging as an essential alternative. Among them, solar energy holds a central position due to its inexhaustible nature, worldwide availability, and steadily improving economic competitiveness **[1,3]**.

Today, crystalline silicon-based photovoltaic (PV) technologies dominate the market thanks to their technological maturity and high performance, achieving efficiencies exceeding 33% for tandem silicon/perovskite architectures. However, these devices require complex and costly manufacturing processes, rely on rigid substrates, and offer limited adaptability for lightweight or flexible applications **[4]**.

Organic solar cells (OSCs), classified as third-generation photovoltaic technologies, present unique advantages: light weight, mechanical flexibility, tunable transparency, compatibility with large-scale printing processes, and the use of non-toxic materials **[5]**. These characteristics pave the way for innovative applications such as wearable devices, smart textiles, and building-integrated photovoltaics (BIPV) **[6]**. Nevertheless, OSCs still face limitations, including lower efficiency than silicon cells, reduced lifetime, and sensitivity to degradation under real-world conditions. Recent advances, particularly the introduction of non-fullerene acceptors (NFAs) like Y6, have enabled laboratory efficiencies above 20%, especially in tandem or multilayer architectures**[7,8]**.

A particularly promising opportunity lies in coupling OSCs with low-power embedded systems. These autonomous sensors, smart labels, wearable medical devices, IoT modules require compact, lightweight, flexible, and efficient power sources, perfectly aligned with the properties of OSCs **[9]**. Direct integration of an organic photovoltaic (OPV) module into an embedded system can increase autonomy, or even make the application fully independent, without bulky batteries or external power cables **[10]**.

Improving OSC performance relies on several strategies: active layer engineering, optimization of selective transport layers (ETL, HTL), morphological control, and stable interface design. Artificial intelligence (AI) plays a key role in accelerating the design and optimization of OSCs, rapidly identifying optimal combinations of materials and architectures. Coupled with simulators like SCAPS-1D, AI can accurately predict device performance, significantly reduce development time and costs, and guide the engineering of new materials with targeted properties**[10,11]**.

Our objectives in this work are improve performances, stability and make OPVs ready for real use.

This thesis is organized into five chapters:

- ✓ **Chapter I**: Presents the fundamentals of solar cells, with an emphasis on the working principles, materials, and architectures specific to organic solar cells (OSCs), including their advantages, limitations, and recent technological trends.
- ✓ **Chapter II:** Describes the numerical methodology, combining the SCAPS-1D simulator with artificial intelligence (AI) techniques to accelerate optimization. It details the computational workflow, parameter selection, and machine learning algorithms used to identify optimal device configurations.
- ✓ **Chapter III:** Focuses on the optimization of a two-terminal polymer/polymer tandem solar cell, covering the design strategy, layer engineering, and the impact of material properties on performance.
- ✓ **Chapter IV:** Explores machine learning-based performance prediction for OSC architectures integrating dual organic/inorganic electron and hole transport layers (ETL/HTL). It analyzes training datasets, feature selection, and prediction accuracy, demonstrating AI's role in guiding material and structural choices.
- ✓ **Chapter V:** Reports an experimental demonstration of a flexible organic photovoltaic (OPV) panel designed to power a smartphone. This includes the fabrication steps, electrical characterization, and integration into a practical embedded system, highlighting real-world applicability and challenges in terms of stability and power management.

However, this work has some limitations: the results are mainly based on numerical simulations and do not fully account for long-term degradation phenomena; actual performance may differ from predictions; and integration into embedded systems with high load variability still requires additional research on electrical coupling (MPPT, voltage regulation, storage). These challenges constitute promising avenues for future research to improve the stability, efficiency, and adaptability of OSCs for widespread use in embedded systems.

Bibliography

[**1**] S. Esiner, J. Wang and R. A. J. Janssen, *Cell Rep Phys Sci*, 2020, 1, 100058.

[**2**] R. Verduci, V. Romano, G. Brunetti, N. Yaghoobi Nia, A. Di Carlo, G. D'Angelo and C. Ciminelli, *Adv Energy Mater*, DOI:10.1002/AENM.202200125.

[**3**] M. Hasanzadeh Azar, S. Aynehband, H. Abdollahi, H. Alimohammadi, N. Rajabi, S. Angizi, V. Kamraninejad, R. Teimouri, R. Mohammadpour and A. Simchi, *Photonics 2023, Vol. 10, Page 271*, 2023, 10, 271.

[**4**] P. Rafieipour, A. Mohandes, M. Moaddeli and M. Kanani, ntegrating transfer matrix method into SCAPS-1D for addressing optical losses and per-layer optical properties in perovskite/Silicon tandem solar cells," arXiv preprint arXiv:2308.01132, 2023.

[**5**] X. Zhou, W. Tang, P. Bi, Z. Liu, W. Lu, X. Wang, X. Hao, W. K. Wong and X. Zhu, *J Mater Chem C Mater*, 2019, 7, 380–386.

[**6**] J. Wang, Z. Zheng, P. Bi, Z. Chen, Y. Wang, X. Liu, S. Zhang, X. Hao, M. Zhang, Y. Li and J. Hou, *Natl Sci Rev*, DOI:10.1093/NSR/NWAD085.

[**7**] X. Du, T. Heumueller, W. Gruber, A. Classen, T. Unruh, N. Li and C. J. Brabec, *Joule*, 2019, 3, 215–226.

[**8**] X. Wan, C. Li, M. Zhang and Y. Chen, *Chem Soc Rev*, 2020, 49, 2828–2842.

[**9**] F. Yang, Y. Huang, Y. Li and Y. Li, *npj Flexible Electronics 2021 5:1*, 2021, 5, 1–12.

[**10**] J. C. Carrillo-Sendejas and J.-L. Maldonado, *APL Energy*, DOI:10.1063/5.0267160.

[**11**] J. Liang, X. Han, Y. Qiu, Q. Fang, B. Zhang, W. Wang, J. Zhang, P. M. Ajayan and J. Lou, *ACS Nano*, 2020, 14, 5426–5434.

CHAPTER I

Research Background

I.1 Introduction

Photovoltaic solar energy serves as a leading alternative solution in a global context characterized by the energy transition and the need for sustainable energy sources. This technology allows for the conversion of sunlight into electricity using photovoltaic cells and is garnering increasing interest due to its environmental and economic benefits.

This chapter first presents the generalities of photovoltaic energy. Particular attention is then given to organic photovoltaic cells, an emerging technology distinguished by its light weight, flexibility, and potential for low-cost manufacturing. We describe the different architectures and types of existing organic cells.

The key parameters for evaluating the performance of photovoltaic devices are then defined before focusing on organic semiconductors, essential materials in these devices.

Subsequently, the main challenges related to the efficiency, stability, and lifespan of organic photovoltaic cells are addressed. Finally, the chapter concludes with an exploration of the role and potential of organic photovoltaic cells in embedded systems, paving the way for innovative applications in fields such as portable electronics or the Internet of Things.

I.2 Solar Energy

Solar energy is an inexhaustible, free, and ubiquitous source of energy, emitted by the sun, a yellow dwarf star located at the center of our solar system. Composed mainly of hydrogen and helium, the sun has a mass equivalent to 330,000 times that of the Earth, representing 99.86% of the mass of the solar system by itself. Thanks to the nuclear fusion reactions that occur within it, it releases an immense amount of energy, a tiny fraction of which reaches the Earth. This energy can be harnessed in two main ways: solar thermal, which heats a liquid or gas for later use (domestic hot water, heating, etc.), and solar photovoltaic, which uses semiconductor cells to convert light into electricity. Although the efficiency of photovoltaic cells is lower than that of thermal systems, they allow for a broader range of uses (powering devices, transportation, etc.). Indeed, the sun sends more than 40,000 times the world's energy needs to Earth each year,

making it a promising solution to replace fossil fuels, especially at a time when their production is reaching a peak. Moreover, solar energy can be produced in a decentralized manner, making it accessible even in remote areas [1–3].

I.3 Solar Radiation

Solar irradiation refers to the amount of solar energy received per unit area in the form of electromagnetic radiation. Outside the Earth's atmosphere, this energy averages 1.37 kW/m². However, as it passes through the atmosphere, some of this radiation is absorbed or scattered by atmospheric components such as ozone, oxygen, and carbon dioxide, which reduces the intensity reaching the ground, generally around 1 kW/m² under optimal conditions. The thickness of the atmosphere traversed strongly influences this attenuation, and it is expressed by the air mass index, noted AM (Air Mass). This parameter varies according to the angle of incidence of the radiation, as shown in **Figure I.1**: AM0 corresponds to a situation without atmosphere (in space), AM1 to radiation arriving vertically on the Earth's surface, and AM1.5 to a more inclined angle, representing an atmospheric path 1.5 times longer. This last case, with an average power of about 827 W/m², serves as the standard reference for evaluating the performance of photovoltaic modules. Thus, ground irradiation varies according to several factors such as geographical location, time, sun inclination, and weather conditions. These spectra are presented in **Figure I.2** [1,4].

$$\mathbf{AM} = \frac{\mathbf{1}}{\cos \boldsymbol{\theta}} \qquad \textbf{(I.1)}$$

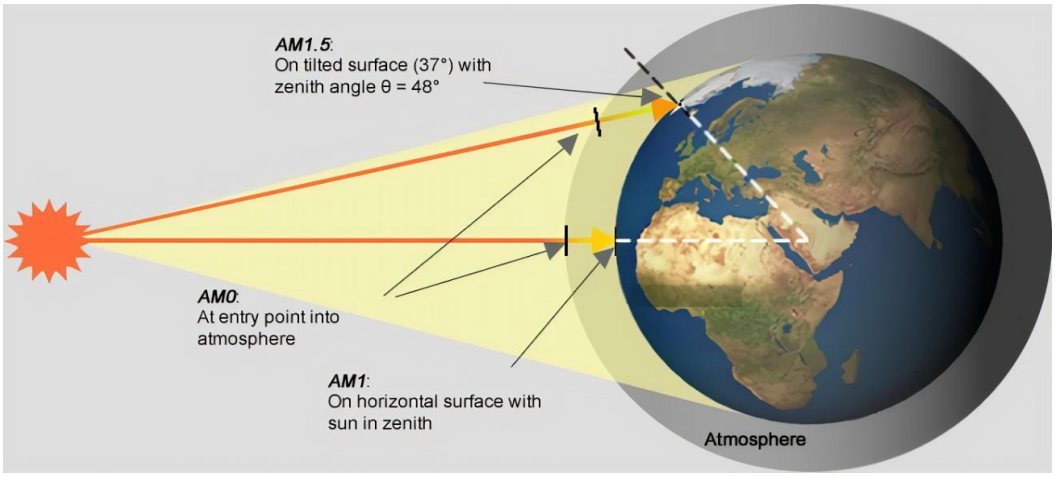

Figure I.1: Path of sunlight through the atmosphere under AM0, AM1, and AM1.5 conditions [5].

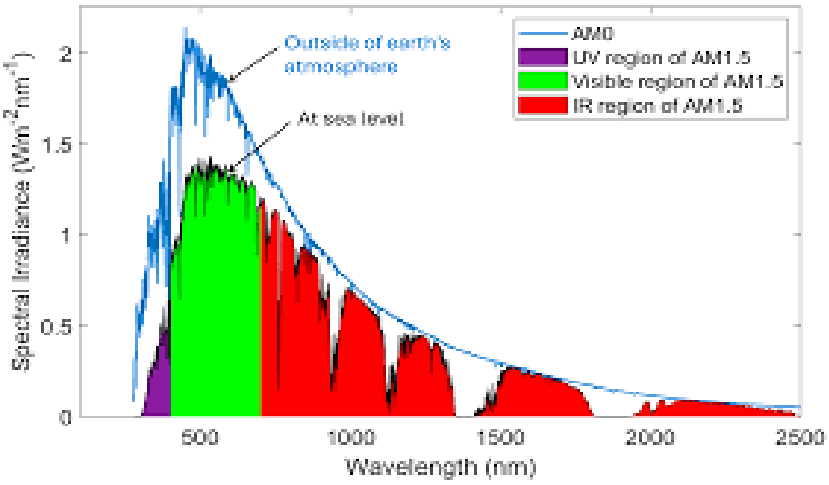

Figure I.2: Solar Spectrum Variation from Space to Earth's Surface [6].

I.4 Overview of Photovoltaic Technologies

The history of photovoltaic (PV) cells begins in the 19th century with the discovery of the photovoltaic effect by Becquerel. At the beginning of the 20th century, researchers like Einstein and Fritts contributed to improving this technology, although the initial efficiencies were very low. In the 1950s-60s, the needs related to space applications stimulated significant advances, reaching efficiencies of around 14%. The oil crisis of the 1970s rekindled interest in renewable energies, leading to significant improvements in materials and processes. Since the 2000s, the efficiency of photovoltaic cells has exceeded 25%, thanks to the introduction of new materials such as perovskites or quantum dots. In parallel, organic solar cells (OPV) have attracted interest since the early 20th century, particularly with the use of polymers as photoconductive materials. The first generations of OPV, in the 1970s–80s, exhibited efficiencies below 1%, but they paved the way for major innovations. In the 1990s, the introduction of new conjugated polymers and techniques such as solution processing made it possible to surpass the 4% efficiency mark. In the 21st century, the optimization of materials (perovskites, fullerene derivatives), architectures (tandem cells), and manufacturing processes has made it possible to achieve efficiencies approaching 20%. Although their efficiency remains lower than that of inorganic cells, OPVs stand out for their reduced cost, mechanical flexibility, and potential for large-scale production. In this context of constant evolution, it is important to highlight the diversity of photovoltaic technologies available on the market today. Mastering this technological classification proves

fundamental for decision-makers, investors, and users, as it allows for guiding strategic choices tailored to the specific needs in solar systems. An overview of this classification is presented in **Figure I.3** [4,7].

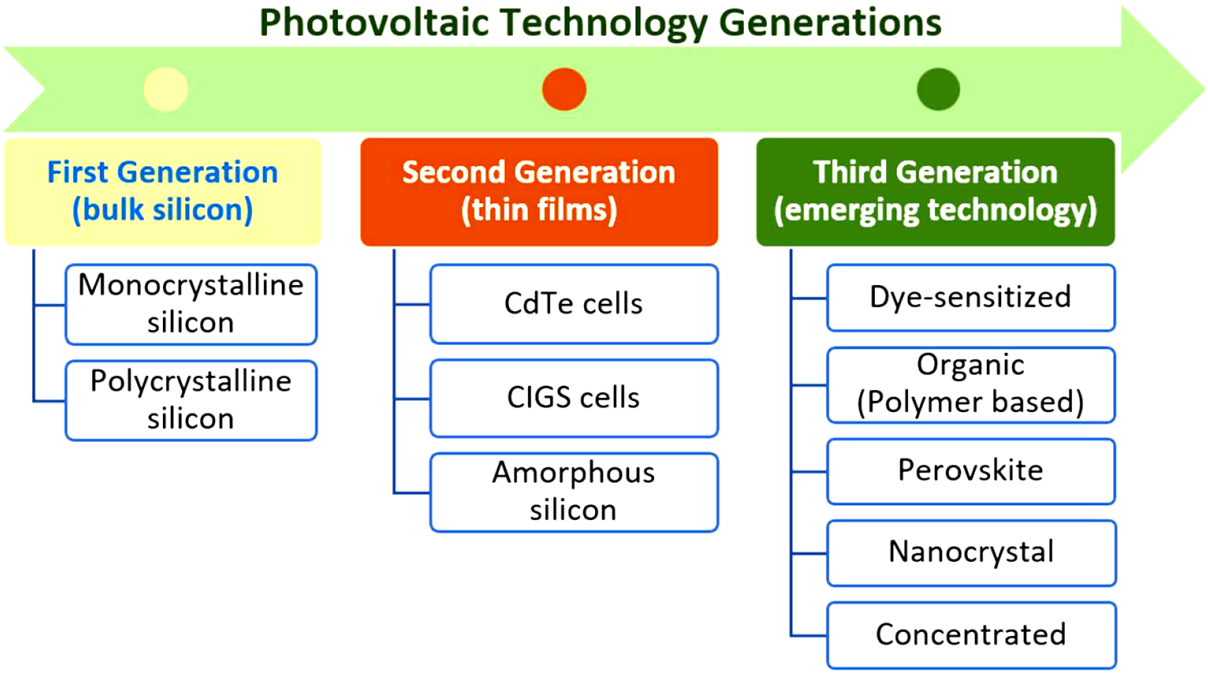

Figure I.3: Evolution of generations of photovoltaic cells [8].

I.4.1 First Generation

The first generation of photovoltaic cells includes traditional technologies based on inorganic semiconductors, mainly monocrystalline and polycrystalline silicon. Developed as early as the 1950s, these cells are now the most widespread on the market. Their operation is based on the use of silicon crystals obtained by cooling molten silicon, which are then cut into thin plates (wafers), doped, and interconnected to form the cell. Silicon, abundant in the Earth's crust and primarily extracted from sand, constitutes a widely available base material, but its transformation remains energy-intensive and costly, representing about 70% of the final cost of a module. In the laboratory, these cells have achieved energy conversion efficiencies of up to 27.6%, although commercially available panels rarely exceed 20% due to losses under real-world usage conditions, particularly in high heat. In theory, their maximum efficiency is limited to 33.7%, which drives researchers to explore avenues for improvement. Despite these

limitations, their technological maturity, reliability, and longevity make them a benchmark solution in the field of photovoltaics [1,4,7,8].

I.4.2 Second Generation

The second generation of photovoltaic cells relies on the use of thin-film semiconductor materials, developed with the aim of reducing production costs and diversifying applications. Unlike crystalline silicon-based cells, these technologies utilise materials with a direct bandgap, such as cadmium telluride (CdTe), copper-indium gallium-selenide (CIGS), amorphous silicon (a-Si), or CZTS ($Cu_2ZnSn(S,Se)_4$), thus allowing for more efficient light absorption with thicknesses on the order of a few micrometres. Their lightness, flexibility, and the possibility of continuous manufacturing (roll-to-roll) make them interesting solutions for mobile applications or building-integrated photovoltaics (BIPV). However, their efficiency generally remains between 10 and 15%, and their long-term stability still raises questions. Moreover, some technologies use rare or toxic materials (such as cadmium or indium), which limits their large-scale adoption, particularly due to environmental and regulatory considerations. Despite these challenges, their potential in terms of cost and versatility continues to attract the interest of research and industry [1,3,4,7,8].

I.4.3 Third Generation

The third generation of photovoltaic cells includes new technologies designed to exceed the efficiency limits set by earlier models, known as the Shockley-Queisser (SQ) limit, and to reach efficiencies estimated between 31% and 41%. These cells use advanced materials that optimize the absorption and conversion of solar energy. Among the main technologies of this generation, we find:

I.4.3.1 Quantum Dot (QD) Cells

These cells exploit quantum dot nanomaterials, which are zero-dimensional structures composed of transition metal elements. These quantum dots serve as a photoactive layer and can generate multiple electron-hole pairs from a single photon, thereby increasing energy conversion efficiency.

I.4.3.2 Dye-Sensitised Solar Cells (DSSC)

These cells work like artificial photosynthesis by using a dye to absorb light, which then activates electrons that move to electrodes and create electricity. Although they offer a maximum efficiency of around 13%, they stand out for their low cost and their ability to operate efficiently at various temperatures.

I.4.3.3 Perovskite Solar Cells

Perovskites represent the most recent innovation in this field, with efficiencies reaching up to 26.1%. These materials are promising for the future of solar energy, although their application is still limited to laboratory environments due to their relatively low stability.

I.4.3.4 Polymer-Based Solar Cells

These cells use plastic polymers, offering exceptional flexibility. Their operation is based on a donor-acceptor mechanism, where a polymer acts as an electron donor and fullerene acts as an acceptor. These cells have particular potential for integration into textiles, paving the way for new applications of solar energy.

Even though there are technical difficulties, especially with how stable perovskites are and the costs of making multi-junction cells, the third generation of photovoltaic cells, like organic photovoltaic cells (OPVs), shows good promise for creating solar energy that is more efficient and cheaper. These cells present enormous potential for applications ranging from large-scale installations to portable devices. In the following paragraphs, we will explore in detail organic photovoltaic cells, which are the subject of this study **[1,4,7,8]**.

I.5 State of Art of OPV

Organic photovoltaic cells (OPVs) are generating increasing interest as a promising alternative to traditional silicon-based photovoltaic technologies. Their development took a turn in 1986, when Tang and his team confirmed Merritt's predictions about the efficiency of structures composed of donor and acceptor materials. Originally, the structure used was planar, where the donor and acceptor layers were stacked separately. This idea then changed to a bulk heterojunction, where the materials are closely mixed in the active layer, leading to significant

conversion efficiencies of about 1% at that time, which have continued to improve. Various combinations of materials have been explored since then, including polymer/polymer, polymer/dye, and polymer/fullerenes. These cells offer several major advantages over inorganic cells: they are lightweight and flexible, can be manufactured on large surfaces using low-cost printing techniques, and are particularly suitable for portable applications.

OPVs are now available in several configurations, particularly depending on the architecture of the active layer, which is influenced by the nature and organization of the donor and acceptor materials **[9–11]**. The donor polymer – acceptor molecule configuration, historically dominated by fullerenes (PC61BM, PC71BM), has been modernized with the introduction of non-fullerene acceptors like ITIC or Y6, achieving record efficiencies of up to 19.6% (**Figure I.4)** for certain combinations such as PM6:D18:L8-BO **[9–11]**. The all-polymer configuration, appreciated for its flexibility and thermal stability, has achieved a yield of 17.2% thanks to the use of NDI/PDI-based acceptors, although it still suffers from miscibility issues **[12]**. The all-small-molecule configuration, offering better structural definition and reproducibility, has achieved yields close to 17%, but morphological stability remains a major challenge **[13]**.

Finally, the donor molecule–acceptor polymer configuration, still little explored, shows good thermal stability but remains limited in efficiency (~10%) due to the difficulty in finding compatible materials. Despite these advances, OPVs are still mostly in the research stage, as they suffer from certain limitations, notably a shorter lifespan compared to inorganic technologies and a difficulty in reproducing performance on a large scale. This is because the physical and chemical properties of organic materials, like molecular weight or regiorgularity, can vary, which affects the structure of the active layer. However, an optimal morphology, with a phase separation of about 10 to 20 nm, is crucial to ensure an efficient separation of photo-

generated charges and their transport to the electrodes. Thus, poor control of these parameters can harm the conversion efficiency[14–17].

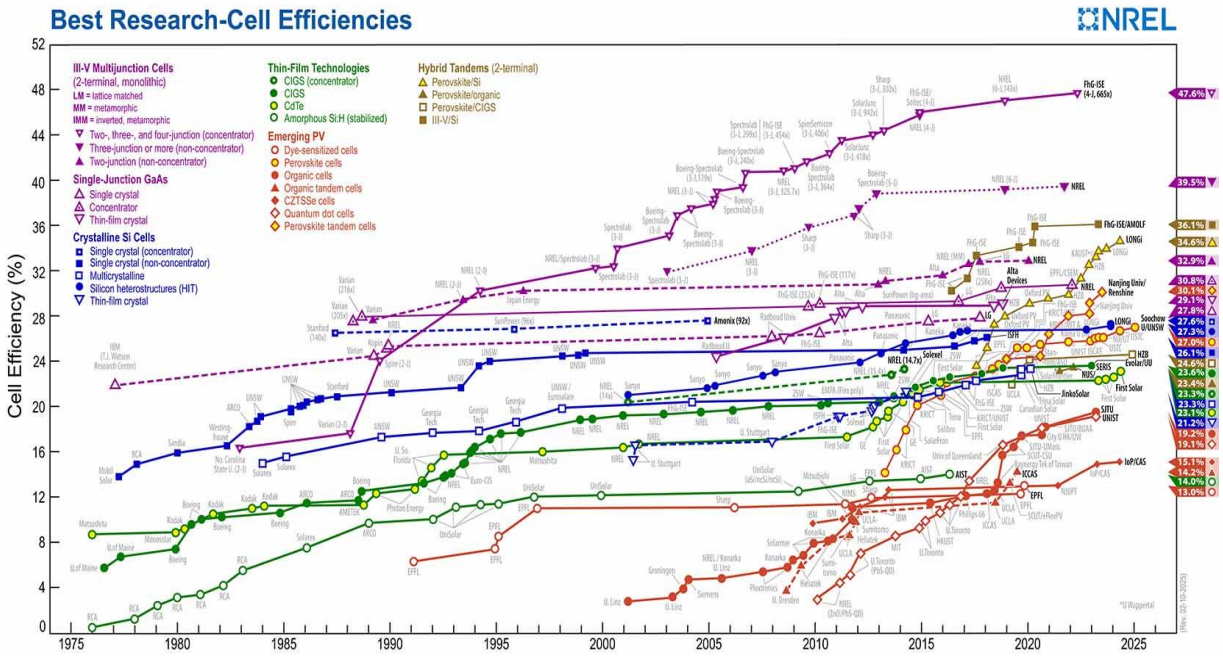

Figure I.4: NREL Best Research-Cell Efficiencies chart [18].

I.5.1 Organic Semiconductors

An organic semiconductor material is an organic compound that exhibits particular electronic and optical properties, primarily due to the conjugation of chemical bonds. This conjugation is manifested by a regular alternation of single and double bonds along the carbon chain, as in conjugated polymers, as shown in **figure I.5**. This molecular architecture allows electrons to move more freely, giving the material conductive or semi-conductive properties. These polymers are used in various applications such as organic electronics, photovoltaic cells, and electroluminescent diodes. They can be synthesised by polymerizing conjugated monomers or through post-polymerization modifications [19–21].

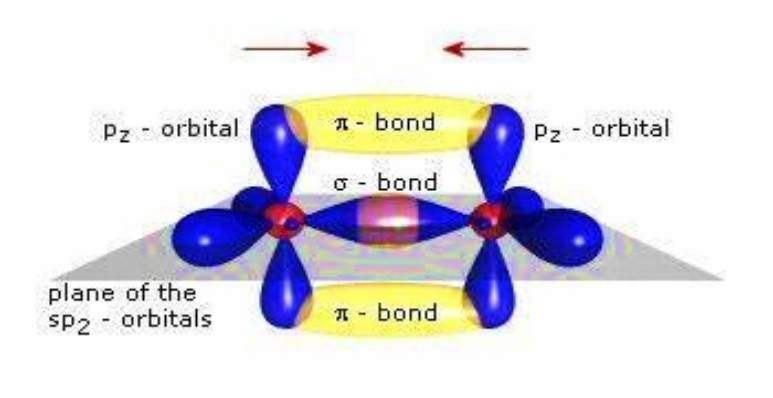

Figure I.5: Electronic structure of a carbon-carbon double bond **[22].**

I.5.1.1 Conduction mechanism in conjugated polymers

The fundamental element of these materials is carbon, which has four valence electrons (electronic configuration $2s^2\ 2p^2$). In conjugated structures, carbon atoms use sp^2 hybridization, where one 2s orbital and two 2p orbitals mix together to create three flat sp^2 hybrid orbitals. These form σ bonds with neighbouring atoms. The third 2p orbital (denoted p_z), perpendicular to the plane, participates in the formation of π bonds through lateral overlap with neighbouring pz orbitals.

The π electrons resulting from these overlaps can delocalise along the entire conjugated chain, thus creating a pathway for electrical conduction. Each double bond is therefore composed of a σ bond (strong and localised) and a π bond (weaker but delocalisable), the latter being responsible for the conductive properties of the polymer **[19–21]**. This process is illustrated in **Figure I.6.**

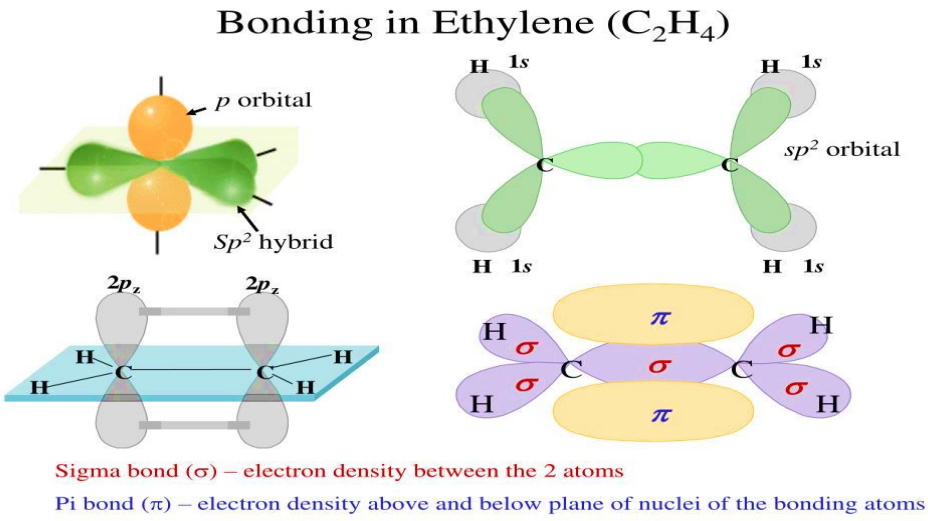

Figure I.6: Analysis of orbital overlap in the polyethylene polymer chain **[23].**

I.5.1.2 Band Model Applied to Conducting Organic Materials

An electron can move from the highest occupied molecular orbital (HOMO) to the lowest unoccupied molecular orbital (LUMO) if it receives enough energy to overcome the band gap (or energy gap, denoted Eg). This mechanism is fundamental for conduction in organic materials. The alternation of bonds promotes the formation of energy bands, resulting from the interaction between the π orbitals (HOMO band) and π* orbitals (LUMO band) (**Figure I.7**).

The valence band (HOMO) contains the electrons in the ground state, while the conduction band (LUMO) is empty but accessible by excitation. If the gap is narrow, electrons can easily jump into the conduction band and move, making the material conductive. On the other hand, a large gap, like in an insulator, prevents this transition. Conductive polymers are distinguished by partially filled or empty bands, which allow for electron mobility.

Moreover, according to their ability to donate or accept electrons, these materials are classified respectively as donors or acceptors. This complementarity is exploited in electronic devices such as organic photovoltaic cells, where the transfer of charges between donor and acceptor is the source of the electric current **[19–21]** .

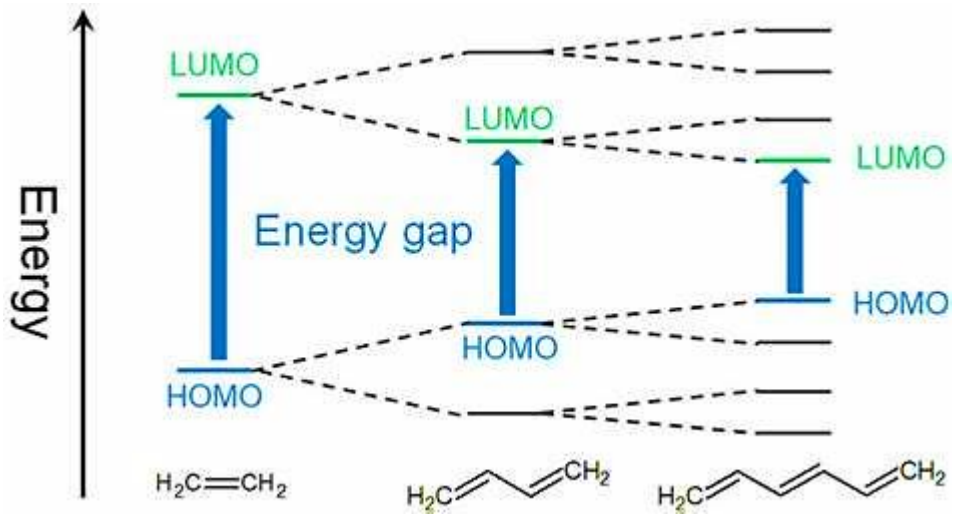

Figure I.7: Energy levels and band structure in organic semiconductors **[24].**

I.5.2 Key Steps in Conversion Process in OSCs

Organic photovoltaic cells (OPVs), considered a third-generation technology, are attracting increasing interest due to their advantages such as mechanical flexibility, light weight, and low cost of electrical energy production. These devices use organic molecules or conductive polymers that can convert solar energy directly into direct current using the photovoltaic effect. The architecture of these devices is similar to that of other emerging solar technologies, employing comparable charge transport layers (CTL) and metal contacts. However, their specificity lies in the photoactive layer, which in the case of OPVs, consists of conjugated polymers or fullerene/non-fullerene derivatives, enabling efficient light absorption and charge generation.

The working principle of bulk heterojunction (BHJ) devices, which represent the most common structure in OPVs, can be described through a few fundamental steps depict in **Figure I.8** **[25,26]**.

I.5.2.1 The Creation of Excitons

In organic solar cells (OSCs) starts when light is absorbed in the photoactive layer, which is made up of a blend of donor and acceptor semiconductor materials. Unlike inorganic semiconductors with continuous absorption, organic materials exhibit discontinuous absorption due to their intramolecular charge transfer properties, allowing them to selectively capture

photons over a wide spectral range. For this absorption to occur, the energy of the incident photon must be greater than the optical gap of the material. When a photon is absorbed, an electron from the HOMO (Highest Occupied Molecular Orbital) level of the donor is excited to its LUMO (Lowest Unoccupied Molecular Orbital) level, leaving behind a hole. This forms an exciton, an electron-hole pair bound by a strong Coulomb interaction (Frenkel-type exciton). Unlike Wannier–Mott-type excitons in inorganic semiconductors, these excitons do not dissociate spontaneously. To break apart, they need a boundary between donor and acceptor materials, where the difference in electronic affinity helps separate the charges, which is necessary for creating an electric current. Their dissociation requires an interface between donor and acceptor materials, where the gradient of electronic affinity effectively separates the charges, a crucial condition for generating an electric current. The efficiency of exciton dissociation in organic solar cells relies on their ability to quickly reach a donor/acceptor interface before disintegrating **[27–29]**.

I.5.2.2 The Exciton Diffusion

In organic solar cells, exciton dissociation efficiency depends on how fast the particles can reach a donor/acceptor interface before breaking down. As neutral quasi-particles of the Frenkel type, excitons move by a process called incoherent diffusion, which is often likened to molecular "hopping," and this movement lasts only a few hundred picoseconds. This movement restricts their journey to an average distance of 10 nm, called the exciton diffusion length. If excitons are generated too far from the interface, they risk recombining before being separated into free charges. That's why the bulk heterojunction (BHJ) structure, composed of a bi-continuous network of intimately mixed donor and acceptor materials, has emerged as an effective solution. It maximizes the available interface surface, thereby reducing the distance that excitons must travel to reach a dissociation point**[27–29]**.

I.5.2.3 The Dissociation of Excitons

in organic solar cells occurs at the interface between the donor and acceptor materials, where the exciton first transforms into a charge transfer (CT) state. At this stage, the electron is transferred from the LUMO level of the donor to that of the acceptor, forming an intermediate state in which the electron and the hole reside on different molecules but remain bound by

Coulomb attraction. The effective separation of these charges into free carriers (an electron and a hole) depends on the ability to overcome this attraction. This process is made possible by a sufficient energy offset between the LUMO levels of the donor and the acceptor, generally between 0.2 eV and 0.3 eV, a value necessary to overcome the binding energy of the exciton.

Moreover, the internal electric field generated by the electrodes with different work functions also promotes this dissociation. However, there is a competition between the dissociation of the CT state and its relaxation, called geminate recombination, where the electron and hole, originating from the same initial excitation, recombine before being separated. Thus, to ensure efficient dissociation, it is crucial to have adequate energy compatibility between the donor and acceptor materials, an essential condition to avoid charge losses and maximize photovoltaic conversion efficiency **[27–29]**.

I.5.2.4 Charge transport and collection

After excitons break apart into free charges (electrons and holes), these charges need to move quickly to their designated electrodes to create an electric current. This movement happens in the n-type organic materials (which accept electrons) for electrons and p-type materials (which donate holes) mainly through a process called "polaron hopping," where charges jump from one spot to another nearby. The movement of charges is influenced by the internal electric field, created by the difference in work function between the two electrodes, although diffusion can also contribute to it.

However, since thin films of organic semiconductors are often disordered, transport is prone to recombination losses. Charges can be trapped in deep energy states or in the tails of the density of states, leading to trap-assisted recombination. Moreover, when free electrons and holes meet again at the donor/acceptor interfaces, bimolecular recombination can occur. These

mechanisms are even more likely in the highly mixed regions near the electrodes, increasing charge losses.

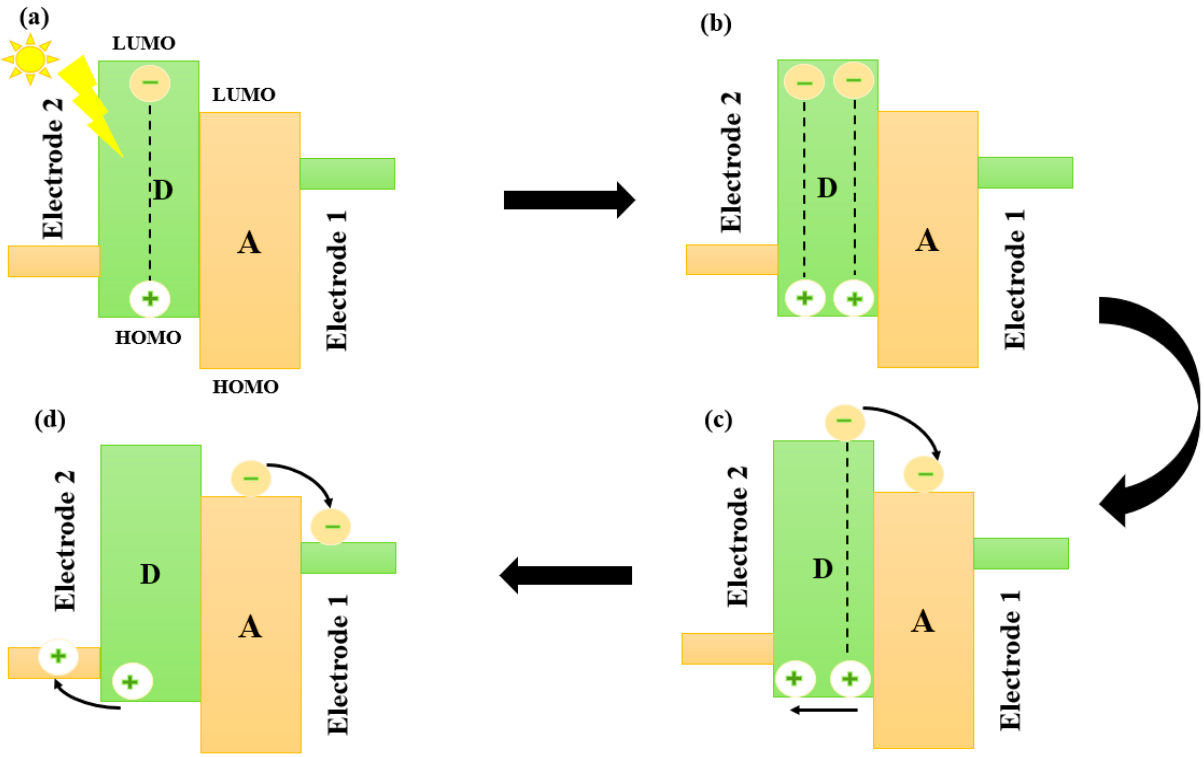

Figure I.8: Diagram of the photocurrent generation mechanism in organic solar cells (a) Exciton creation, (b) Exciton diffusion, (c) Exciton dissociation, (d) Charge collection.

Finally, if the carriers reach the electrodes without being recombined, they are extracted and collected: electrons at the cathode and holes at the anode. It is this final extraction that allows for the generation of the photocurrent when an external circuit is closed or when a voltage is applied. At this stage as well, losses can occur if a charge reaches the wrong electrode and recombines with a majority carrier. Effective transport and collection management is therefore essential to optimize the performance of organic solar cells **[27–29]**.

I.6 Circuit representation of solar cells

The equivalent circuit of solar cell is illustrated in **Figure I.9(a)**. This model, often used to represent inorganic solar cells, includes an ideal diode, a photogenerated current source (J_{ph}), as well as series (R_S) and parallel (R_{SH}) parasitic resistances. It allows for the description of the

basic electrical behaviors of the solar cell through the classical current-voltage equation **(equation I.2)** [30].

$$J = J_0 \left[\exp\left(\frac{e(V-JR_s)}{nk_BT}\right) - 1\right] + \frac{V-JR_s}{R_{sh}} - J_{ph} \quad \textbf{(I.2)}$$

However, this model is not suitable for organic solar cells (OSC) because it does not take into account several essential physical phenomena specific to these devices, namely:

- The formation and dissociation of geminate pairs (strongly bound excitons)
- The bimolecular recombination of charge carriers,
- The influence of interfacial layers playing critical roles in photon transmission, charge injection, and blocking,
- The effects of specific resistance in OSCs, highly dependent on the electric field and the morphology of the active material.

To overcome these limitations, a two-diode equivalent model has been proposed. This model, illustrated in **Figure I.9(b)**, introduces a second diode to more accurately represent the various recombination mechanisms:

- ✓ The first diode (D1) models the processes in the quasi-neutral region such as diffusion, drift current, and classical recombination.
- ✓ The second diode (D2) simulates recombination in the space charge region (or depletion layer), particularly Shockley–Read–Hall type recombination **[30–32]**.

This two-diode model gives a clearer picture **(equation I.3)** of how organic solar cells work electrically, especially when there is low injection, and helps us understand their current-voltage (J-V) characteristics better.

$$\mathbf{J = J_{ph} - \frac{V+JR_s}{R_{sh}} - J_{D1}\left[e^{B_1(V+JR_s)} - 1\right] - J_{D2}\left[e^{B_2(V+JR_s)} - 1\right]} \quad \textbf{(I.3)}$$

Where:

$$B_1 = \frac{q}{k_BT}, \quad B_2 = \frac{B_1}{n}$$

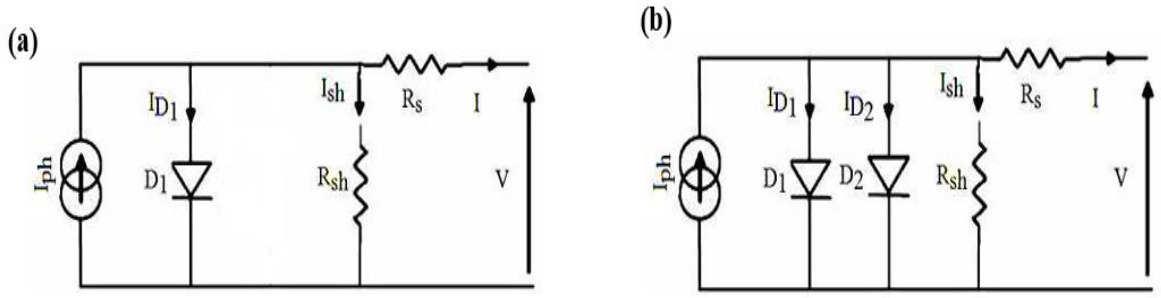

Figure I.9: (a) Single Diode equivalent circuit, (b) Two-diode electrical model of an organic solar cell **[30,33].**

I.7 Characteristic of Solar Cells

The performance of a solar cell is generally evaluated using four fundamental parameters: the open-circuit voltage (V_{OC}), the short-circuit current density (J_{SC}), the fill factor (FF), and the power conversion efficiency (PCE). These parameters, measured from current–voltage (J–V) curves, are interconnected and influenced by the physical, optical, and electronic properties of the materials used in the cell.

I.7.1 The open-circuit voltage (V_{OC})

Represents the maximum voltage that a solar cell can deliver when its terminals are open, that is, when no current is flowing. On the J–V curve **(Figure I.10(a))**, it corresponds to the point where the current density is zero. V_{OC} essentially depends on the energy difference between the HOMO (Highest Occupied Molecular Orbital) level of the donor material and the LUMO (Lowest Unoccupied Molecular Orbital) level of the acceptor material.

The greater this difference, the higher the V_{OC} can be. However, losses due to radiative or non-radiative recombination of electron-hole pairs reduce this voltage. Moreover, the quality of the interfaces between the electrodes and the charge transport layers plays a crucial role. Ohmic

and barrier-free contacts promote better charge transfer, which helps increase the V_{OC} **(Equation I.4)** **[31–34]**.

$$V_{OC} = \frac{mk_BT}{q} \ln\left(\frac{J_{ph}}{J_0} + 1\right) \quad \textbf{(I.4)}$$

I.7.2 The short-circuit current density (J_{SC})

Short-circuit current density is the current generated by the cell when it is short-circuited, that is, at zero voltage. It is directly related to the ability of the photoactive material to absorb light and generate electron-hole pairs. Several factors influence the J_{SC}, notably the bandgap of the active material: a smaller bandgap allows for the absorption of a larger portion of the solar spectrum. Similarly, a high absorption coefficient, an appropriate thickness of the active film, and a suitable morphology (ensuring effective phase separation between donor and acceptor) improve charge collection. Finally, a high mobility of charge carriers reduces recombination losses and ensures efficient transport of electrons and holes to the electrodes **[31–34]**.

I.7.3 The fill factor (FF)

Characterizes the quality of the J–V curve of the solar cell. It is defined as the ratio between the maximum power obtained (at the maximum power point, or MPP) and the product $J_{SC} \times V_{OC}$ **(equation I.5).** The FF reflects the efficiency of charge transport and the presence of internal resistive losses. In an ideal cell, the FF would be close to 100%, but in practice, it is limited by series resistances (which reduce the current) and shunt resistances (which short-circuit part of the voltage) **[31–34]**.

The FF can be improved by increasing the mobility of charge carriers, balancing the mobility of electrons and holes, and optimizing the interfaces between the different layers of the cell to reduce barriers to charge transport **[31–34]**.

$$FF = \frac{P_{max}}{V_{OC} \times J_{SC}} \quad \textbf{(I.5)}$$

I.7.4 The Power Conversion Efficiency (PCE)

The power conversion efficiency (PCE) is the key parameter that measures the overall efficiency of the cell. It is defined as the ratio between the maximum electrical power extracted from the cell and the incident luminous power **(equation I.6).** The efficiency therefore directly depends on the three previous parameters: J_{SC}, V_{OC}, and FF. The testing conditions (light intensity and spectrum), operating temperature, material stability, and cell architecture also affect it. To maximize efficiency, it is essential to design cells that combine excellent light absorption, efficient charge transport, and low recombination **[31–34]** .

$$\mathbf{PCE} = \frac{\mathbf{FF \times V_{OC} \times J_{SC}}}{\mathbf{P_{in}}} \qquad \mathbf{(I.6)}$$

$\mathbf{P_{in}}$ in $\mathbf{W/m^2}$represents the incident power received by the solar cell.

I.7.5 The External Quantum Efficiency

External Quantum Efficiency (EQE), also known as Incident Photon to Current Efficiency (IPCE) **(Figure I.10(b))**, is a key parameter for evaluating the performance of photovoltaic cells. It represents the fraction of incident photons converted into electrons collected by the electrodes at a given wavelength. In other words, the EQE measures the efficiency with which a cell converts incident light into electrical current.

This efficiency strongly depends on the wavelength, due to the specific absorption properties of the active materials used in the cell. To determine the EQE, the cell is illuminated with monochromatic light and the generated current is measured. Mathematically, the EQE at a wavelength λ can be expressed as the ratio of the spectral short-circuit current $J_{cc}(\lambda)$ and the spectral incident power $P_i(\lambda)$, according to the following **equation I.7** **[7,35,36]**.

$$\mathbf{EQE(\lambda)} = \frac{\mathbf{1240 \times} J_{cc}(\boldsymbol{\lambda})}{\boldsymbol{P_i(\lambda) \times \lambda}} \qquad \mathbf{(I.7)}$$

Where:

$(\mathbf{J_{cc}})$is in $\mathbf{A/cm^2}$, $(\mathbf{P_i})$ in $\mathbf{W/cm^2}$, and$(\boldsymbol{\lambda})$in $\mathbf{nm}$.

Measuring EQE across the whole solar spectrum (like AM1.5) helps accurately predict the maximum short-circuit current density of a solar cell, adding to what we learn from current-

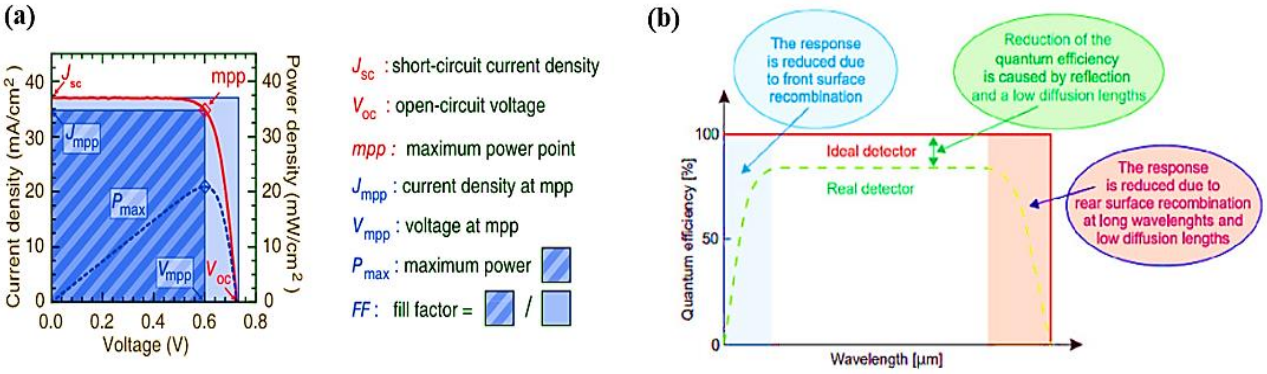

Figure I.10: (a) J-V curves and characteristic parameters of a photovoltaic cell, (b) External Quantum Efficiency **[24,37]**.

voltage (J–V) curves. This parameter is therefore essential for comparing the performance of different photovoltaic technologies.

I.8 The Architecture of an Organic Solar Cell

In general, there are two main architectures for organic solar cells (OSCs): the regular (or conventional) structure and the inverted structure. The essential difference between these two configurations lies in the order of the electrodes.

The regular (or conventional) structure of an organic solar cell, illustrated in **Figure I.11**, generally consists of five successive layers. First, a transparent anode made of indium tin oxide (ITO) allows for the collection of holes. Next, a hole transport layer (HTL) facilitates the injection of holes while blocking undesirable electrons. The active layer is made up of a uniform blend of a polymer that gives away electrons and an acceptor, which is usually made from fullerene or another type of n-type semiconductor. Then, an electron transport layer (ETL), typically made of calcium or lithium fluoride (LiF), is used to adjust the energy levels and optimize electron transport.

Finally, a metal cathode with a low work function, such as aluminum or a calcium/aluminum combination, effectively collects the generated electrons.

However, this structure has some drawbacks. For example, the PEDOT:PSS layer, often used as the HTL, can corrode the ITO electrode. Moreover, the vertical phase separation is not ideal: instead of the donor and acceptor materials distributing respectively towards the anode and cathode, the donor, having a lower surface energy, migrates towards the surface, resulting in an unfavorable distribution for a cathode located at the top of the structure.

Additionally, putting the cathode on top of the photoactive layer requires vacuum steps, which makes it difficult to use fully solution-based methods for large-scale production.

To overcome these limitations and improve the stability of the devices, the inverted structure was developed. In this configuration (i-OPV), the order of the layers is reversed, which avoids vacuum steps and facilitates large-scale manufacturing entirely through solution processing.

Inverted organic solar cells are particularly attractive due to their great stability, being able to remain functional for several days even without encapsulation. This longer-lasting performance is mainly because metal oxides (like zinc oxide or titanium oxide) are used as layers between materials, which are better than organic layers because they have helpful physical and chemical properties.

In addition to their better stability, inverted structures also offer greater flexibility and increased photocurrent. However, how well these devices work still relies a lot on the material

used for the ETL layer and how good its connection is with the active layer in a bulk heterojunction (BHJ) structure [35,38,39].

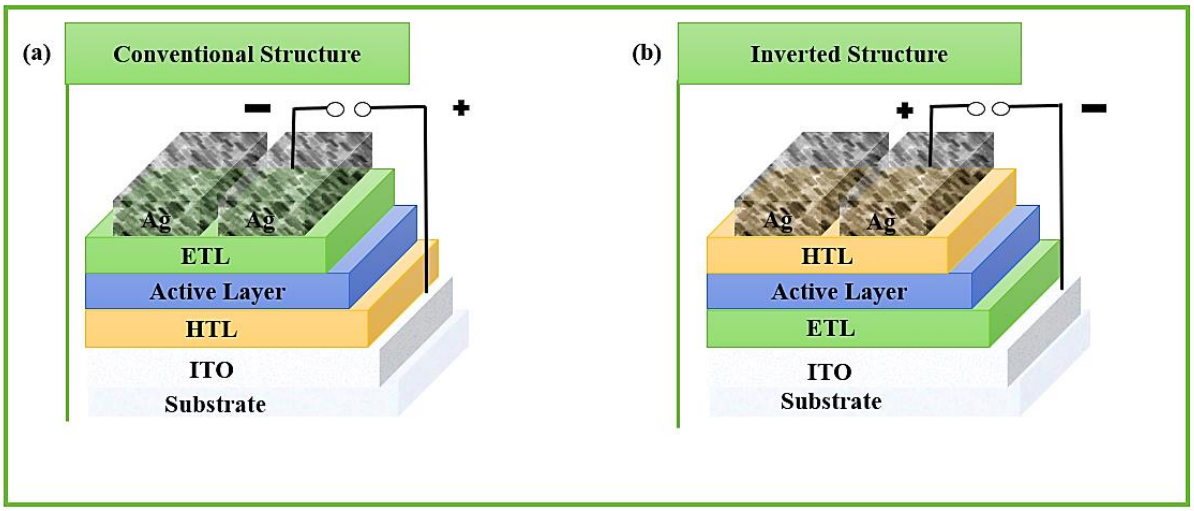

Figure I.1: (a) Conventional Structure, (b) Inverted Structure.

I.9 Structural conceptions of OSCs

I.9.1 Single layer

Single-layer organic photovoltaic cells represent the most basic architecture of OPV devices. They consist of a single layer of organic semiconductor material **(Figure I.12),** usually a polymer, deposited between two electrodes. One electrode makes a good connection with the active material, while the other creates a barrier that helps form an internal electric field, which helps break apart excitons. In some cases, the donor and acceptor materials can be mixed within the same layer, further simplifying the structure. Although this configuration allows for easy and low-cost manufacturing, it generally suffers from low conversion efficiencies due to less effective charge separation and limited absorption. Despite this, it remains a useful model for the fundamental study of photoelectric phenomena in organic materials [40].

I.9.2 Planar Heterojunction

The planar heterojunction (PHJ) structure, also known as a bilayer junction, consists of two stacked layers: one that donates electrons and another that accepts them **(Figure I.12),** creating a boundary where charge separation happens. When an exciton is generated in the

donor layer by light absorption, it must reach this interface to dissociate into an electron and a hole.

However, the short diffusion length of excitons (10–20 nm) limits the efficiency of this dissociation, especially if the layers are too thick. Although increasing the thickness improves light absorption, only a thin region near the interface actually contributes to photovoltaic conversion, which leads to recombination losses. Thus, despite its simplicity of fabrication, the PHJ structure is often less efficient than other more interpenetrated architectures like the BHJ **[40–42]**.

I.9.3 Bulk Heterojunction

The bulk heterojunction (BHJ) structure is a big improvement over the planar junction (PHJ) because it solves the problem of excitons not traveling very far. In this architecture, the donor and acceptor materials are mixed in solution and then deposited together **(Figure I.12),** forming an interpenetrating network that maximizes the D/A interface surface.

This three-dimensional structure promotes efficient charge separation and reduces recombination losses. Thanks to the constant proximity between the donor and acceptor domains, excitons are more likely to reach an interface before recombining.

BHJ cells can rely on binary blends, but the evolution of materials and formulation strategies has led to the emergence of ternary and even quaternary blends, combining multiple donors and acceptors. These multi-component systems exhibit complementary absorption spectra, allowing for better photon harvesting in the active layer while maintaining a relatively simple manufacturing process. They also aim to improve energy compatibility, optimize charge mobility, and widen the absorption window.

However, the performance of BHJ cells remains highly dependent on the manufacturing conditions, particularly the D:A ratio, the solvents used, and post-deposition treatments such as thermal annealing. Additionally, while the early BHJ cells used fullerene-type acceptors, their narrow range of light absorption prompted the creation of non-fullerene acceptors (NFAs), which make better use of sunlight and greatly enhance efficiency **[40,43,44]**.

I.9.4 Tandem

The limited range of light that single-junction organic photovoltaic (OPV) cells can absorb and the energy lost as heat are some of their biggest drawbacks. To address this, tandem solar cells (TSC) have been developed. These devices stack two or more sub-cells **(Figure I.12)**, each with a different bandgap, allowing for a more extensive use of the solar spectrum. High-energy photons are absorbed by the upper sub-cell with a wide bandgap, thereby reducing thermalization losses, while lower-energy photons pass through this first layer to be captured by a lower sub-cell with a narrow bandgap. Thus, each photon is optimally utilized according to its energy, significantly improving the overall efficiency.

Each sub-cell integrates an absorbing material capable of generating excitons, as well as transport materials to facilitate the separation and collection of charges. By using different light and electrical properties in the same design, tandem cells perform better than traditional structures while still being compatible with the low-cost production methods common in organic photovoltaics (OPVs) [33,45,46].

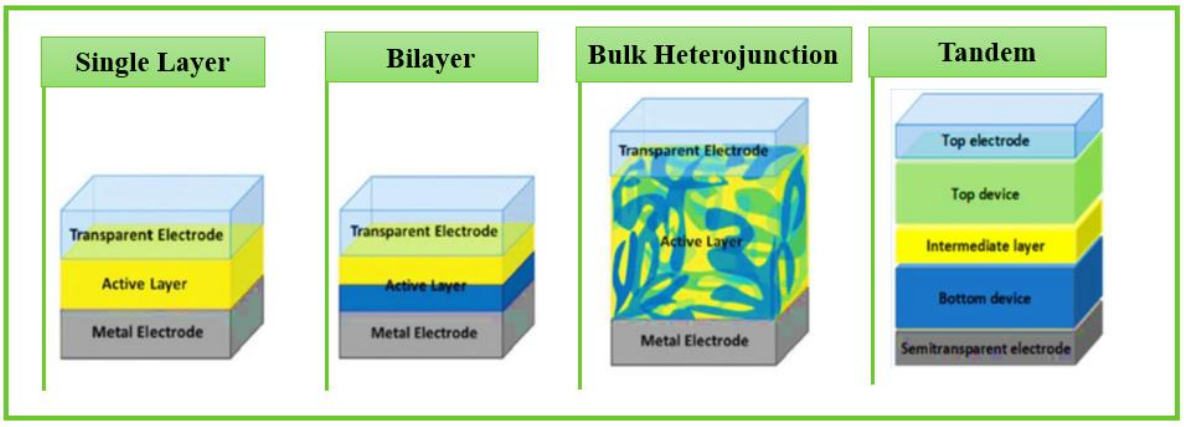

Figure I.2: The architecture of organic photovoltaic cells [33].

I.10 Functional Classification of Materials Used in OSCs

In the field of organic solar cells, the choice of materials for each functional layer is crucial for the performance and stability of the device. The materials used vary according to their specific role: light absorption, charge transport, electron or hole extraction, or even

encapsulation. Each of these materials has advantages that can be exploited according to the needs of the application, but also limitations that should be taken into account during the design. The following section summarizes these materials according to their function, specifying their category and a few examples, as well as their main advantages and disadvantages.

- **Active Layer**

The active layer is the core of the organic solar cell, responsible for light absorption and exciton generation. It typically consists of a blend of donor and acceptor materials. Common donor polymers such as P3HT and PBDB-T are valued for their flexibility, low cost, and compatibility with solution processing. However, they suffer from low charge mobility and photodegradation. On the acceptor side, fullerene derivatives like PCBM offer good electron mobility and chemical stability, yet they are expensive and have limited absorption across the solar spectrum. Non-fullerene acceptors (NFAs), such as Y6 and ITIC, enable broader spectral absorption and higher efficiency due to their tunable molecular structures. Nonetheless, they often require complex synthesis processes and their long-term stability remains under optimization.

- **Electron Transport Layer (ETL)**

The electron transport layer facilitates the extraction of electrons from the active layer to the cathode while blocking holes. Metal oxides such as ZnO and TiO_2 provide efficient electron extraction and excellent thermal stability. However, some require high-temperature processing and may introduce surface defects. Organic materials like PFN and BPhen are low-cost and compatible with low-temperature processing, although their long-term stability is limited. Small molecules like BCP offer well-defined energy levels and good interfacial compatibility, but are sensitive to oxygen and moisture. Conductive polymers such as PEIE are easily processed and cost-effective, but are also vulnerable to degradation by air and moisture.

- **Hole Transport Layer (HTL)**

The hole transport layer ensures efficient hole extraction to the anode and prevents electron leakage. PEDOT:PSS is widely used due to its high conductivity and optical transparency. However, its acidic and hygroscopic nature can corrode ITO and compromise stability. Metal oxides such as MoO_3 and V_2O_5 offer good hole injection and enhanced stability, but typically require vacuum deposition. Small molecules like Spiro-OMeTAD provide high efficiency and excellent hole mobility, though they are costly and their dopants are sensitive to moisture. Inorganic compounds such as NiO and CuSCN offer high thermal and chemical stability with potential for low-temperature processing, though their interfacial quality is sometimes difficult to control.

- **Cathode**

The cathode collects the electrons extracted by the ETL. Low work function metals such as Aluminum (Al) and Calcium (Ca) are commonly used due to their efficient electron extraction capability. However, these materials are prone to oxidation and degradation when exposed to air, which compromises device stability.

- **Anode**

The anode, usually made of a transparent conductive oxide like ITO or FTO, collects holes and allows light to pass through the device. These materials offer high transparency and electrical conductivity but are brittle (especially ITO), costly, and not ideal for flexible device applications.

I.11 Challenges of organic photovoltaics

To meet the industrial requirements of organic photovoltaics, it is essential to tackle a fundamental technological triptych **(Figure I.13)**, composed of:

- Efficiency
- Stability

- Manufacturing processes.

This triptych today represents one of the main challenges that organic solar cells (OSCs) must face. This triptych today represents one of the main challenges that organic solar cells (OSCs) must face.

Progress in each of these three areas is essential to enable the transition of OSCs from the laboratory to viable and competitive commercialization[16,47].

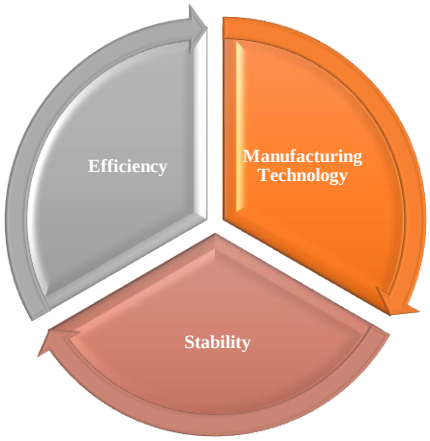

Figure I.3: Challenges of organic photovoltaics.

I.11.1 Stability of OSC

The issue of degradation and stability of organic solar cells (OSC) is particularly complex. These two parameters are essential criteria for evaluating the performance and durability of organic photovoltaic devices. Indeed, an efficient solar cell must not only exhibit good efficiency but also maintain its performance over time, despite environmental conditions.

I.11.2 The Degradation of an Organic Solar

The degradation of an organic solar cell refers to the gradual deterioration of its operational capacity. It is important to note that this deterioration does not always manifest as a direct chemical modification of the material structures; it can also be related to physical or morphological changes affecting the overall functioning of the device. To better understand and control these phenomena, researchers have structured their studies around two main categories of degradation:

I.11.2.1 Chemical Degradation

Several cases of degradation were identified and illustrated in **Figure I.14.**

- **The diffusion of oxygen (O_2) and water (H_2O) in organic photovoltaic devices:**

The infiltration of these environmental elements leads to undesirable reactions with the active materials, altering the performance of the cells.

- **The photochemical and photo-oxidation effects of polymers:**

Under the effect of light, particularly UV, polymers can degrade through oxidation, reducing their effectiveness.

- **The degradation caused by the preparation of the polymer:**

Defects or impurities resulting from the synthesis or treatment of polymers can promote their chemical instability.

- **Photo-oxidation occurs between polymer materials and inorganic oxide-type interfaces:**

At the interfaces with layers like ZnO or TiO_2, light induces oxidation reactions that deteriorate performance.

- **The chemical degradation of metallic electrodes:**

Metals (like aluminum) react with oxygen or moisture, causing corrosion or loss of conductivity.

- **The chemical degradation of the ITO (Indium Tin Oxide) electrode:**

This transparent material can undergo chemical corrosion, particularly in a humid atmosphere, affecting its transparency and conductivity.

The conductive polymer type PEDOT:PSS is responsible for the degradation of the interface layer. This polymer is sensitive to moisture, which can lead to a decrease in performance or reactions with nearby electrodes **[16,48–50]**.

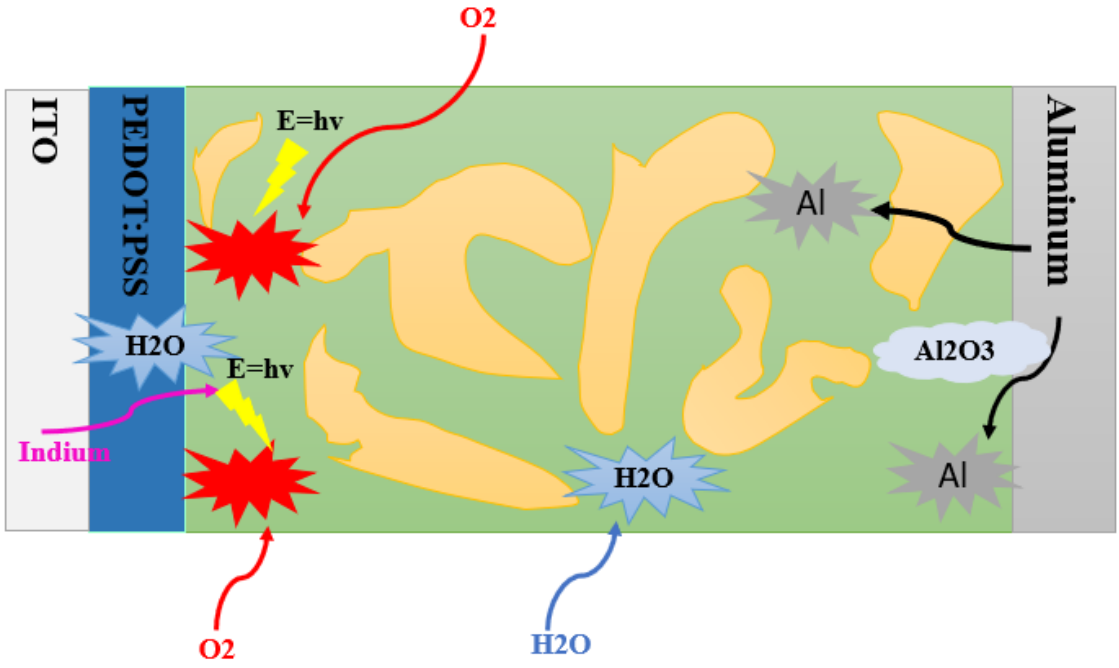

Figure I.4: Schematic illustration of chemical degradation.

I.11.2.2 Physical and Mechanical Degradation

Several instances of physical and mechanical degradation have also been described:

- **The thermal effects on controlling the morphology of the photoactive layer:**

Heat can cause a reorganization of the materials in the active layer, reducing the efficiency of charge transport.

- **The role of UV light in the morphological stability of the photoactive layer:**

UV light can destabilize the internal structure of the active layer by altering the arrangement of the polymeric domains.

- **The degradation caused by mechanical stresses applied to the organic device in the case of using a flexible substrate:**

Bending, stretching, or compressing can cause cracks or delamination, affecting the integrity and performance of the device **[1,16,48–50]**.

I.11.3 Efficiency

Among the main challenges related to organic solar cells (OSC), conversion efficiency is a major issue. Over time, numerous research efforts have been made to improve this performance. The first planar cells displayed modest efficiencies, in the range of 2 to 5%, although some optimizations allowed them to approach 8 to 9% under laboratory conditions. The introduction of the bulk heterojunction (BHJ) idea was a major improvement, raising the efficiency to 16% on small areas under standard testing conditions (AM1.5G).

Subsequently, the use of ternary and quaternary blends combining several types of donors and acceptors allowed for better management of light and charge transport, achieving efficiencies around 18 to 19% in experimental devices. More recently, developing tandem structures by stacking two complementary organic cells has allowed surpassing the 20% efficiency mark in the laboratory, marking a turning point in the evolution of OSCs. Thus, the efficiency targets set for organic photovoltaic cells now seem to be on track for achievement, particularly within the timeframe envisioned by the scientific community.

I.11.4 Manufacturing Techniques

Manufacturing techniques represent a major challenge in the development of organic solar cells (OSCs), still hindering their full commercialization. Although these devices offer numerous advantages, such as mechanical flexibility, lightweight, and low-cost manufacturing potential, their market deployment remains limited by the complexity and sensitivity of the manufacturing processes. The performance and stability of OSCs are closely dependent on mastering several critical steps, including material deposition, device architecture design, and encapsulation.

In particular, the quality of the deposited layers is essential: they must be continuous, uniform, defect-free, and have a precisely controlled thickness. Techniques such as spin-coating, blade coating, or roll-to-roll printing have been explored to meet these requirements, but they still have limitations in terms of reproducibility, large-scale yield, and durability. To enable large-scale commercial adoption of OSCs, it is essential to overcome these technical obstacles and develop more robust, stable, and industrially compatible manufacturing processes **[17,51]**. **Table I.1** and **Figure I.15** summarizes the manufacturing technique of OSCs.

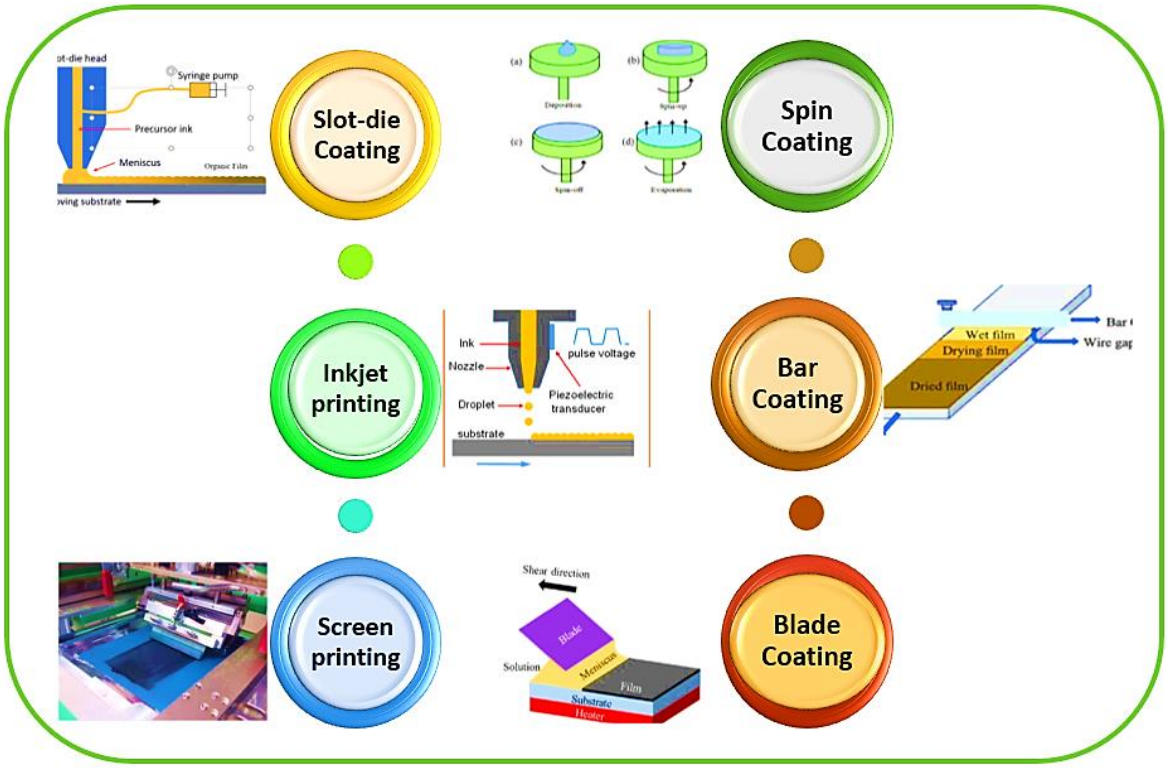

Figure I.15: Technologies for manufacturing organic solar cells.

Table I.1: Methods for Depositing Active Layers and Transport in Organic Devices: Advantages, Disadvantages, and Efficiency.

Method	Type	Description	Advantages	Drawbacks	PCE
Spin Coating	Batch	Solution deposited on a rotating substrate	Simple, fast, low material consumption	High material waste, not scalable	Up to **19%** [52,53]
Bar Coating	Roll-to-roll	Film deposited using a stainless steel rod	High speed (up to 600 m/min), good chemical resistance	Less precise than other techniques	**9.32%**
Blade Coating	Roll-to-roll	Film spread with a doctor blade	Good film control, scalable fabrication	Sensitive to external parameters, may require additional steps	Up to **16.35%** [54,55]
Slot-die Coating	Roll-to-roll	Deposition via a coating head with internal channel	Low material waste, good homogeneity, low contamination	More complex system	**15.6%** **17.2%** [56,57]
Inkjet Printing	Functional printing	Controlled drop-on-demand or continuous inkjet deposition	High precision, low ink consumption	Sensitive to ink viscosity, satellite droplet formation possible	**13.09%** [58]
Screen Printing	Functional printing	Ink pushed through a mesh (flat or rotary screen)	Suitable for non-active layers, stable process	Less suitable for active layers, limited precision	Used for transport layers

I.12 Organic Photovoltaic in Embedded System

An embedded system is an autonomous electronic device, generally designed to perform a specific task, integrating a microcontroller, sensors, actuators, and often communication modules. These systems are essential in various fields such as the Internet of Things (IoT), environmental monitoring, or wearable devices [59,60].

In this context, organic photovoltaic (OPV) technology represents a promising solution for the energy supply of these systems, thanks to its advantages in terms of flexibility, lightness, and reduced cost. Several studies have explored the integration of OPV into embedded systems. For example, Izidoro et al. presented a systematic review on OPV devices combined with electronic protection systems, highlighting the technical challenges related to stability and integration **[61]**. On their part, da Silva et al. developed an OPV self-powered system capable of harvesting ambient indoor light energy, thereby demonstrating the feasibility of such applications in low-light environments **[59]**. Finally, Dolara et al. proposed an embedded test bench for the real-time evaluation of OPV modules, highlighting the importance of integrated monitoring to optimize energy efficiency **[62]**.

Although the performance of OPVs is still inferior to that of inorganic cells, they already allow for the efficient powering of low-consumption components such as microcontrollers, sensors, and wireless modules. By possibly adding a way to store energy (like a battery or supercapacitor), these devices can work on their own, leading to eco-friendly, smart, and self-sufficient electronic systems.

I.13 Conclusion

This chapter has provided an overview of the fundamentals of photovoltaic energy, with a focus on organic cells, their architectures, materials, performances, and challenges. Their integration into embedded systems opens up intriguing prospects for flexible and sustainable applications.

Bibliography

[**1**] N.-F. CHALABI-épouse-YELLES-CHAOUCHE, Etude et simulation d'une cellule photovoltaïque organique à base du matériau organique OC1C10-PPV : PCBM ,2020.

[**2**] A. D. Becke, *J Chem Phys*, 1993, 98, 5648–5652.

[**3**] M. N. Arshad, M. Khalid, M. Asad, A. A. C. Braga, A. M. Asiri and M. M. Alotaibi, *ACS Omega*, 2022, 7, 11631–11642.

[**4**] H. L. ح. لموفق, Study of the electro-optical properties of nanostructured inorganic solar cells with an ultra-thin absorber layer, 2024.

[**5**] An Energy Primer for the AP Environmental Science Student - Sue O'Bannon | Bibliothèque | Formatif, https://app.formative.com/library/62040a296e16ac00e301ce2f, (accessed 8 May 2025).

[**6**] I. Visa, A. Duta, M. Moldovan, B. Burduhos and M. Neagoe, *Green Energy and Technology*, 2020, 59–158.

[**7**] C. BENDENIA, etude et simulation des proprietes electriques et optiques des cellules photovoltaiques organiques multicouches ,2019.

[**8**] E. K. Solak and E. Irmak, *RSC Adv*, 2023, 13, 12244–12269.

[**9**] Y. Lin, J. Wang, Z. G. Zhang, H. Bai, Y. Li, D. Zhu and X. Zhan, *Advanced Materials*, 2015, 27, 1170–1174.

[**10**] W. Ma, C. Yang, X. Gong, K. Lee and A. J. Heeger, *Adv Funct Mater*, 2005, 15, 1617–1622.

[**11**] L. Zhu, M. Zhang, J. Xu, C. Li, J. Yan, G. Zhou, W. Zhong, T. Hao, J. Song, X. Xue, Z. Zhou, R. Zeng, H. Zhu, C. C. Chen, R. C. I. MacKenzie, Y. Zou, J. Nelson, Y. Zhang, Y. Sun and F. Liu, *Nature Materials 2022 21:6*, 2022, 21, 656–663.

[**12**] R. Sun, W. Wang, H. Yu, Z. Chen, X. X. Xia, H. Shen, J. Guo, M. Shi, Y. Zheng, Y. Wu, W. Yang, T. Wang, Q. Wu, Y. (Michael) Yang, X. Lu, J. Xia, C. J. Brabec, H. Yan, Y. Li and J. Min, *Joule*, 2021, 5, 1548–1565.

[**13**] J. Qin, Z. Chen, P. Bi, Y. Yang, J. Zhang, Z. Huang, Z. Wei, C. An, H. Yao, X. Hao, T. Zhang, Y. Cui, L. Hong, C. Liu, Y. Zu, C. He and J. Hou, *Energy Environ Sci*, 2021, 14, 5903–5910.

[**14**] O. Almora, D. Baran, G. C. Bazan, C. Berger, C. I. Cabrera, K. R. Catchpole, S. Erten-Ela, F. Guo, J. Hauch, A. W. Y. Ho-Baillie, T. J. Jacobsson, R. A. J. Janssen, T. Kirchartz, N. Kopidakis, Y. Li, M. A. Loi, R. R. Lunt, X. Mathew, M. D. McGehee, J. Min, D. B. Mitzi, M. K. Nazeeruddin, J. Nelson, A. F. Nogueira, U. W. Paetzold, N. G. Park, B. P. Rand, U. Rau, H. J. Snaith, E. Unger, L. Vaillant-Roca, H. L. Yip and C. J. Brabec, *Adv Energy Mater*, DOI:10.1002/AENM.202002774.

[**15**] O. Almora, G. C. Bazan, C. I. Cabrera, L. A. Castriotta, S. Erten-Ela, K. Forberich, K. Fukuda, F. Guo, J. Hauch, A. W. Y. Ho-Baillie, T. J. Jacobsson, R. A. J. Janssen, T. Kirchartz, R. R. Lunt, X. Mathew, D. B. Mitzi, M. K. Nazeeruddin, J. Nelson, A. F. Nogueira, Ulrich. W. Paetzold, B. P. Rand, U. Rau, T. Someya, C. Sprau, L. Vaillant-Roca and C. J. Brabec, *Adv Energy Mater*, 2025, 15, 2404386.

[**16**] É. D. Mathématiques, M. A. Colsmann, : M Aziz Dinia and : M Thomas Heiser, DOI:10.34894/VQ1DJA ,2015.

[**17**] J. Majhi, S. Ghosh, K. Priya, S. Sharma and A. Bandyopadhyay, *Next Materials*, 2025, 8, 100595.

[**18**] Best Research-Cell Efficiency Chart | Photovoltaic Research | NREL, https://www2.nrel.gov/pv/cell-efficiency, (accessed 8 May 2025).

[**19**] A. G. S. Al-Azzawi, S. B. Aziz, E. M. A. Dannoun, A. Iraqi, M. M. Nofal, A. R. Murad and A. M. Hussein, *Polymers 2023, Vol. 15, Page 164*, 2022, 15, 164.

[**20**] M. Heydari Gharahcheshmeh and K. K. Gleason, *Energies 2022, Vol. 15, Page 3661*, 2022, 15, 3661.

[**21**] A. R. Murad, A. Iraqi, S. B. Aziz, S. N. Abdullah and M. A. Brza, *Polymers 2020, Vol. 12, Page 2627*, 2020, 12, 2627.

[**22**] (PDF) Thesis - Toward the organic laser diode, https://www.researchgate.net/publication/267103687_Thesis_-_Toward_the_organic_laser_diode, (accessed 8 May 2025).

[**23**] S. Arya and P. Mahajan, *Solar Cells*, 2023, 101–130.

[**24**] (PDF) Development of Simplified In Situ Processing Routes for Rear-Side Patterning of Silicon Heterojunction Interdigitated Back Contact (SHJ-IBC) Solar Cells, https://www.researchgate.net/publication/331023989_Development_of_Simplified_In_Situ_Processing_Routes_for_Rear-Side_Patterning_of_Silicon_Heterojunction_Interdigitated_Back_Contact_SHJ-IBC_Solar_Cells, (accessed 8 May 2025).

[**25**] A. G. S. Al-Azzawi, S. B. Aziz, E. M. A. Dannoun, A. Iraqi, M. M. Nofal, A. R. Murad and A. M. Hussein, *Polymers 2023, Vol. 15, Page 164*, 2022, 15, 164.

[**26**] L. Velasco Davoise, A. M. Díez-Pascual and R. Peña Capilla, *Materials 2022, Vol. 15, Page 1171*, 2022, 15, 1171.

[**27**] R. Alkarsifi, J. Ackermann and O. Margeat, *Journal of Metals, Materials and Minerals*, 2022, 32, 1–22.

[**28**] J. Jing, Y. Dou, S. Chen, K. Zhang and F. Huang, *eScience*, 2023, 3, 100142.

[**29**] Y. Dong, *Transactions on Environment, Energy and Earth Sciences*, 2024, 2, 10–17.

[**30**] B. Qi and J. Wang, *J Mater Chem*, 2012, 22, 24315–24325.

[**31**] M. Ghorab, A. Fattah and M. Joodaki, *Optik (Stuttg)*, 2022, 267, 169730.

[**32**] 2017, 310–333.

[**33**] N. Shah, A. A. Shah, P. K. Leung, S. Khan, K. Sun, X. Zhu and Q. Liao, *Processes 2023, Vol. 11, Page 1852*, 2023, 11, 1852.

[**34**] A. V. Mumyatov and P. A. Troshin, *Energies 2023, Vol. 16, Page 1924*, 2023, 16, 1924.

[**35**] A. V. Mumyatov and P. A. Troshin, *Energies 2023, Vol. 16, Page 1924*, 2023, 16, 1924.

[**36**] R. Ilmi, H. Al-Sharji and M. S. Khan, *Top Curr Chem*, 2022, 380, 1–38.

[**37**] N. Ali, S. Attique, A. Rahimi-Iman, S. Ali, F. Akram, N. Dai and H. Wu, *Sustainable Materials and Technologies*, 2023, 38, e00759.

[**38**] L. Velasco Davoise, A. M. Díez-Pascual and R. Peña Capilla, *Materials 2022, Vol. 15, Page 1171*, 2022, 15, 1171.

[**39**] T. Paula, M. de F. Marques, T. Paula and M. de F. Marques, *AIMS Energy 2022 1:149*, 2022, 10, 149–176.

[**40**] E. K. Solak and E. Irmak, *RSC Adv*, 2023, 13, 12244–12269.

[**41**] W. Abdelaziz, A. Zekry, A. Shaker and M. Abouelatta, *Solar Energy*, 2020, 211, 375–382.

[**42**] J. Jing, Y. Dou, S. Chen, K. Zhang and F. Huang, *eScience*, 2023, 3, 100142.

[**43**] K. N'Konou, S. Y. Kim and N. Y. Doumon, *Carbon Energy*, 2024, 6, e579.

[**44**] J. Wang, Z. Xie and J. T. W. Yeow, *ECS Journal of Solid State Science and Technology*, 2020, 9, 105004.

[**45**] M. B. Salim, R. Nekovei and R. Jeyakumar, *Solar Energy*, 2020, 198, 160–166.

[**46**] F. Yang, D. W. Kang and Y. S. Kim, *Solar Energy*, 2017, 155, 552–560.

[**47**] gopal gupta, priyanka Kumari, sonam Gupta, G. kumari, R. upadhyay and gopal gupta, DOI:10.20944/PREPRINTS202405.1591.V1.

[**48**] J. Wachsmuth, A. Distler, D. Deribew, M. Salvador, C. J. Brabec and H. J. Egelhaaf, *Adv Eng Mater*, 2023, 25, 2300595.

[**49**] S. Y. Kim, C. C. F. Kumachang and N. Y. Doumon, *Solar RRL*, 2023, 7, 2300155.

[**50**] E. çetin Yilmaz, M. K. Yeşilyurt, I. V. öner, G. ömeroğlu and A. N. özakin, *Periodicals of Engineering and Natural Sciences*, 2017, 5, 152–160.

[**51**] gopal gupta, priyanka Kumari, sonam Gupta, G. kumari, R. upadhyay and gopal gupta, DOI:10.20944/PREPRINTS202405.1591.V1.

[**52**] L. Kong, Z. Zhang, N. Zhao, Z. Cai, J. Zhang, M. Luo, X. Wang, M. Chen, W. Zhang, L. Zhang, Z. Wei and J. Chen, *Adv Energy Mater*, 2023, 13, 2300763.

[**53**] Z. Liu, M. Zhang, L. Zhang, S. Y. Jeong, S. Geng, H. Y. Woo, J. Zhang, F. Zhang and X. Ma, *Chemical Engineering Journal*, 2023, 471, 144711.

[**54**] Y. Cho, B. Lee, S. Jung, S. Jeong, J. Park, G. Park, S. Yang and C. Yang, *Energy Environ Sci*, 2023, 16, 6035–6045.

[**55**] J. Zhang, L. Zhang, X. Wang, Z. Xie, L. Hu, H. Mao, G. Xu, L. Tan and Y. Chen, *Adv Energy Mater*, 2022, 12, 2200165.

[**56**] H. Zhao, B. Lin, J. Xue, H. B. Naveed, C. Zhao, X. Zhou, K. Zhou, H. Wu, Y. Cai, D. Yun, Z. Tang and W. Ma, *Advanced Materials*, 2022, 34, 2105114.

[**57**] H. Zhao, H. B. Naveed, B. Lin, X. Zhou, J. Yuan, K. Zhou, H. Wu, R. Guo, M. A. Scheel, A. Chumakov, S. V. Roth, Z. Tang, P. Müller-Buschbaum and W. Ma, *Advanced Materials*, 2020, 32, 2002302.

[**58**] X. Chen, R. Huang, Y. Han, W. Zha, J. Fang, J. Lin, Q. Luo, Z. Chen and C. Q. Ma, *Adv Energy Mater*, 2022, 12, 2200044.

[**59**] E. A. D. ; Silva, W. M. C. ; Filho, M. R. ; Cavallari, J. Ando, E. Andrade Da Silva, W. Moreira, C. Filho, M. R. Cavallari, O. Hideo and A. Junior, *Electronics 2024, Vol. 13, Page 2518*, 2024, 13, 2518.

[**60**] M. Jahandar, S. Kim and D. C. Lim, *ChemSusChem*, 2021, 14, 3449–3474.

[**61**] C. L. Izidoro, W. M. C. Filho, M. R. Cavallari and O. H. A. Junior, *Brazilian Archives of Biology and Technology*, 2024, 67, e24230786.

[**62**] A. Dolara, A. Cabrera-Tobar, E. Ogliari, S. Leva and L. Hanne, *Electronics 2024, Vol. 13, Page 3104*, 2024, 13, 3104.

CHAPTER II

COMPUTATIONAL METHODS FOR DEVICE SIMULATION AND ML PREDICTIONS

II.1 Introduction

In the context of advanced research in electronics and renewable energy, numerical simulation methods and machine learning (ML) techniques play a central role in the analysis, optimization, and prediction of device performance. The simulation of devices, using specialized software such as SCAPS-1D, allows for the precise modelling of solar cell behavior by solving fundamental physical equations while reducing the need for costly and time-consuming experiments.

At the same time, machine learning adds a new dimension to the analysis of data from these simulations, facilitating the extraction of complex trends and the prediction of performance from large datasets. This chapter explores the main computational approaches used for the simulation of photovoltaic devices, as well as the integration of machine learning models to improve the design and efficiency of solar cells, particularly in the case of organic materials.

II.2 Digital Tools Used

The integration of SCAPS-1D and machine learning through Google Colab is a potent and novel strategy in the field of organic solar cell research. The University of Ghent created SCAPS-1D, a one-dimensional simulation program that solves the continuity equation of charge carriers and the Poisson equation of semiconductors, enabling accurate modelling of photovoltaic device performance. It has become a vital tool for the study of thin-film solar cells because of its capacity to simulate a variety of materials, including organic materials like MEH-PPV:PCBM **[1]**.

At the same time, Google Colab, a cloud-based Jupyter notebook environment, facilitates the development and execution of machine learning models, thanks to the integration of popular Python libraries such as TensorFlow, scikit-learn, and PyTorch, as well as free access to GPUs. By combining simulation data obtained via SCAPS-1D with machine learning algorithms executed on Google Colab, it is possible to optimize the design parameters of organic solar cells, predict their performance, and accelerate the development process of new photovoltaic materials.

Figure II. 1: Digital tools used for simulation.

II.3 Integrated Models

II.3.1 The Effective Medium Theory (EMT)

To model the physical processes in active layers composed of donor/acceptor blends, the effective medium theory (EMT) is often used. This approach considers the heterogeneous mixture as a homogeneous layer with average properties derived from the local characteristics of the individual components (mobility, electron affinity, bandgap, etc.) as well as the microstructure of the material. It allows for a significant simplification of the resolution of carrier transport equations by replacing a complex three-dimensional model where interfaces between domains on the order of ~10 nm must be taken into account with a one-dimensional model that is more easily numerically manageable at the device scale (~200 nm). This simplification accelerates the simulations while maintaining an accurate description of the overall behavior of the device.

In this case, the energy gap between the acceptor's LUMO and the donor's HOMO is seen as the effective bandgap (E_g) of the semiconductor, which is an important factor for understanding the material's optoelectronic properties. The transport of electrons and holes in the semiconductor, under operating conditions, is schematically illustrated in **Figure II.2** [2,3].

However, these methods are often made up on the spot and don't always connect the effective parameters used to the real shape of the microstructure, nor do they accurately show certain specific areas like the layers rich in donors or acceptors that overlap. Even with these

drawbacks, the effective medium model is still a useful method for studying and improving how well OSCs made from bulk heterojunctions work.

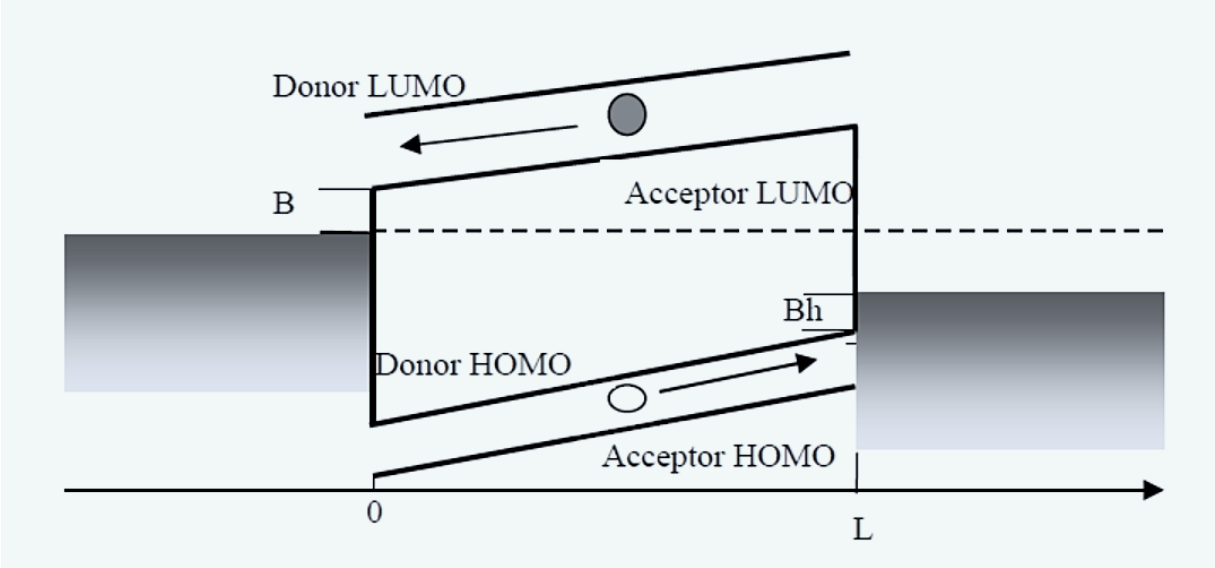

Figure II. 2: Effective Bandgap and Charge Transport in Donor–Acceptor Semiconductors [4].

II.3.2 Drift-Diffusion Model

The drift-diffusion model is a basic and commonly used method for understanding how charge carriers (electrons and holes) move in semiconductor devices, especially in organic solar cells.

This model relies on two complementary mechanisms: drift, caused by the action of an electric field that drives the carriers in a given direction, and diffusion, which results from the concentration gradient of the carriers, causing them to move from areas of high concentration to areas of low concentration. The model relies on two types of equations:

III.3.2.1 Transport Equations

The transport equations **(II.1, II.2),** describe the current densities associated with drift and diffusion.

$$\overrightarrow{J_n} = qD_n\nabla n - q\mu_n n\nabla\phi \qquad \textbf{(II.1)}$$

$$\overrightarrow{J_p} = -qD_p\nabla p + q\mu_p p\nabla\phi \quad \textbf{(II.2)}$$

Where:

$\overrightarrow{J_n}$,$\overrightarrow{J_p}$ are the current densities of electrons and holes, q is the elementary charge, n, p are the concentrations of electrons and holes, ϕ electric potential, D_n, D_p are the diffusion coefficients of electrons and holes and μ_n, μ_p are the mobilities of electrons and holes, given by the Einstein relation **(equation II.3):**

$$D = \mu\frac{k_B T}{q} \quad \textbf{(II.3)}$$

where k_B is the Boltzmann constant and **T** is the temperature.

III.3.2.2 The Continuity Equations

The continuity equations **(II.4, II.5)**, which ensure charge conservation by taking into account the phenomena of generation, recombination, and current flow.

$$\frac{\partial n}{\partial t} = \frac{1}{q}\nabla\cdot\overrightarrow{J_n} + G_n - R_n \quad \textbf{(II.4)}$$

$$\frac{\partial p}{\partial t} = -\frac{1}{q}\nabla\cdot\overrightarrow{J_p} + G_p - R_p \quad \textbf{(II.5)}$$

Where:

G_n , G_p electron and hole generation rates (for example, due to light absorption), R_n, R_p are the recombination rates of electrons and holes, $\nabla\cdot\overrightarrow{J_n}$, $\nabla\cdot\overrightarrow{J_p}$ divergence of the current, representing local losses or accumulations.

These equations are generally coupled with the Poisson equation (II.6) to determine the electric field:

$$\nabla\cdot(\varepsilon\nabla\phi) = -q(p - n + N_D^+ - N_A^-) \quad \textbf{(II.6)}$$

where:

ε is the permittivity of the material, N_D^+ , N_A^- donor and acceptor doping densities.

The whole set of equations enables an accurate simulation of how photovoltaic devices behave with light, especially in how they separate and move the carriers created by the light.

II.3.3 Recombination Mechanism

III.3.3.1 Langevin Recombination

The Langevin recombination is a fundamental theoretical model that describes the bimolecular recombination of charge carriers (electrons and holes) in semiconductors, particularly in low-mobility materials such as disordered organic semiconductors.

In these materials, charge carriers move via localized hopping, and the recombination probability strongly depends on their mobility.

This model is based on the Coulomb interaction between an electron and a hole, when they are within a distance less than a certain critical capture radius **(equation II.7**), they can recombine. The recombination rate is then not limited by the recombination process itself but by the speed at which the carriers meet, which directly depends on their respective mobilities.

$$\mathbf{r_c = \frac{q^2}{4\pi\varepsilon_0\varepsilon_r k_B T}} \qquad \textbf{(II.7)}$$

Recombination according to Langevin is a nongeminate process, following second-order kinetics, and the recombination rate is given by the expression **II.8**:

$$\boldsymbol{R = k\left(pn - n_i^2\right)} \qquad \textbf{(II.8)}$$

where $\boldsymbol{n}$ and $\boldsymbol{p}$ are the electron and hole densities, $\boldsymbol{n_i^2}$ is the intrinsic carrier density, and $\boldsymbol{k}$ is the Langevin recombination coefficient, defined by **equation II.9**:

$$\boldsymbol{k = \frac{q(\mu_n + \mu_p)}{\varepsilon_0 \varepsilon_r}} \qquad \textbf{(II.9)}$$

$\boldsymbol{q}$ is the elementary charge, $\boldsymbol{\mu_n}$, $\boldsymbol{\mu_p}$ are the mobilities of electrons and holes, $\boldsymbol{\varepsilon_0}$ is the vacuum permittivity and $\boldsymbol{\varepsilon_r}$ is the relative permittivity of the material.

III.3.3.2 Shockley-Read-Hall (SRH) recombination

Shockley-Read-Hall (SRH) recombination is a non-radiative mechanism that primarily occurs in disordered materials such as organic semiconductors, where numerous trap states exist within the energy gap. Originally proposed by Shockley, Read, and Hall, this model assumes that crystal defects, or impurities, introduce localized energy levels between the valence band (VB) and the conduction band (CB)[5–7].

The process occurs in two steps: an electron from the conduction band is first captured by a trap level, then a hole from the valence band recombines with this trapped electron. This type of recombination strongly depends on the density of the traps, their energetic position in the gap, and the material's manufacturing technology [5–7].

Generally, two types of traps are distinguished: shallow traps, close to the conduction or valence bands and likely to quickly release carriers, and deep traps, located closer to the center of the gap, which play a central role in recombination mechanisms **(Figure II.3)** [8].

In organic materials, SRH recombination centers are often assumed to be located between the HOMO and LUMO levels. The SRH recombination rate is generally modelled by the **equation II.10**:

$$R_{SRH} = \frac{np - n_i^2}{\tau_p\left(n + N_{LUMO}e^{\frac{E_t - E_{LUMO}}{kT}}\right) + \tau_n\left(p + N_{HOMO}e^{\frac{E_{HOMO} - E_t}{kT}}\right)} \quad \textbf{(II.10)}$$

n , p are electron and hole concentration, n_i^2 *is the* intrinsic carrier concentration τ_p , τ_n *are* lifetime of holes and electrons, E_t *is* trap level energy and N_{LUMO}, N_{HOMO} are density of states in the LUMO region and HOMO region respectively

Equations **(II.11)** and **(II.12)** provide key insights into how the density of defects affects both the carrier lifetime (τ) and diffusion length (L), thereby playing a central role in determining device efficiency

$$\tau_n, \tau_p = \frac{1}{\sigma_n v_{\text{th}} N_t} \quad \textbf{(II.11)}$$

$$L = \sqrt{\mu \frac{kT}{q} \cdot \tau} \quad \textbf{(II.12)}$$

This mechanism plays a crucial role in the performance of organic devices, especially under low injection conditions or when defects are abundant.

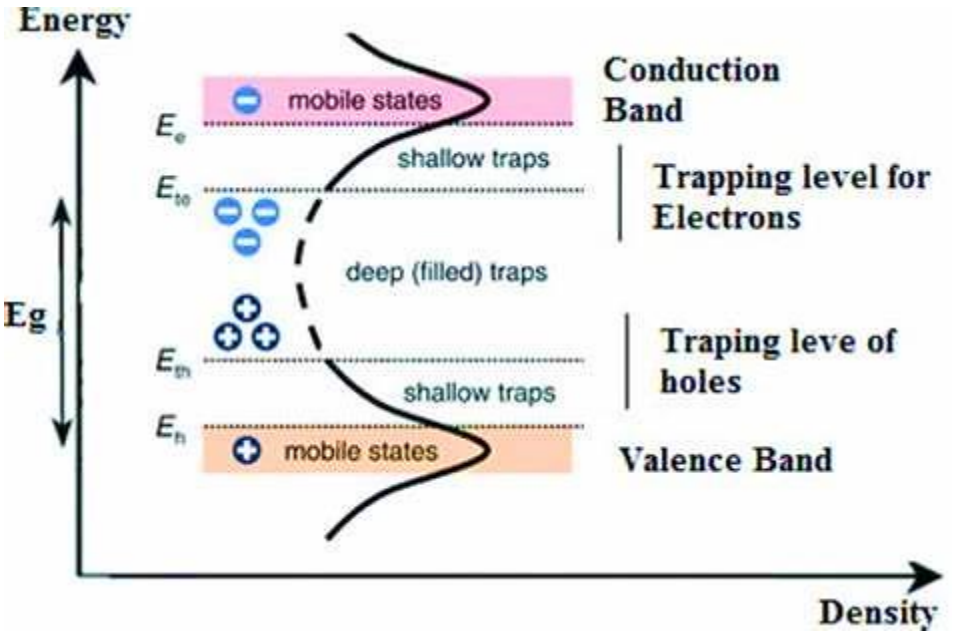

Figure II. 3: Shallow and Deep Trap States [8].

II.3.4 Gaussian disorder model

Mobility (μ) is an essential parameter that determines the speed at which charge carriers (electrons or holes) move under the influence of an electric field in a material. In the Gaussian disorder model (GDM), the mobility is affected by the energy disorder of the material, which comes from defects in its structure [9,10].

In this model, charge transport occurs through intermolecular hops between localized energy sites, which are represented by specific energy levels within the material. This energy distribution is expressed by the density of states N(E), which follows a Gaussian law **(equation II.13)**.

$$\mathbf{N(E) = N_t \exp\left(-\frac{(E-E_0)^2}{2\delta^2}\right)} \quad \textbf{(II.13)}$$

Where N_t is the total density of molecules, and δ represents the variance of the distribution, measuring the extent of the disorder. In this context, charge transport is characterized by a Poole-Frenkel-type mobility, which varies exponentially with the intensity of the disorder, according to the relation **II.14.**

$$\boldsymbol{\mu = \mu_0 \exp\left(-\frac{\delta}{k_B T}\right)} \quad \textbf{(II.14)}$$

Where μ_0 is the mobility at low disorder, k_B is the Boltzmann constant, and T is the temperature. Thus, energetic disorder plays a central role in the mobility of charge carriers, directly affecting the efficiency of transport and the electronic properties of the material

II.4 From Simulation to Prediction

Nowadays, machine learning (ML) has become an indispensable tool in many scientific fields, particularly in the energy sector and advanced materials. Thanks to its ability to exploit large datasets and establish nonlinear relationships between parameters, it allows for accelerated predictions, reduced computational costs, and sometimes even avoids the need for traditional physical modeling methods.

In this study, the SCAPS-1D simulator is used as a numerical simulation tool to model the behavior of organic solar cells. It plays a fundamental role in understanding the physical mechanisms (charge transport, recombination, potential profile, etc.) and in optimizing the device's performance through parametric exploration.

However, the approach exclusively based on simulation can be limited in terms of speed and exploration of large design spaces. It is in this context that the integration of machine learning makes perfect sense. By using the data created by SCAPS-1D, we can train predictive

models that can quickly estimate how well devices will perform, suggest the best setups, and find complex patterns that analytical modeling might miss **(Figure II.4).**

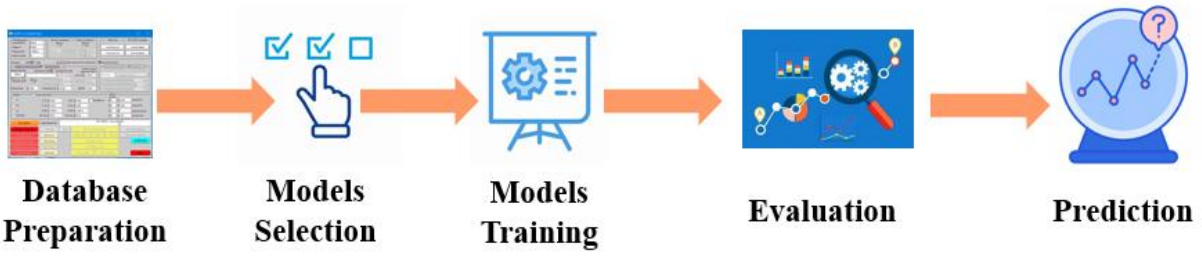

Figure II. 4: Fundamentals and Implementation of Supervised Machine Learning.

II.4.1 Supervised Machine Learning

Supervised machine learning is an approach in which an algorithm learns from labeled training data, that is, data for which the expected outcomes are already known. The objective is to enable the model to establish a relationship between inputs and outputs so that it can predict results for new, unseen data **[11,12]**.

This process is comparable to teacher-guided learning, where the model is gradually corrected until it can correctly generalize the responses. Used in many fields, including the prediction of photovoltaic device performance, supervised machine learning allows for the transformation of raw data into actionable information, paving the way for powerful predictive analyses.

Several supervised learning methods exist, and we will detail them in the following sections.

III.4.1.1 Linear Regression

Linear regression is one of the most fundamental and widely used algorithms in statistics and machine learning. It allows for the identification of linear relationships between a dependent variable and one or more independent variables **(Figure II.5)**. We mainly distinguish between two types of linear regression: simple linear regression and multiple linear regression (MLR) **[12–14]**.

These methods are often used to build predictive models by evaluating the impact of different input variables. In this context, linear regression can be considered a conceptual foundation for more complex models, such as neural networks, where the weights associated with the inputs represent the relative influence of each variable [12–14].

The general equation of multiple linear regression is written as follows **(equation II.15)**:

$$\mathbf{y = \beta_0 + \beta_1 x_1 + \beta_2 x_2 + \cdots + \beta_n x_n + \varepsilon} \qquad \textbf{(II.15)}$$

where $\mathbf{y}$ is the dependent variable, $\mathbf{x_1}$, $\mathbf{x_2}$, …,$\mathbf{x_n}$ are the independent variables, $\boldsymbol{\beta_0}$ is the intercept (or bias), $\boldsymbol{\beta_1}$, …, $\boldsymbol{\beta_n}$ are the coefficients of the variables, and ε is the random error.

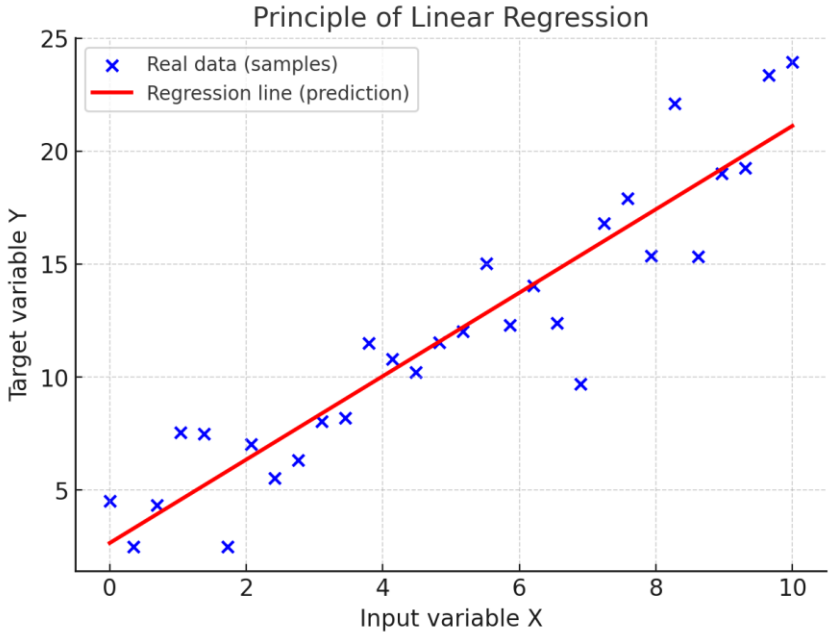

Figure II. 5: Mathematical Foundations of Linear Regression [15].

III.4.1.2 Desision Tree

The decision tree (DT) is an essential technology in machine learning, widely used in various fields for classification and regression tasks. It is a predictive model structured in the form of a tree, composed of nodes, branches, and leaves. Each node represents a characteristic (or attribute) of an example to be classified, each branch corresponds to a possible value of that characteristic, and each leaf indicates a decision or an output class **(Figure II.6).** The algorithm

sorts the instances starting from the root node, directing them through the branches according to the attribute values until reaching a leaf [12–14].

Decision trees can be built quickly, making them an effective tool for processing large amounts of data. A commonly used equation in the construction of a decision tree is that of entropy, which measures the degree of impurity of a dataset **(equation II.16):**

$$\textbf{Entropie}(S) = -\sum_{i=1}^{n} p_i \log_2(p_i) \qquad \textbf{(II.16)}$$

where S is the dataset, p_i is the proportion of elements belonging to class i, and n is the total number of classes.

This measure allows for selecting the attribute that provides the best separation between classes, by maximizing the information gain at each split of the tree.

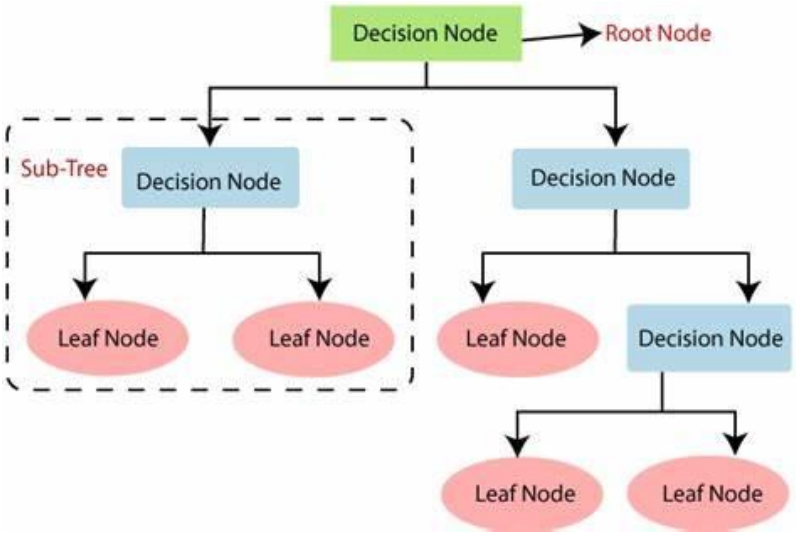

Figure II. 6: Decision Tree Architecture [16].

III.4.1.3 Random Forest

Random Forest is an ensemble machine learning algorithm that combines the results of several decision trees to produce a robust and accurate classifier. The fundamental principle relies on the construction of multiple decision trees, each being independently trained on a random sample of the training dataset (bootstrap method) and randomly selecting a subset of

features at each node split **(Figure II.7)**. This double introduction of randomness in the data and the attributes helps reduce overfitting and improve the model's generalization.

During the prediction phase, Random Forest aggregates the results of individual trees by majority vote for classification tasks or by averaging for regression tasks **[17]**.

This approach allows for transforming a set of weak models (decision trees) into a strong learner, capable of providing reliable results even on complex or noisy data.

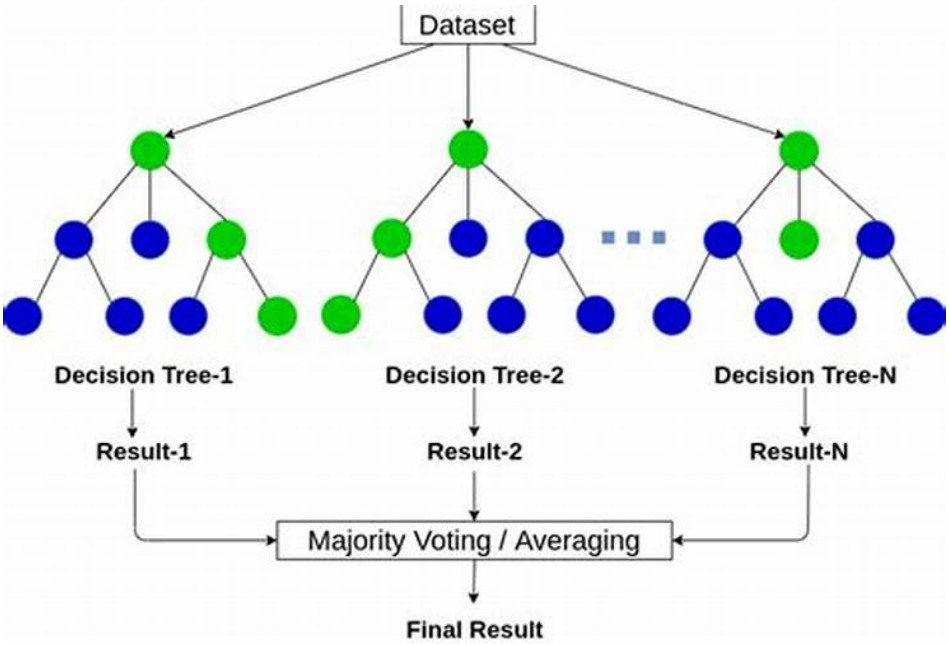

Figure II. 7: Random Forest Architecture **[18]**.

III.4.1.4 Extreme Gradient Boosting

XGBoost (Extreme Gradient Boosting) is a machine learning algorithm based on the principle of gradient boosting, an ensemble technique that combines several weak learners, typically decision trees, to form a powerful predictive model **(Figure II.8)**. Unlike other methods, XGBoost builds its trees sequentially, with each tree learning to correct the errors (or residuals) of the previous trees. The trees used are often shallow to limit overfitting and ensure that each iteration focuses on the marginal improvement of predictions. The architecture of XGBoost is designed to be efficient, scalable, and robust, making it particularly effective on large datasets or in competitive environments like Kaggle competitions **[19,20]**.

Thanks to its ability to model complex relationships while maintaining excellent generalization, XGBoost has become one of the most popular algorithms for classification, regression, and other predictive analysis applications.

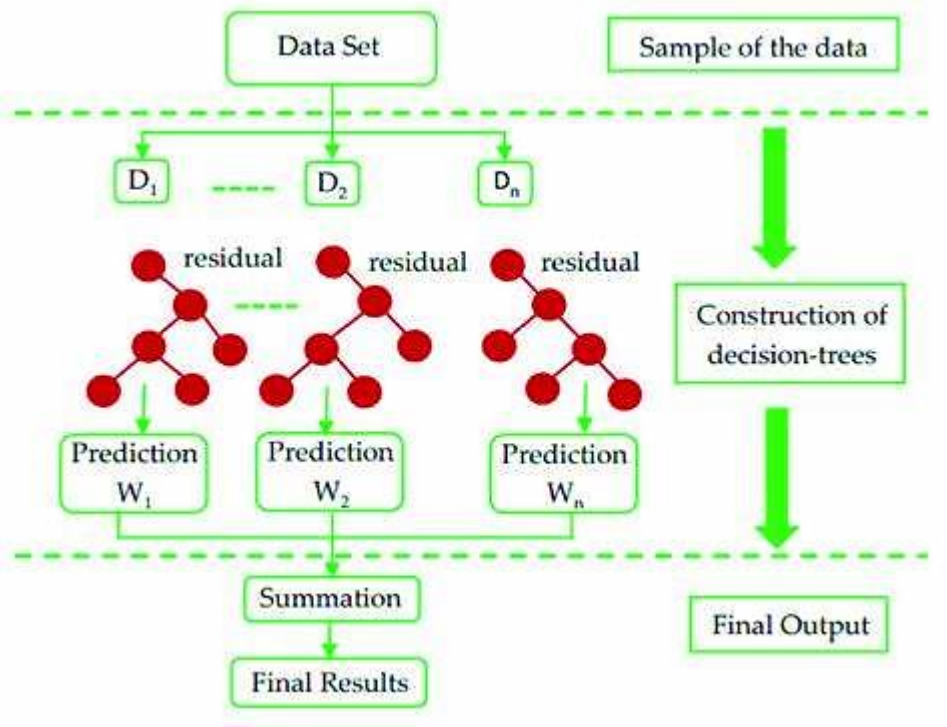

Figure II. 8: XGBoost Architecture [18].

III.4.1.5 K-Nearest Neighbors (KNN)

K-Nearest Neighbors (KNN) is a non-parametric and intuitive machine learning algorithm, widely used for classification and regression tasks. In the case of KNN regression, the principle is based on the idea that instances close in the feature space have similar target values. Thus, to predict the value of an unknown data point, the algorithm identifies its k nearest neighbors in the training set, using a distance measure, usually the Euclidean distance **(Figure II.9)**. The average (or weighted average) of the neighbors' target values is used to make the prediction [21,22].

This model does not rely on any prior assumptions regarding the distribution of the data or the functional form between the variables, making it particularly suitable for complex or

nonlinear relationships**.** the prediction for a new point xxx is calculated as follows **(equation II.17)**:

$$\hat{y} = \frac{1}{k}\sum_{i=1}^{k} y_i(x) \qquad \textbf{(II.17)}$$

where $y_i(x)$ represents the target value of the i-th nearest neighbor of (x) .This simple yet powerful mechanism allows KNN to adapt efficiently to a wide variety of problems.

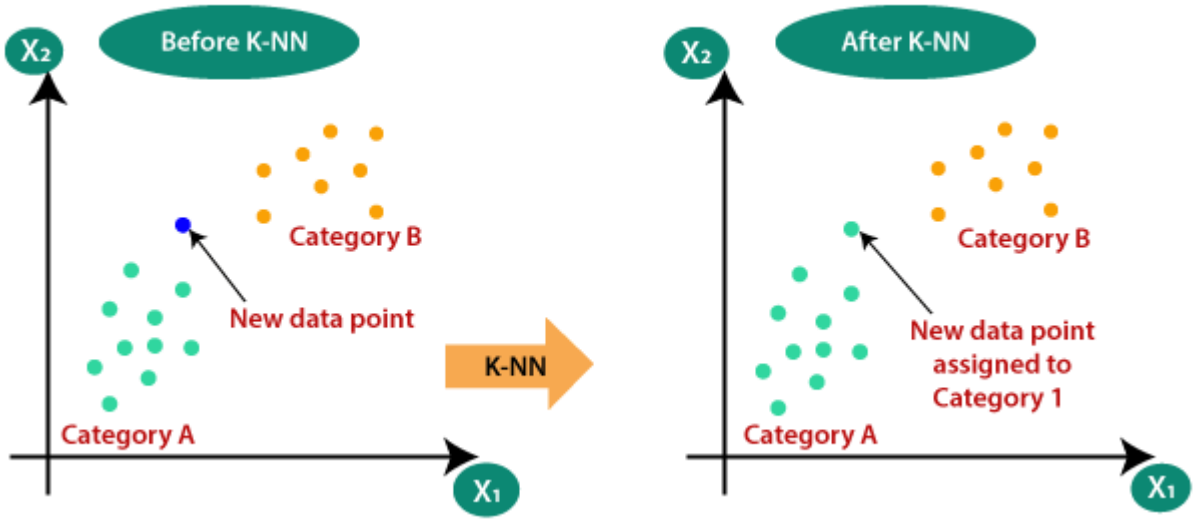

Figure II. 9: KNN Algorithm Workflow [23].

I.5.2 Validation Process

The evaluation of supervised learning models relies on several metrics that measure the accuracy and quality of predictions. Among the most commonly used indicators for regression problems are the mean absolute error (MAE), root mean square error (RMSE), mean absolute percentage error (MAPE), and the coefficient of determination (R^2). These metrics respectively quantify the average error between actual and predicted values, the dispersion of errors, and the proportion of variance explained by the model. The RMSE helps to assess how big the prediction errors are on average, while the R^2 coefficient, which goes from 0 to 1, shows how well the model can explain the differences in the data, with a value near 1 meaning it fits well [24–27].

To make sure the evaluation is strong, techniques like k-fold cross-validation are commonly used, which help accurately assess how well the model performs on new data. These measures thus provide a comprehensive framework for analyzing and improving the quality of predictive models.

$$\mathbf{MSE} = \frac{1}{m}\sum_{i=1}^{m}(x_i - y_i)^2 \quad \textbf{(II.18)}$$

$$\mathbf{RMSE} = \sqrt{\mathbf{MSE}} \quad \textbf{(II.19)}$$

$$\mathbf{R^2} = 1 - \frac{\mathbf{MSE}}{\mathbf{Var(y)}} \quad \textbf{(II.20)}$$

$$\mathbf{MAE} = \frac{1}{n}\sum_{i=1}^{n}\left|y_{real,i} - y_{pred,i}\right| \quad \textbf{(II.21)}$$

y_{real} is the ground truth, what we want to predict, and y_{pred} is what the model calculates or estimates.

II.5 Conclusion

The combination of numerical simulations and machine learning constitutes an effective approach for optimizing photovoltaic devices. SCAPS-1D allows for precise modelling of solar cell behavior, while ML facilitates analysis and prediction of performance. Together, these tools accelerate the design of more efficient cells, particularly in the field of organic materials.

Bibliography

[**1**] Y. El Arfaoui, M. Khenfouch, et N. Habiballah, Optik, vol. 300, p. 171638, avr. 2024

[**2**] T. Liu, S. Ma, B. Yang, S. Xiao and L. Zhou, *Phys Rev B*, 2020, 102, 174208.

[**3**] G. Richardson, C. P. Please and V. Styles, *Eur J Appl Math*, 2017, 28, 973–1014.

[**4**] N. Shrivastav, S. Kashyap, J. Madan, M. K. A. Mohammed, M. K. Hossain, et R. Pandey, Optik, vol. 281, p. 170821, juin 2023, doi: 10.1016/j.ijleo.2023.170821.

[**5**] L. Sun, J. X. Sun, C. H. Xiong and X. H. Shi, *Solar Energy*, 2016, 135, 308–316.

[**6**] J. Szmytkowski, *Solid State Commun*, 2020, 321, 114044.

[**7**] N. S. Ndiaye, O. Simonetti, T. P. Nguyen and L. Giraudet, *Org Electron*, 2021, 99, 106350.

[**8**] M. Ghorab, A. Fattah and M. Joodaki, *Optik (Stuttg)*, 2022, 267, 169730.

[**9**] R. Coehoorn and P. A. Bobbert, *physica status solidi (a)*, 2012, 209, 2354–2377.

[**10**] A. Melianas and M. Kemerink, *Advanced Materials*, DOI:10.1002/ADMA.201806004,.

[**11**] The Top 10 Machine Learning Algorithms Every Data Scientist Should Know | by Emine Bozkus | Medium, https://eminebozkus.medium.com/the-top-10-machine-learning-algorithms-every-data-scientist-should-know-19491811bd24, (accessed 13 May 2025).

[**12**] O. F.Y, A. J.E.T, A. O, H. J. O, O. O and A. J, *International Journal of Computer Trends and Technology*, 2017, 48, 128–138.

[**13**] R. Nath Mohalder, Md. Alam Hossain and N. Hossain, *Int J Adv Res (Indore)*, 2024, 12, 422–438.

[**14**] M. R. Prusty, J. Chakraborty, T. Jayanthi and K. Velusamy, *Lecture Notes in Computer Science (including subseries Lecture Notes in Artificial Intelligence and Lecture Notes in Bioinformatics)*, 2015, 8947, 111–122.

[**15**] Linear Regression in Machine Learning - Shiksha Online, https://www.shiksha.com/online-courses/articles/linear-regression-in-machine-learning/, (accessed 15 May 2025).

[**16**] Decision Tree. One decision to classify and predict… | by Sigireddyviswesh | Medium, https://medium.com/@sigireddyviswesh/decision-tree-2166c873f3e8, (accessed 15 May 2025).

[**17**] G. Jing, DOI:10.54254/2755-2721/149/2025.KL22361.

[**18**] Understanding the Perceptron: The Building Block of Neural Networks | by Jainvidip | Medium, https://medium.com/@jainvidip/understanding-the-perceptron-the-building-block-of-neural-networks-c8995ecf8c42, (accessed 15 May 2025).

[**19**] M. M. Zühlke and D. Kudenko, *Mach Learn*, 2025, 114, 1–52.

[**20**] I. W. Prastiyo and A. Febriandirza, *JURNAL MEDIA INFORMATIKA BUDIDARMA*, 2024, 8, 1694–1705.

[**21**] R. Seyghaly, J. Garcia, X. Masip-Bruin and J. Kuljanin, *Future Internet 2024, Vol. 16, Page 422*, 2024, 16, 422.

[**22**] (PDF) A KNN-Linear Regression Fusion Approach for Improved Real Estate Price Estimation, https://www.researchgate.net/publication/384322683_A_KNN-Linear_Regression_Fusion_Approach_for_Improved_Real_Estate_Price_Estimation, (accessed 15 May 2025).

[**23**] 1. Cours - kNN | qkzk, https://qkzk.xyz/docs/nsi/cours_premiere/algorithmique/knn/1_cours/, (accessed 15 May 2025).

[**24**] T. M. Khan, O. Saidani and S. R. Al Ahmed, *RSC Adv*, 2024, 14, 27749–27763.

[**25**] M. A. Basit, M. A. Ali and M. Yasmeen, *Machine Learning for Advanced Functional Materials*, 2023, 1–20.

[**26**] C. Ren, Y. Wu, J. Zou and B. Cai, *Materials*, 2024, 17, 2686.

[**27**] Y. Miyake and A. Saeki, *Journal of Physical Chemistry Letters*, 2021, 12, 12391–12401.

CHAPTER III

SIMULATION AND OPTIMIZATION OF ORGANIC TANDEM SOLAR CELLS USING SCAPS-1D

III.1 Introduction

Third-generation organic solar cells (OSC) are garnering increasing interest due to the emergence of new materials such as polymers and the introduction of advanced architectures like tandem cells. The latter help to get around the limits of single-junction cells by using the solar spectrum more effectively, thanks to two different active layers: an upper cell that absorbs short-wavelength light and a lower cell that captures longer-wavelength light. Among the different configurations of OSCs, all-polymer solar cells (all-PSCs), which use conjugated polymers as donors (p-type) and acceptors (n-type), stand out for their morphological stability, mechanical flexibility, and compatibility with large-scale and low-cost manufacturing processes **[1–5]**.

Since 2017, the conversion efficiency of all-PSCs has increased from less than 10% to around 17%, but challenges remain, notably a relatively low current density and significant energy losses **[3,6]**. To address this, combining the advantages of fully polymeric devices with a tandem architecture appears to be a promising strategy to improve overall performance.

In this chapter, two distinct strategies have been proposed to evaluate and improve the performance of the devices. The first optimization focused on the top sub-cell, where adjusting the thickness of the active layer and the defect concentration led to significant efficiency gains. The second optimization focused on interfacial engineering by replacing the electron transport layers (ETLs) in both sub-cells.

III.2 Structural Configuration of The Studied Device

III.2.1 Selection of The Constituent Materials of The Device

The active layer is the essential element of an organic photovoltaic device, as it is at this level that light absorption, generation of electron-hole pairs, and their separation and transport occur. To ensure a high energy conversion efficiency, it is therefore crucial to carefully select the materials that compose it. However, the selection of appropriate active materials remains one of the main challenges in the development of organic solar cells, particularly in tandem structures.

In our study, we opted for a tandem architecture using PM6:PY-IT as the active layer of the bottom cell and PM7:PIDT for the top cell due to their spectral complementarity and excellent photovoltaic properties **(Figure III.1)**. The PM6:PY-IT system utilizes a narrow bandgap PSMA acceptor (~1.4 eV), allowing it to efficiently absorb in the near-infrared region and generate a high current. On its part, the PM7:PIDT pair covers the visible part of the spectrum, ensuring efficient absorption in the short wavelengths. Moreover, due to their polymerized nature, PSMA-based active layers, such as PM7:PIDT, exhibit strong thermal stability, which is a significant advantage during the fabrication of tandem devices, often subjected to successive thermal treatments **[7–11]**.

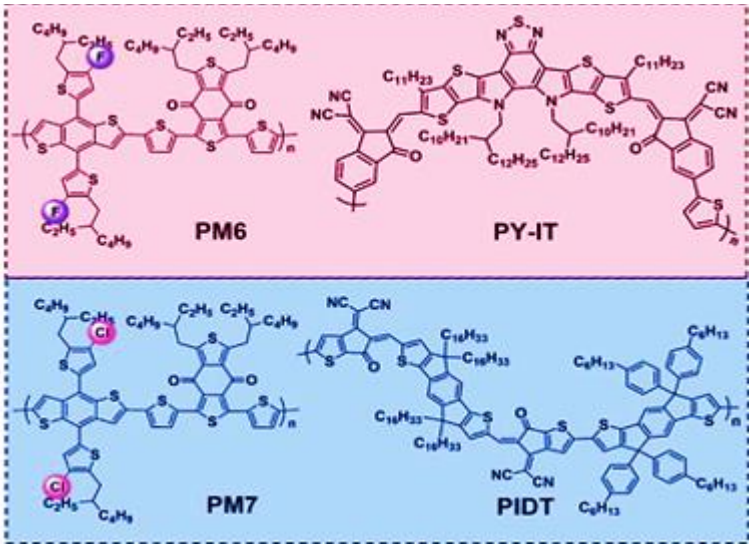

Figure III. 1: Representative Donor–Acceptor Pairs Investigated in This Work **[12]**.

III.2.2 Description of the Two-Terminal Tandem Cell

In the current study, a tandem all-polymer solar cell was designed depict in **Figure III.2**, composed of two vertically stacked sub-cells top and bottom each consisting of a hole transport layer (HTL), an active layer, and an electron transport layer (ETL). The bottom sub-cell integrates PEDOT:PSS, PM6:PY-IT, and PDINN, while the top sub-cell uses PEDOT:PSS, PM7:PIDT, and C60 as HTL, active layer, and ETL, respectively. The materials were selected based on their favorable optical and electronic properties, including suitable energy bandgaps, well-aligned electron affinities, balanced carrier mobilities, and low defect densities.

The tandem sub-cells are connected in series and separated by an intermediate layer (ICL), which can be either a thin metal film or a transparent conductive oxide. This interlayer plays a crucial role in optimizing light absorption and energy conversion, with each photoactive layer tailored to harvest a different portion of the solar spectrum **[13–15]**.

These properties are summarized in **Table III.1**. The intrinsic nature of the active layers and the doping of the transport layers aim to facilitate efficient charge extraction and reduce recombination losses.

The tandem solar cell architecture was simulated using the SCAPS-1D software, which has been described in detail in the previous chapter. As SCAPS-1D does not natively support tandem structures, the two sub-cells were simulated separately, an established and widely accepted methodology for analyzing tandem solar cell performance. The top sub-cell was modeled under standard AM1.5G illumination, while the bottom sub-cell was exposed to a modified spectrum that takes into account the optical transmission of the top cell.

This filtered spectrum was derived using an optical transmission filter calculated according to **equations (III.1) and (III.2)**, as described in previous literature **[16]**.

$$\boldsymbol{S(\lambda) = S_0(\lambda) \cdot \sum \exp(-\alpha_{PEDOT:PSS} d_{PEDOT:PSS}) \cdot \exp(-\alpha_{PM7:PIDT} d_{PM7:PIDT}) \cdot \exp(-\alpha_{C60} d_{C60})} \quad \textbf{(III.1)}$$

$$\boldsymbol{\alpha(E) = A \cdot \sqrt{h\nu - Eg}} \quad \textbf{(III.2)}$$

Where: $\boldsymbol{S(\lambda)}$ ($W.m^{-2}.nm^{-1}$) represents the transmitted light spectrum, $\boldsymbol{S_0(\lambda)}$ ($W.m^{-2}.nm^{-1}$) the incident light spectrum, $\boldsymbol{\alpha}$ (m^{-1}) the absorption coefficient of each layer, and $\boldsymbol{d}$ (m) its corresponding thickness.

A is a material-dependent constant, **hν** (eV) is the photon energy, and **Eg** (eV) is the optical bandgap of the material**.**

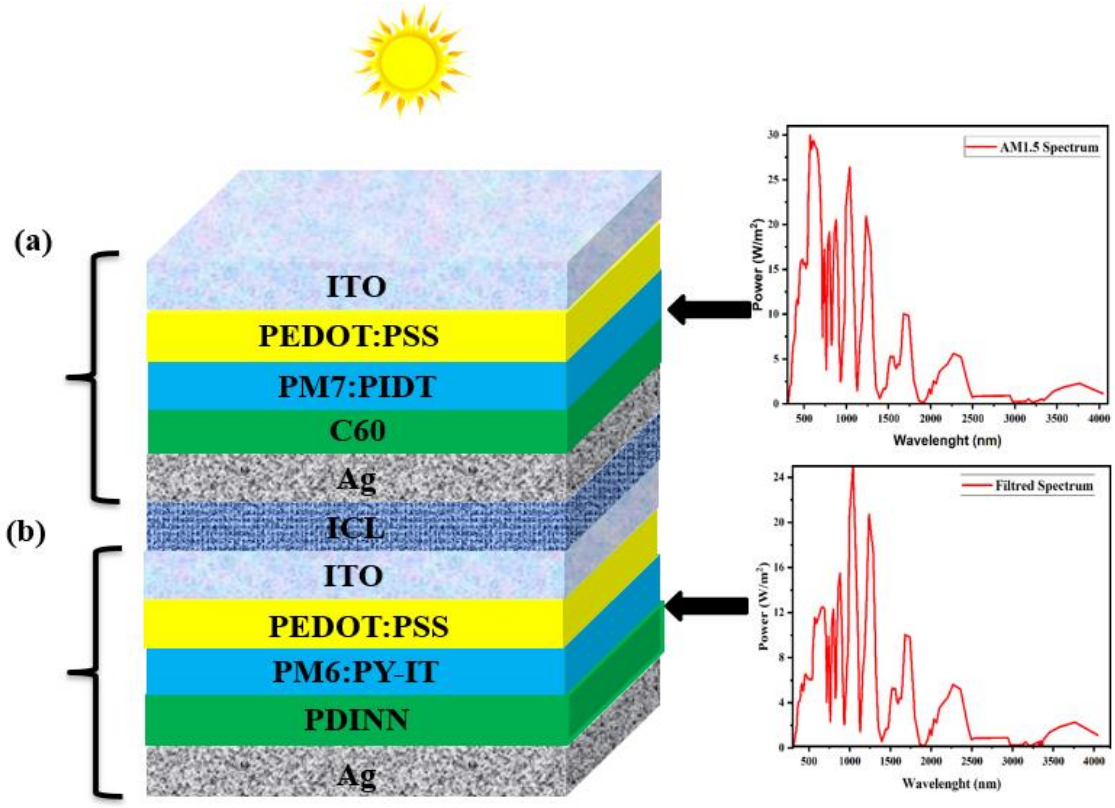

Figure III.2: Incident Spectra: (a) Standard AM1.5 for Top Cell, (b) Filtered Light for Bottom Cell.

Table III. 1: Simulation Input Parameters.

Parameters	Lower Cell [17]			Upper Cell [18]		
	HTL	Active Layer	ETL	HTL	Active Layer	ETL
Materials	**PEDOT :PSS**	**PM6:PY-IT**	**PDINN**	**PEDOT:PSS**	**PM7:PIDT**	**C60**
Thickness(µm)	0.03	0.120	0.03	0.03	0.110	0.03
E_g (eV)	1.6	1.45	2.24	1.6	1.76	1.7
χ (eV)	3.4	3.77	3.78	3.6	3.74	4.3
ε (relative)	3	3	5	3	3	10
N_c (cm^{-3})	2.2×10^{18}	1×10^{21}	1×10^{19}	1×10^{21}	1×10^{21}	2×10^{18}
N_v (cm^{-3})	1.8×10^{19}	1×10^{21}	1×10^{19}	1×10^{21}	1×10^{21}	1.8×10^{19}
μ_e (cm^2/Vs)	4.5×10^{-4}	1.97×10^{-4}	2×10^{-6}	4.5×10^{4}	2.89×10^{-4}	1×10^{-1}

μ_h (cm^2/Vs)	9.9×10^{-5}	1.97×10^{-4}	1×10^{-3}	9.9×10^{-5}	2.89×10^{-4}	1×10^{-1}
N_A (cm^{-3})	1×10^{22}	0	0	9×10^{21}	0	0
N_D (cm^{-3})	0	0	1×10^{22}	0	0	1×10^{22}
N_t (cm^{-3})	1×10^{13}	0	1×10^{13}	1×10^{13}	0	1×10^{13}
Defect Type	Neutral	Neutral	Neutral	Neutral	Neutral	Neutral
Electron capture cross-section (cm^2)	1×10^{-19}	1×10^{-19}	1×10^{-19}	1×10^{-19}	1×10^{-19}	1×10^{-19}
Hole capture cross-section (cm^2)	1×10^{-19}	1×10^{-19}	1×10^{-19}	1×10^{-19}	1×10^{-19}	1×10^{-19}
Energy level above Ev (eV)	0.6	0.6	0.6	0.6	0.6	0.6
Concentration (N_t) (cm^{-2})	1×10^{11}	1×10^{11}	1×10^{10}	1×10^{10}	1×10^{10}	1×10^{10}

III.3 Results And Discussion

III.3.1 J-V characteristics Before optimization

The performance of the tandem cell was evaluated and compared to experimental and simulated results from the literature to validate the robustness of our model.

The current-voltage (J–V) characteristics of the different structures are presented in **Figure III.3(a)** Before optimization, the lower cell achieved a power conversion efficiency (PCE) of 16.63%, with a short-circuit current density (J_{SC}) of 22.55 mA/cm², an open-circuit voltage (V_{OC}) of 0.9242 V, and a fill factor (FF) of 79.78%. These results are in excellent agreement with the performances reported in the literature, both experimental (~16%) and simulated (~16.5%). The top cell showed an efficiency of 10.08%, consistent with previously published values (~10.1%). The tandem cell achieved an overall efficiency of 17.2%, with an open-circuit voltage of 1.91 V and a fill factor of 75.8%, demonstrating good spectral complementarity between the two sub-cells.

These results validate the relevance of the proposed model and confirm its excellent alignment with the experimental data.

Figure III.3(b) illustrates the external quantum efficiency (EQE) of the upper and lower sub-cells as a function of wavelength. The upper cell shows a high response in the short wavelength region (approximately 300 to 750 nm), while the lower cell maintains significant efficiency up to 1200 nm. This complementary spectral distribution allows for better utilization of solar energy, with each sub-cell efficiently absorbing a specific part of the spectrum. The two sub-cells achieve EQE values close to 65%, contributing to the overall improvement in the efficiency of the tandem cell.

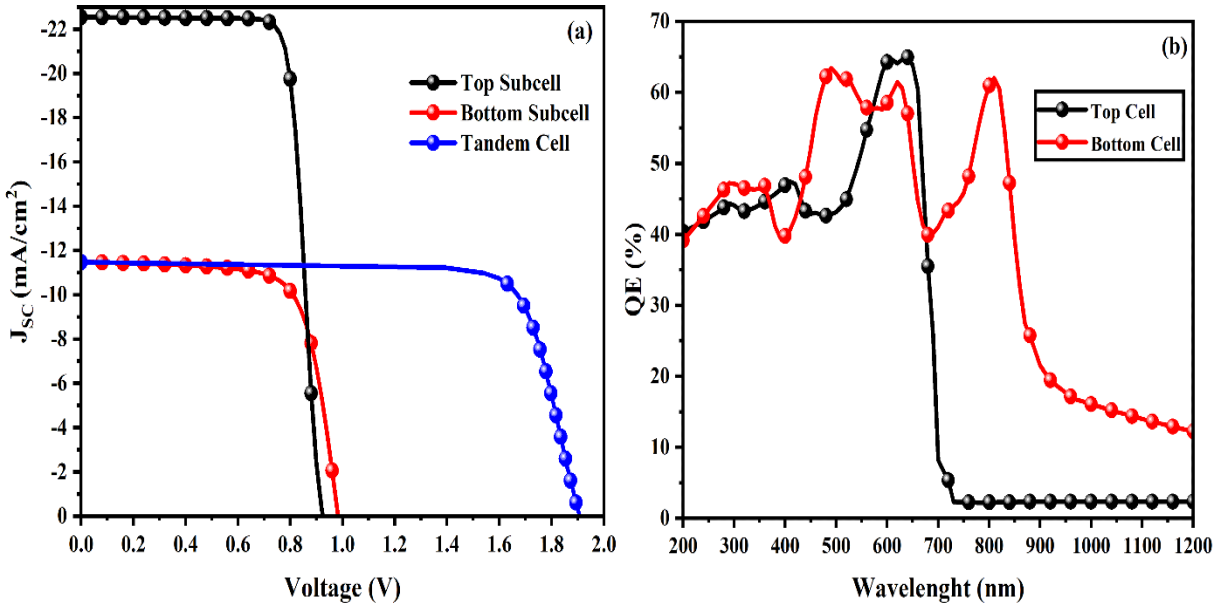

Figure III.3: (a) Pre-Optimization Electrical Characteristics, (b) EQE of Sub-cells.

Tables III.2 summarize the key photovoltaic parameters (J_{SC}, V_{OC}, FF, PCE) of the upper and lower sub-cells as well as the tandem cell and compare them to the results reported in the literature before optimization.

Table III. 2: Pre-Optimization Performance Comparison of Tandem and Sub-Cells with Previous Studies.

PV Parameters	J_{SC} (mA/cm^2)	V_{OC} (V)	FF (%)	PCE (%)	Tools	References
Bottom Sub-cell	22.55	0.9242	79.78	16.63	SCAPS-1D	**This work**
	23.2± 0.6	0.94± 0.01	72.7±1.5	16.0± 0.4	Experimental	**[12]**
	23.33	0.949	74.58	16.50	TCAD	**[17]**
Top Sub-cell	14±0.3	1.1±0.01	65.3±1.5	10.1±1.04	Experimental	**[12]**
	13.76	1.10	66.76	10.110	TCAD	**[17]**
	11.47	1.17	75.44	10.20	SCAPS-1D	**This work**
Tandem Cell	11.5±0.2	2±0.01	75.0±1.2	17.6±0.2	Experimental	**[12]**
	11.9	1.91	75.8	17.2	SCAPS-1D	**This work**

III.3.2 Band Diagram

To optimize the efficient movement of photogenerated charge carriers to their respective electrodes in organic solar cells, it is essential to precisely align the energy bands at the device interfaces. The fundamental performances of these cells, such as the short-circuit current (Jsc) and the open-circuit voltage (Voc), heavily depend on this energy alignment **[19]**.

The description of the conduction band offsets (CBO) and valence band offsets (VBO) can be done using Anderson's rule (**equation III.3 and III.4**), which allows calculating these offsets with respect to the electron affinities (X) and energy gaps (Eg) of the different layers of the device, as follows:

$$\mathbf{CBO} = \left(\mathbf{X_{Active\ layer}} - \mathbf{X_{ETL}}\right) \quad \textbf{(III.3)}$$

$$\mathbf{VBO} = \left(\mathbf{X_{HTL}} - \mathbf{X_{Active\ layer}}\right) + \left(\mathbf{Eg_{HTL}} - \mathbf{Eg_{Active\ layer}}\right) \quad \textbf{(III.4)}$$

These equations translate the energy barriers that charge carriers must overcome and thus explain how the alignment of energy bands conditions the optimal transport of charges, directly impacting the key performance parameters of organic solar cells **[20]**.

Figure III.4(a) illustrates the band diagrams for the two sub-cells .In the upper cell, the active layer is situated between an HTL in PEDOT:PSS and an ETL in C60. At the interface between the absorber and the ETL (C60), a conduction band offset (CBO) of -0.56 eV is observed. This negative CBO forms a cliff-type interface, which is unfavorable for electron transport as it promotes their recombination, leading to a decrease in performance. On the valence side, the VBO between the HTL (PEDOT:PSS) and the active layer is -0.3 eV, also forming a cliff -type interface for holes, which can hinder their efficient extraction.

In contrast, the lower cell shows a more favorable alignment (**Figure III.4(b)**). The CBO between the absorber and the ETL is +0.03 eV, forming a slight "spike," considered acceptable to limit recombination without blocking electronic transport. The VBO at the HTL/absorber interface is -0.22 eV, representing a moderate cliff interface. Moreover, the CBO between the HTL (PEDOT:PSS) and the absorber is very low (-0.01 eV), indicating a favorable alignment for the passage of electrons.

In summary, the lower cell benefits from a better overall energy alignment, reducing recombination losses and promoting more efficient charge transport, unlike the upper cell, where cliff-type interfaces are more pronounced and unfavorable[21].

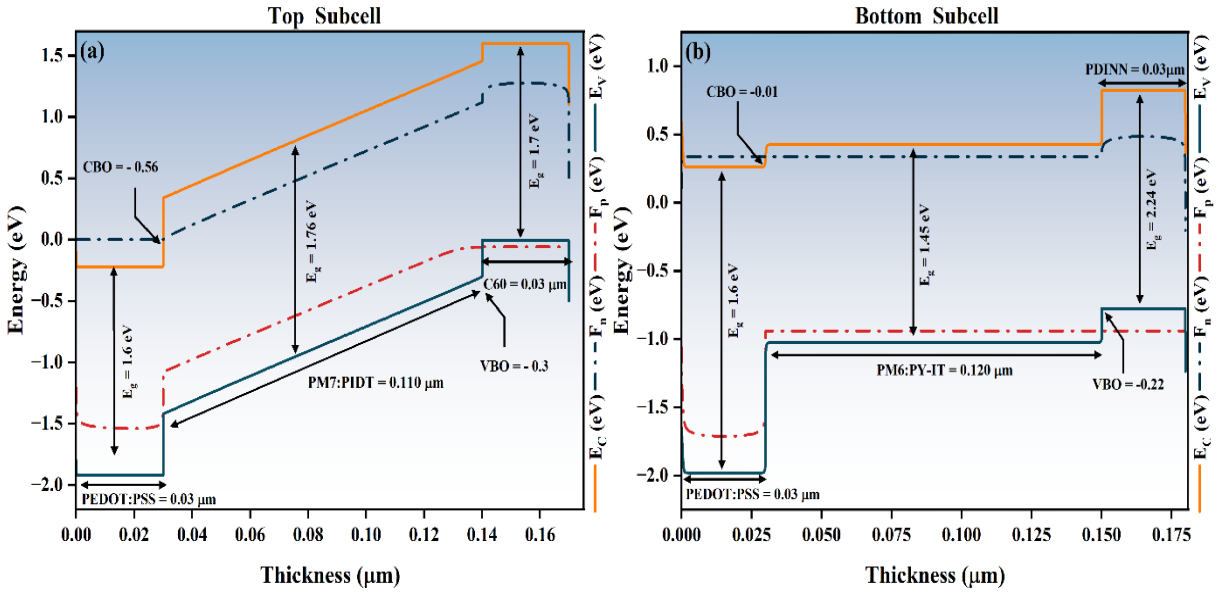

Figure III.4: Band Alignment Simulations for (a) Top and (b) Bottom Sub-cells.

III.3.3 Role of HTL and ETL Matching in Enhancing Tandem Cell Efficiency

To better understand the optimal values of the conduction band offset (CBO) and valence band offset (VBO) in this device, it is crucial to analyze the influence of the materials constituting the electron transport layer (ETL) and the hole transport layer (HTL) on the overall performance of the device [22].

The analysis of variations in ETL and HTL materials, both in the upper cell and the lower cell of a tandem solar cell, highlights their decisive influence on the device's efficiency.

It is within this framework that simulations are conducted in this section to evaluate the performance of different combinations of HTL and ETL layers in the tandem configuration.

The properties of these materials are presented in **Table III.3**.

Table III. 3: Electrical Parameters for Different ETLs and HTLs.

Layer	**ETLs**				**HTLs**			
Parameters	**TiO_2 [23]**	**WS_2 [24]**	**ZnO [25]**	**PDINN [26]**	**CuI [27]**	**CuO [28]**	**P3HT [29]**	**GO [30]**
E_g (eV)	3.2	1.8	3.3	2.24	3.1	1.51	1.7	2.48
χ (eV)	4	4	4	3.78	2.1	4.07	3.5	2.3
ε (relative)	9	9	9	5	6.5	18.1	3	10
N_c ($1.cm^{-3}$)	1.8×10^{19}	2.4×10^{19}	3.7×10^{18}	1×10^{19}	2.8×10^{19}	2.2×10^{19}	2×10^{21}	1.8×10^{18}
N_v ($1.cm^{-3}$)	1.8×10^{19}	1.8×10^{19}	1.8×10^{19}	1×10^{19}	1×10^{20}	5.5×10^{20}	2×10^{21}	2.2×10^{18}
μ_e (cm^2/Vs)	20	100	100	2×10^{-6}	100	100	1.8×10^{-3}	26
μ_h (cm^2/Vs)	10	100	25	1×10^{-3}	43.9	0.1	1.86×10^{-2}	23
N_A (cm^{-3})	0	0	0	0	1×10^{18}	1×10^{18}	1×10^{18}	1×10^{18}
N_D (cm^{-3})	1×10^{18}	1×10^{18}	1×10^{18}	1×10^{22}	0	0	0	0
N_t (cm^{-3})	1×10^{15}	1×10^{15}	1×10^{15}	1×10^{15}	1×10^{15}	1×10^{15}	1×10^{15}	1×10^{15}

The overall performance of a tandem cell strongly depends on the energy alignment at the ETL/absorber and HTL/absorber interfaces, expressed by the conduction band offset (CBO) and valence band offset (VBO). This is clearly illustrated in **Figures III.5 and III.6**, which show how minimal energy offsets facilitate smoother carrier flow.

For the bottom cell, PDINN stands out with a nearly zero CBO (−0.01 eV), ensuring excellent band alignment and optimal electron extraction. In contrast, materials such as ZnO, TiO_2, and WS_2, with a CBO of −0.23 eV, introduce an energy barrier that limits performance.

This energetic advantage translates into higher open-circuit voltages and power conversion efficiencies (PCE), exceeding 24% in some combinations, notably with CuI or P3HT as HTL, which exhibit an almost zero VBO (−0.02 eV).

Conversely, more significant misalignments, such as those observed with GO (−0.44 eV) or CuO (+0.36 eV), cause notable losses in V_{OC}, fill factor, and thus overall efficiency.

The short-circuit current density remains generally stable around 11.6 to 11.8 mA/cm², with a peak at 13.2 mA/cm² for the CuI/WS_2 combination, owing to excellent alignment that limits interfacial recombination. The FF often exceeds 80%, reflecting good charge transport, although some anomalies remain, such as with the CuI/WS_2 pair (FF = 54.8%), indicating interfacial issues despite a good theoretical VBO.

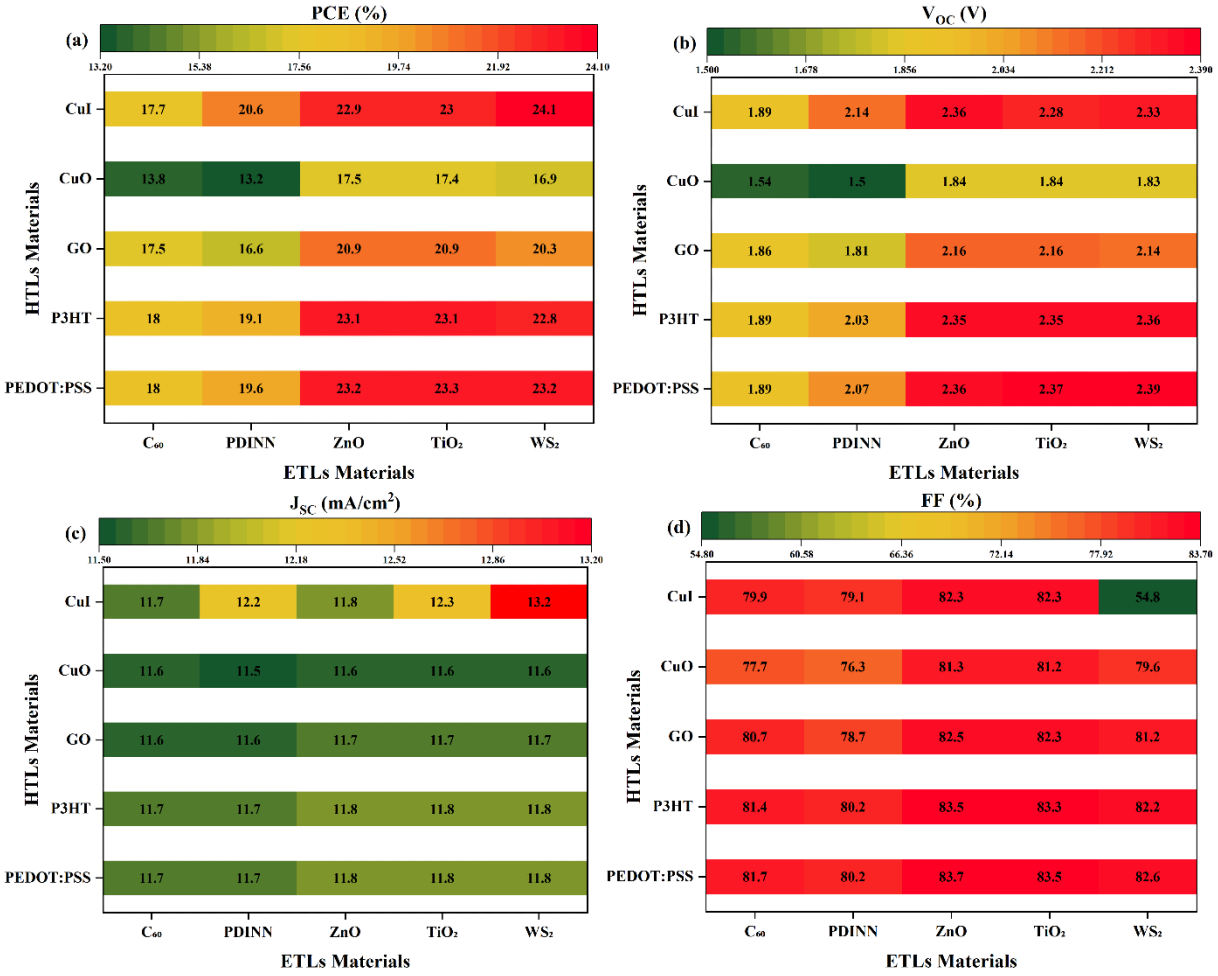

Figure III.5: Material Selection of ETL and HTL in Bottom Cell and Its Effect on Tandem Photovoltaic Performance.

For the top cell, a similar trend is observed: PDINN provides a CBO of −0.04 eV, significantly better than ZnO, TiO_2, or WS_2 (−0.26 eV), explaining the higher V_{OC} and PCE achieved with PDINN. Among HTLs, CuI, P3HT, and GO offer good band alignment, while CuO, despite a slightly positive VBO (+0.08 eV), exhibits high FF values (>84%) but more variable performance.

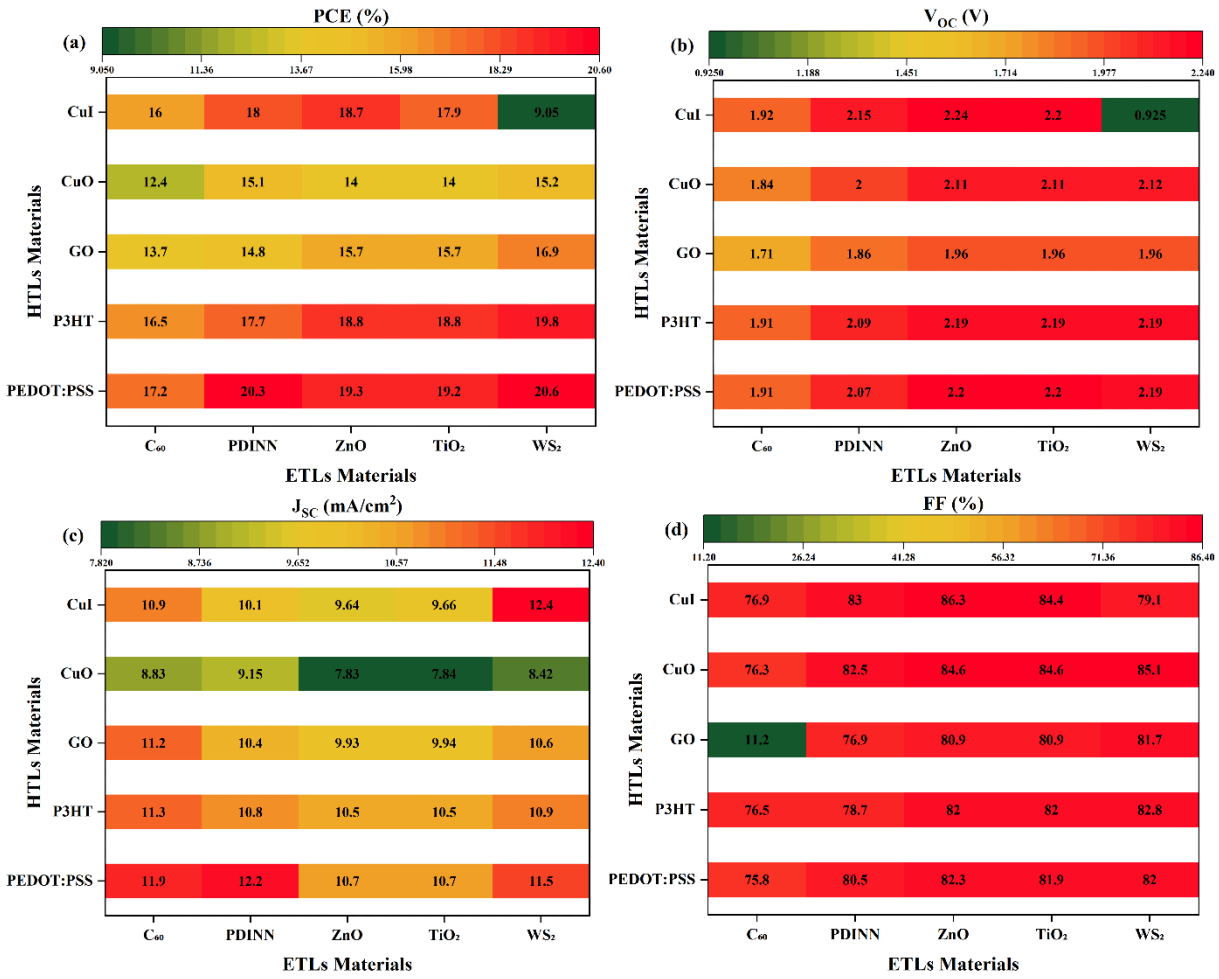

Figure III.6: Material Selection of ETL and HTL in Bottom Cell and Its Effect on Tandem Photovoltaic Performance.

In summary, the highest efficiencies are consistently obtained when CBO and VBO values are close to zero, ensuring efficient charge extraction and minimizing energy losses at the interfaces. Thus, interfacial material engineering emerges as a crucial lever to optimize tandem cell performance through precise control of band alignments and energetic compatibility between functional layers **[11]**.

III.3.4 Thickness and Defect Optimization in Tandem Sub-cells for Enhanced Efficiency

The presence of defects in the absorber layer plays a crucial role in the performance of photovoltaic devices, as these defects act as recombination centers or traps, promoting electron-

hole recombination. This phenomenon, explained by the Shockley-Read-Hall mechanism, leads to a reduction in both the diffusion length and carrier lifetime, which in turn results in a decrease in cell efficiency, as discussed **in Section (II.3.3.2)**. Furthermore, the thickness and defect density significantly influence the processes of charge generation, recombination, and transport within the absorber layer, thereby impacting the overall performance of the device**[31,32]**.

In this context, we studied the combined effect of absorber layer thickness and defect density in both sub-cells (top and bottom) of a tandem solar cell, as shown in **Figures III.7 and III.8**, to assess their influence on the device's overall performance. For the top cell, we analyzed the impact of the absorber layer thickness by varying it from 80 nm to 200 nm while simultaneously changing the defect density within a range from 10^{10} to 10^{14} cm^{-3} and keeping the structure of the bottom cell unchanged. The results reveal that an increase in thickness initially enhances performance, particularly the short-circuit current density and the power conversion efficiency, due to improved light absorption. This improvement is especially notable at low defect densities ($\leq 10^{12}$ cm^{-3}), with a maximum efficiency of 24.6% achieved at a thickness of 200 nm.

In contrast, at high defect densities ($\geq 10^{13}$ cm^{-3}), increasing the thickness leads to performance degradation due to more significant non-radiative recombination, resulting in a marked drop in the fill factor and open-circuit voltage, with efficiency falling to 13.1% **[31]**.

Simultaneously, the combined effect of thickness and defect density was also evaluated for the bottom sub-cell while keeping the top cell's structure constant. The results show that at low defect densities ($\leq 10^{11}$ cm^{-3}), increasing the thickness has a limited impact on performance, with efficiency remaining stable around 19.3% and a slight increase in Voc. However, when the defect density exceeds 10^{12} cm^{-3}, the performance of the tandem cell progressively deteriorates: V_{OC} decreases from 2.11 V to 1.73 V at a defect density of 10^{14} cm^{-3}, accompanied by a reduction in J_{SC} and a significant drop in FF (from 77.9% to 64.4%) **[32]**.

These results highlight the importance of jointly optimizing both the thickness and the crystalline quality (low defect density) in the two sub-cells. A thicker absorber layer can improve how well it captures light, but this benefit is reduced or can even be harmful if there are too many defects, as it leads to more recombination. Therefore, a well-balanced compromise between layer geometry and material purity is essential to achieve optimal performance in tandem solar cells **[31,33]**.

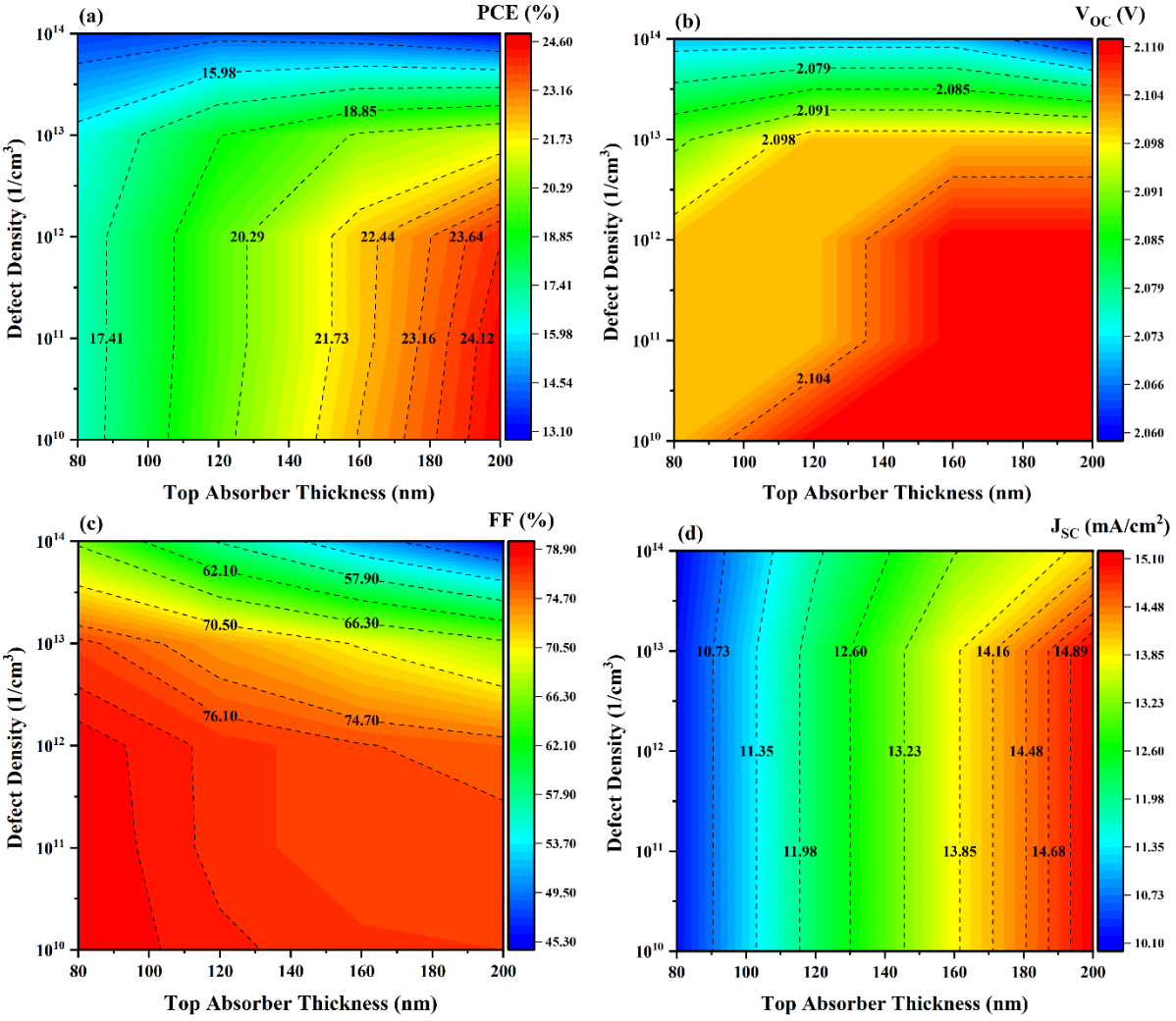

Figure III.7: Impact of Active Layer Thickness and Defect Density in the Top Sub-cell on Tandem Cell Efficiency.

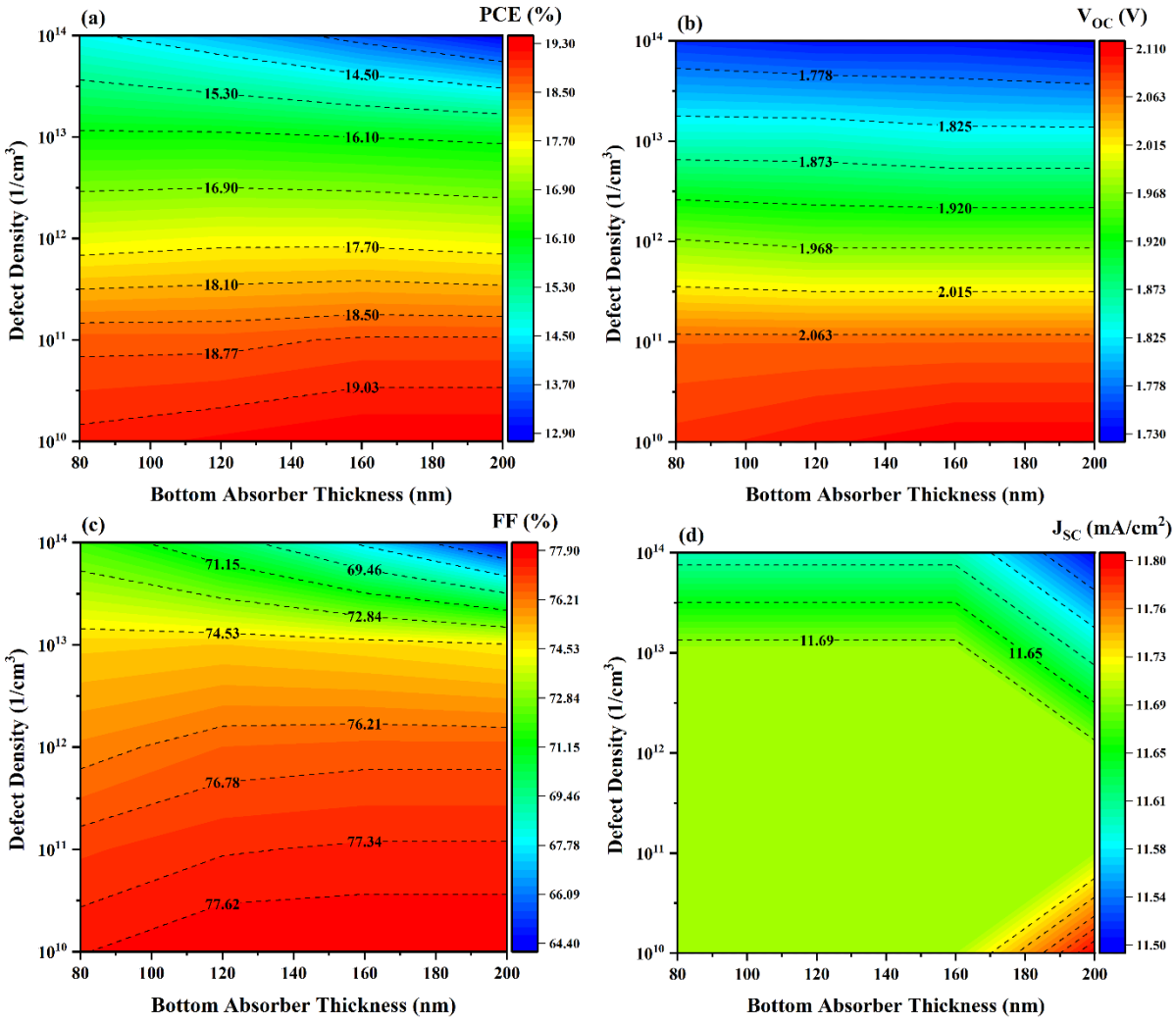

Figure III.8: Impact of Active Layer Thickness and Defect Density in the Bottom Sub-cell on Tandem Cell Efficiency.

III.3.5 Current–Voltage Performance Metrics

As mentioned at the beginning of this chapter, the aim of this study is to optimize the tandem solar cell using two distinct strategies, both of which have demonstrated significant performance improvements based on SCAPS-1D simulations. The current density–voltage (J–V) characteristics corresponding to these two strategies are illustrated in **Figures III.9(a)** and **III.9(b).**

The first strategy focused on optimizing the top cell by adjusting the active layer thickness and defect concentration. The best performance was achieved with a 200 nm active layer and a defect concentration of 10^{11} cm^{-3}, resulting in a short-circuit current density of 15.1 mA/cm², an open-circuit voltage of 2.11 V, a fill factor of 76.7%, and a power conversion efficiency (PCE) of 24.5%. These results clearly surpass those of the initial unoptimized device (J_{SC} = 11.9 mA/cm², V_{OC} = 1.91 V, FF = 75.8%, PCE = 17.2%) and also outperform several state-of-the-art experimental values reported in the literature **[12]**.

The second strategy involved replacing the electron transport layer (ETL) materials in both sub-cells. Specifically, titanium dioxide (TiO_2) was used in the bottom cell and PDINN in the top cell. This configuration led to a J_{SC} of 11.769 mA/cm², a V_{OC} of 2.3359 V, an FF of 83.049%, and a PCE of 22.831%. Although this strategy resulted in a slightly lower current density compared to the first, it exhibited significantly higher V_{OC} and FF. These improvements indicate a more efficient charge separation and extraction mechanism, which enhances the overall device performance.

Beyond simple numerical gains, the improved device performance stems largely from strategic engineering in the charge transport layers. The electron and hole transport layers (ETL and HTL) facilitate directional charge extraction and play a crucial role in suppressing recombination losses and aligning energy levels across interfaces **[34]**.

In the top sub-cell, the use of PDINN a conjugated small molecule with well-matched energy levels proves particularly beneficial. It efficiently channels electrons to the cathode while acting as a robust barrier to holes, thanks to its deep HOMO level. This dual function reduces leakage and interfacial recombination, contributing to enhanced fill factor and open-circuit voltage **[35]** .

In the bottom sub-cell, TiO_2 serves as a highly effective ETL due to its favorable conduction band alignment with non-fullerene acceptors. Its low trap density mitigates Shockley–Read–Hall recombination, while its high dielectric constant helps screen Coulombic interactions, thereby limiting charge recombination **[36,37]** .

Overall, these interfacial enhancements underscore the critical role of transport layer design not just the intrinsic properties of the active materials in advancing tandem organic solar cell performance. This reinforces a growing consensus in the field: Interface engineering is central to pushing the efficiency boundaries of organic photovoltaics **[38]**.

Table III. 4: Performance metrics of optimized tandem cell.

PV Parameters	J_{SC} (mA/cm^2)	V_{OC} (V)	FF (%)	PCE (%)	Method	References
Cell Before optimazation	11.5±0.2	2±0.01	75.0±1.2	17.6±0.2	Experimental	**[9]**
	11.9	1.91	75.8	17.2	SCAPS-1D	**This work**
1st Strategy optimazation	15.1	2.11	76.7	24.5	SCAPS-1D	**This work After optimazation**
2nd Strategy optimazation	11.769	2.3359	83.049	22.831	SCAPS-1D	

Compared to other reported tandem configurations represented in **Table III.5**, both optimization strategies particularly the second demonstrated superior performance in terms of voltage output and fill factor, reflecting the effectiveness of interfacial engineering and material selection.

The structural and material modifications implemented in this study successfully improved spectral utilization, reduced recombination losses, and enhanced charge transport properties.

Overall, the results confirm that the proposed optimization approaches are effective pathways for advancing tandem solar cell technology. The notable gains in voltage, fill factor, and efficiency underscore the potential of combining physical parameter tuning with interface and material engineering to achieve high-performance tandem devices.

Table III. 5: A state-of-the-art comparison between OSC/OSC TSC PV metrics and some TSCs.

PCE [%]	V_{OC} [V]	J_{SC} [mA/ cm²]	FF [%]	Bottom absorber layer	Top absorber layer	Refs.
19	1.69	15	74.8	PTB7-Th:BTPSeV-4F (1.21 eV)	PM6 :O1-Br (1.58 eV)	[39]
17.3	1.64	14.4	73.3	PTB7-Th:O6T-4F (1.24 eV)	PBDB-T :F-M (1.72 eV)	[40]
15.9	1.66	14.1	68	PM6 :SFT8-4F (1.31)	PCE-10:BT-CIC:BEIT-4F (1.64 eV)	[40]
15	1.6	13.6	69	PTB7-Th:PCDTBT:IEICO-4F (1.32 eV)	PBDB-T-2F:TfIF-4FIC (1.65 eV)	[40]
19.5	1.912	14.2	72	PBDB-TF :ITCC (1.32 eV)	PBDB-TF:BTP-eC11 (1.74 eV)	[40]
18.7	1.883	14	70.9	PM6 :CH1007 :PC71BM (1.36 eV)	D18 :F-ThBr (1.73 eV)	[41]
15.2	1.61	12.9	73	PM6 :Y6 (1.37 eV)	PV2000 :PCBM (1.73 eV)	[40]
19.6	2.03	13	74.2	PBDB-TF:HDO-4Cl:BTP-eC9 (1.39 eV)	PB2:GS-ISO (1.78 eV)	[41]

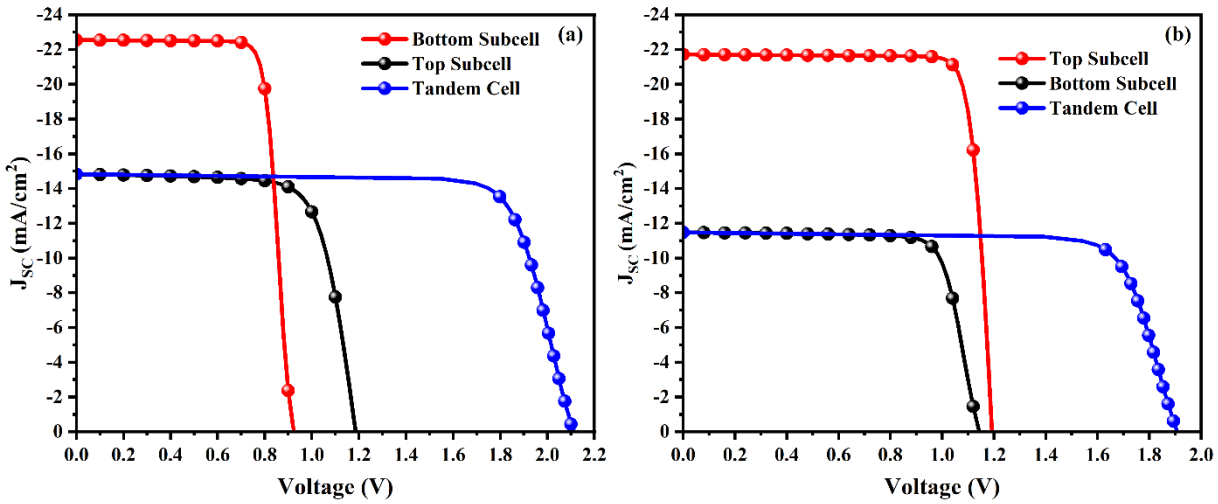

Figure III.9: (a) JV Curves of Sub-cells and Tandem Cell Following First Optimization, (b) Following Second Optimization.

III.3.5.1 External Quantum Efficiency

From a spectral standpoint as illustrated in **Figure III.10**, the first strategy partially improves the spectral complementarity between the two sub-cells, with external quantum efficiency (EQE) peaks reaching around 63%. However, the curves still show fluctuations and an imperfect spectral distribution.

In contrast, the second strategy clearly stands out: the EQE of the bottom cell is significantly enhanced, reaching up to 69%, and the spectral transition between the two sub-cells becomes smoother, indicating improved spectral synergy.

This strategy thus enables more efficient utilization of the solar spectrum and leads to a notable enhancement in the overall tandem cell performance compared to both the initial configuration and the first optimization approach.

Unlike the unoptimized state, where the two cells exhibited partial spectral overlap and marked irregularities, the proposed strategies particularly the second one provides a better distribution of the spectrum between the top cell (300–700 nm) and the bottom cell (700–1150 nm), along with higher peak EQE values. The spectral response curves become smoother and more coherent, reducing optical losses and significantly boosting the overall efficiency of the tandem device.

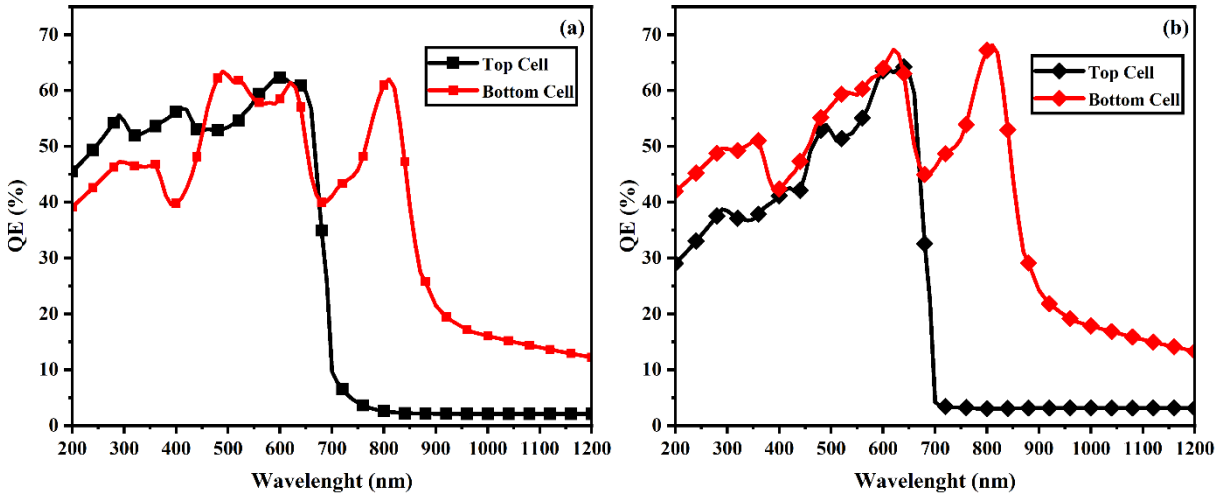

Figure III.10: (a) EQE of the Sub-cells Following First Optimization, (b) Following Second Optimization.

III.4 Conclusion

This chapter has explored the optimization of a tandem solar cell through two distinct strategies. The first focused on adjusting the active layer thickness and defect concentration of the top sub-cell, which led to a significant enhancement of the short-circuit current density (J_{SC} = 15.1 mA/cm²) and an improved overall efficiency (PCE = 24.5%, V_{OC} = 2.11 V, FF = 76.7%).

The second strategy involved replacing and optimizing the ETL materials in both sub-cells, which resulted in remarkable gains in the open-circuit voltage (V_{OC} = 2.34 V) and the fill factor (FF = 83%), yielding a power conversion efficiency of 22.83%.

SCAPS-1D simulations confirmed that both strategies significantly outperform the initial configuration (PCE ≈ 17.2%) and rival or even surpass several results reported in the literature.

These findings highlight the crucial role of physical parameter engineering and interfacial optimization in boosting tandem OSC performance.

While the results are promising, experimental validation remains necessary to confirm these outcomes and support further development toward efficient, real-world applications of tandem organic solar cells.

Bibliography

[**1**] Y. R, S. A.P, M. P, A. J and S. R, *Optik (Stuttg)*, 2020, 212, 164723.

[**2**] X. Liu, M. Sha, H. Yin and X. Hao, *APL Energy*, DOI:10.1063/5.0170931.

[**3**] R. Sun, W. Wang, H. Yu, Z. Chen, X. X. Xia, H. Shen, J. Guo, M. Shi, Y. Zheng, Y. Wu, W. Yang, T. Wang, Q. Wu, Y. (Michael) Yang, X. Lu, J. Xia, C. J. Brabec, H. Yan, Y. Li and J. Min, *Joule*, 2021, 5, 1548–1565.

[**4**] H. Sun, X. Guo and A. Facchetti, *Chem*, 2020, 6, 1310–1326.

[**5**] X. Zhan, Z. Tan, B. Domercq, Z. An, X. Zhang, S. Barlow, Y. Li, D. Zhu, B. Kippelen and S. R. Marder, *J Am Chem Soc*, 2007, 129, 7246–7247.

[**6**] R. Ma, Y. Tao, Y. Chen, T. Liu, Z. Luo, Y. Guo, Y. Xiao, J. Fang, G. Zhang, X. Li, X. Guo, Y. Yi, M. Zhang, X. Lu, Y. Li and H. Yan, *Sci China Chem*, 2021, 64, 581–589.

[**7**] H. Yin, C. Yan, H. Hu, J. K. W. Ho, X. Zhan, G. Li and S. K. So, *Materials Science and Engineering: R: Reports*, 2020, 140, 100542.

[**8**] J. Guo, X. Xia, B. Qiu, J. Zhang, S. Qin, X. Li, W. Lai, X. Lu, L. Meng, Z. Zhang and Y. Li, *Advanced Materials*, 2023, 35, 2211296.

[**9**] Z. G. Zhang, Y. Yang, J. Yao, L. Xue, S. Chen, X. Li, W. Morrison, C. Yang and Y. Li, *Angewandte Chemie - International Edition*, 2017, 56, 13503–13507.

[**10**] Y. Lin, J. Wang, Z. G. Zhang, H. Bai, Y. Li, D. Zhu and X. Zhan, *Advanced Materials*, 2015, 27, 1170–1174.

[**11**] S. Chen, L. Feng, T. Jia, J. Jing, Z. Hu, K. Zhang and F. Huang, *Sci China Chem*, 2021, 64, 1192–1199.

[**12**] Q. Ma, Z. Jia, L. Meng, H. Yang, J. Zhang, W. Lai, J. Guo, X. Jiang, C. Cui and Y. Li, *Adv Funct Mater*, 2023, 33, 2210733.

[**13**] T. Todorov, O. Gunawan and S. Guha, *Mol Syst Des Eng*, 2016, 1, 370–376.

[**14**] J. Yang, W. Chen, B. Yu, H. Wang and D. Yan, *Org Electron*, 2012, 13, 1018–1022.

[**15**] L. Hafaifa, M. Maache, Z. Allam and A. Zebeir, *Results in Optics*, 2024, 14, 100596.

[**16**] Y. El Arfaoui, M. Khenfouch and N. Habiballah, *Journal of Optics (India)*, DOI:10.1007/S12596-023-01647-3.

[**17**] T. I. Alanazi, *Polymers 2023, Vol. 15, Page 2217*, 2023, 15, 2217.

[**18**] T. I. Alanazi and M. El Sabbagh, *Polymers (Basel)*, 2023, 15, 1823.

[**19**] H. A. El-Demsisy, A. Shaker, M. D. Asham, I. S. Ahmed and T. M. Abdolkader, *Silicon*, 2024, 16, 5337–5353.

[**20**] T. I. Alanazi, A. Shaker, M. Gad and M. Okil, *Phys Scr*, 2024, 99, 065516.

[**21**] M. R. Khan and B. Jarząbek, DOI:10.20944/PREPRINTS202308.0912.V1.

[**22**] S. Abdelaziz, A. Zekry, A. Shaker and M. Abouelatta, *Opt Mater (Amst)*, 2022, 123, 111893.

[**23**] N. Shrivastav, S. Kashyap, J. Madan, M. K. A. Mohammed, M. K. Hossain and R. Pandey, *Optik (Stuttg)*, 2023, 281, 170821.

[**24**] N. Shrivastav, J. Madan, R. Pandey and A. E. Shalan, *RSC Adv*, 2021, 11, 37366–37374.

[**25**] M. K. Hossain, G. F. I. Toki, A. Kuddus, M. H. K. Rubel, M. M. Hossain, H. Bencherif, M. F. Rahman, M. R. Islam and M. Mushtaq, *Scientific Reports 2023 13:1*, 2023, 13, 1–24.

[**26**] S. Rai, B. K. Pandey and D. K. Dwivedi, *Opt Mater (Amst)*, 2020, 100, 109631.

[**27**] S. Rai, B. K. Pandey and D. K. Dwivedi, *Journal of Physics and Chemistry of Solids*, 2021, 156, 110168.

[**28**] A. M. N. ABENA, A. T. NGOUPO, F. X. A. ABEGA and J. M. B. NDJAKA, *Chinese Journal of Physics*, 2022, 76, 94–109.

[**29**] E. Puente-López and M. Pal, *Optik (Stuttg)*, 2023, 272, 170233.

[**30**] L. Hafaifa, M. Maache and M. W. Bouabdelli, *Journal of Theoretical and Applied Physics*, 2024, 18, 182435–182436.

[**31**] L. R. Karna, R. Upadhyay and A. Ghosh, *Sci Rep*, 2023, 13, 1–19.

[**32**] M. Islam, T. Ahmed, S. U. D. Shamim, A. A. Piya and A. Basak, *Chemistry of Inorganic Materials*, 2024, 2, 100034.

[**33**] K. A. Bangash, S. A. A. Kazmi, W. Farooq, S. Ayub, M. A. Musarat, W. S. Alaloul, M. F. Javed and A. Mosavi, *Micromachines 2021, Vol. 12, Page 518*, 2021, 12, 518.

[**34**] A. Rajagopal, K. Yao and A. K. Y. Jen, *Advanced Materials*, 2018, 30, 1800455.

[**35**] M. Zi, X. Chen, S. Tan, C. Weng and B. Zhao, *Chemical Engineering Journal*, 2022, 443, 136455.

[**36**] J. You, L. Dou, K. Yoshimura, T. Kato, K. Ohya, T. Moriarty, K. Emery, C. C. Chen, J. Gao, G. Li and Y. Yang, *Nat Commun*, 2013, 4, 1–10.

[**37**] W. Chen, Y. Wu, Y. Yue, J. Liu, W. Zhang, X. Yang, H. Chen, E. Bi, I. Ashraful, M. Grätzel and L. Han, *Science (1979)*, 2015, 350, 944–948.

[**38**] L. Dou, J. You, J. Yang, C. C. Chen, Y. He, S. Murase, T. Moriarty, K. Emery, G. Li and Y. Yang, *Nat Photonics*, 2012, 6, 180–185.

[**39**] Z. Jia, Q. Ma, Z. Chen, L. Meng, N. Jain, I. Angunawela, S. Qin, X. Kong, X. Li, Y. (Michael) Yang, H. Zhu, H. Ade, F. Gao and Y. Li, *Nat Commun*, 2023, 14, 1–11.

[**40**] O. Almora, D. Baran, G. C. Bazan, C. Berger, C. I. Cabrera, K. R. Catchpole, S. Erten-Ela, F. Guo, J. Hauch, A. W. Y. Ho-Baillie, T. J. Jacobsson, R. A. J. Janssen, T. Kirchartz, N. Kopidakis, Y. Li, M. A. Loi, R. R. Lunt, X. Mathew, M. D. McGehee, J. Min, D. B. Mitzi, M. K. Nazeeruddin, J. Nelson, A. F. Nogueira, U. W. Paetzold, N. G. Park, B. P. Rand, U. Rau, H. J. Snaith, E. Unger, L. Vaillant-Roca, H. L. Yip and C. J. Brabec, *Adv Energy Mater*, 2021, 11, 2002774.

[**41**] O. Almora, D. Baran, G. C. Bazan, C. Berger, C. I. Cabrera, K. R. Catchpole, S. Erten-Ela, F. Guo, J. Hauch, A. W. Y. Ho-Baillie, T. J. Jacobsson, R. A. J. Janssen, T. Kirchartz, N. Kopidakis, Y. Li, M. A. Loi, R. R. Lunt, X. Mathew, M. D. McGehee, J. Min, D. B. Mitzi, M. K. Nazeeruddin, J. Nelson, A. F. Nogueira, U. W. Paetzold, N. G. Park, B. P. Rand, U. Rau, H. J. Snaith, E. Unger, L. Vaillant-Roca, H. L. Yip and C. J. Brabec, *Adv Energy Mater*, 2021, 11, 2102526.

CHAPTER IV

MACHINE LEARNING-GUIDED DESIGN OF DUAL ETLS FOR ORGANIC SOLAR CELLS

IV.1 Introduction

The electron transport layer (ETL) significantly contributes to the performance of organic solar cells (OSC). It facilitates the extraction of electrons and influences the morphology of the active layer, which has a direct impact on the efficiency and stability of the device [1,2].The materials used as ETL are generally classified into three categories: polymers (PFN, PEI, PEIE), small organic molecules (PDINN, PDINO), and inorganic materials (ZnO, TiOx, SnOx) [3].

Among these, metal oxides such as ZnO, TiO_2, and SnO_2 are particularly valued for their good optical and electronic properties, stability, and ease of implementation [4,5]. These materials are often used in inverted architectures (iOPV), particularly due to their compatibility with the energy levels of all the layers, which influences the overall efficiency and stability of the device [6].

Several studies have highlighted the importance of ETL engineering to improve interfaces, charge extraction, and the lifespan of OSCs [7,8]. A well-controlled surface can notably limit moisture penetration, reduce interface defects, and lower energy barriers, which helps to limit recombinations and improve thermal stability [6]. Among the most common materials, [6,6]-Phenyl-C61-butyric acid methyl ester ($PC_{60}BM$) is widely used due to its excellent electronic mobility (~2×10^{-7} m^2 V^{-1} s^{-1}) and thermal stability (Tg ≈ 430 K), in addition to promoting a bicontinuous structure in the active layer [9].

Researchers like Aryal and Singh have studied the effects of double ETL structures, particularly the combination of organic and inorganic layers [10,11]. Their work highlights the importance of ETL optimization to improve charge extraction, thermal stability, and device lifespan. Despite these advances, challenges remain, particularly for flexible OSCs, whose performance still lags behind that of rigid devices [12].

Moreover, the integration of artificial intelligence in the photovoltaic field is intensifying, with a growing use of optimization algorithms and machine learning [13]. For example, S. Moulebhar et al. applied the NSGA-II algorithm to optimize the properties of materials in OSCs [14], while Danlong Zong et al. used genetic algorithms to design solar

absorbers **[15]**. Similarly, Tanvir Mahtab Khan et al. used machine learning to improve the performance of thin-film cells based on $Sb_2(S_xSe_{1-x})_3$ **[16]**.

This study aims to enhance the performance of an organic solar cell device through the use of a dual electron transport layer combining organic and inorganic materials.

IV.2 Physical Configuration of the Solar Cell

The simulation work was carried out using the SCAPS-1D software to evaluate the performance of organic solar cells based on the PM6:PY-IT photoactive layer. Initially, a conventional reference structure was simulated with the following configuration: ITO/PEDOT:PSS/PM6:PY-IT/PDINN/Ag, as illustrated in **Figure IV.1**.

To enhance the electron extraction and improve overall device performance, we proposed the integration of dual electron transport layers (ETLs) by combining organic and inorganic materials. Specifically, three combinations were investigated:

- PCBM/ZnO
- PCBM/SnO_2
- PCBM/TiO_2

These materials were selected based on their favorable energy level alignment with the conduction band minimum (CBM) and valence band maximum (VBM) of the active layer, ensuring efficient charge transport and minimal energy losses. All relevant physical and electronic parameters of the layers are summarized in **Tables IV.1 and IV.2**.

Simulations were performed under standard illumination conditions (AM1.5G solar spectrum, 1000 W/m²) and at an operating temperature of 300 K.

In the second part of this study, machine learning (ML) techniques were employed to predict the photovoltaic performance of devices incorporating the proposed dual ETLs. The primary goal was to determine the optimal organic/inorganic ETL combination and its corresponding thickness that would yield the best device efficiency. Several supervised ML algorithms were applied and evaluated, as detailed in Section II.4.

The database used**,** summarized in **Appendix A,** was generated using the SCAPS-1D simulator. It comprises a total of 882 samples, divided into two sets: a training set (70%) and a test set (30%). This strategy allows for the efficient training of models while validating their ability to generalize predictions, with the aim of optimizing both material selection and the overall performance of the cell.

Table IV. 1: Different layer optoelectronic parameters input.

Parameters	**PEDOT:PSS [17]**	**PM6:PY-IT [18]**	**PDINN [19]**
Thickness (µm)	0.03	0.2	0.03
Eg (eV)	1.6	1.69	2.24
χ (eV)	3.4	3.77	3.78
ε_r	3	3	5
N_c (cm^{-3})	2.2×10^{18}	1×10^{21}	1×10^{19}
N_v (cm^{-3})	1.8×10^{19}	1×10^{21}	1×10^{19}
μ_e (cm^2/Vs)	4.5×10^{-2}	1.97×10^{-4}	2×10^{-6}
μ_h (cm^2/Vs)	4.5×10^{-2}	1.97×10^{-4}	1×10^{-3}
N_A (cm^{-3})	1×10^{19}	0	0
N_D (cm^{-3})	0	0	2×10^{20}
N_t (cm^{-3})	1×10^{13}	0	1×10^{13}
Defect type	Acceptor {+/0}	/	Donor {+/0}
Capture cross section (e^-) (cm^2)	1×10^{-15}	/	1×10^{-14}
Capture cross section (h^+) (cm^2)	1×10^{-15}	/	1×10^{-14}

Table IV. 2:Input parameters of different ETLs used.

Parameters	**PCBM [17]**	**ZnO [18]**	**TiO2 [19]**	**SnO2 [20]**
Thickness (µm)	0.03	0.03	0.03	0.01
E_g (eV)	3	3.3	3.2	3.6
χ (eV)	3.9	4.4	4	4
ε_r	3.9	9	9	9
N_c (cm^{-3})	2.5×10^{21}	3.7×10^{18}	2×10^{18}	2.2×10^{18}
N_v (cm^{-3})	2.5×10^{21}	1.8×10^{19}	1.8×10^{19}	1.8×10^{19}
μ_e (cm^2/Vs)	2×10^{-1}	100	20	100
μ_h (cm^2/Vs)	2×10^{-1}	25	10	25
N_A (cm^{-3})	0	0	0	0
N_D (cm^{-3})	1×10^{17}	1×10^{15}	1×10^{15}	1×10^{15}
N_t (cm^{-3})	1×10^{15}	1×10^{15}	1×10^{15}	1×10^{15}
Defect type	Donor {+/0}	Donor {+/0}	Donor {+/0}	Donor {+/0}
Capture cross section (e^-) (cm^2)	1×10^{-14}	1×10^{-14}	1×10^{-14}	1×10^{-14}
Capture cross section (h^+) (cm^2)	1×10^{-14}	1×10^{-14}	1×10^{-14}	1×10^{-14}

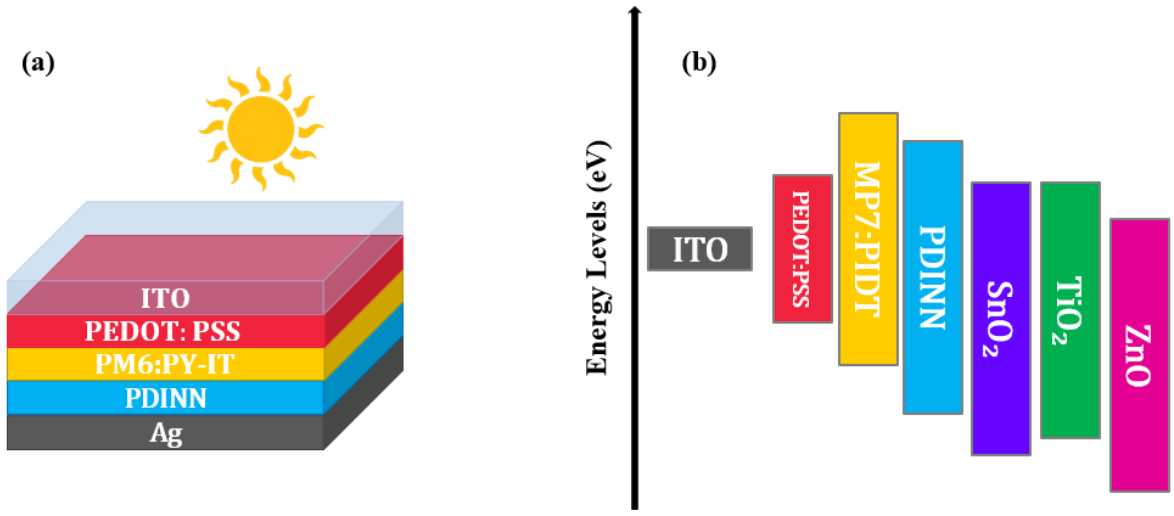

Figure IV. 1: (a) Schematic Representation and (b) Energy Level Diagram of the Modeled OSC.

IV.3 Results And Discussion

IV.3.1 Effect of Dual ETL Donor Doping on the Electrical and Photovoltaic Properties of the Solar Cell

The doping density of material is responsible for most of the electrical properties, such as conductivity and mobilities for the carriers, by increasing the carrier concentration [21].

In this context, we study the impact of doping in a double ETL structure on the performance of our organic solar cell by varying the doping density from 10^{15} to 10^{20} cm^{-3} as shown in **Figures IV.2, 3, 4**. The results show that increasing the doping density of PCBM significantly enhances the open-circuit voltage, especially beyond 10^{17} cm^{-3}, due to improved carrier extraction and reduced recombination. The secondary ETL materials (SnO_2, TiO_2, or ZnO) also contribute positively, though to a lesser extent, by facilitating better band alignment and interface quality. However, at very high doping levels ($\geq 10^{18}$ cm^{-3}), a slight decrease in V_{OC} and short-circuit current density may occur, likely caused by the formation of trap states, increased recombination centers, and reduced carrier mobility. The fill factor (FF) shows a notable improvement with increasing PCBM doping, reaching values above 79%, while the contribution of the metal oxides remains moderate but stabilizing. Consequently, the power

conversion efficiency (PCE) follows a similar trend, peaking around 21%, confirming the importance of doping optimization **[22–24]**.

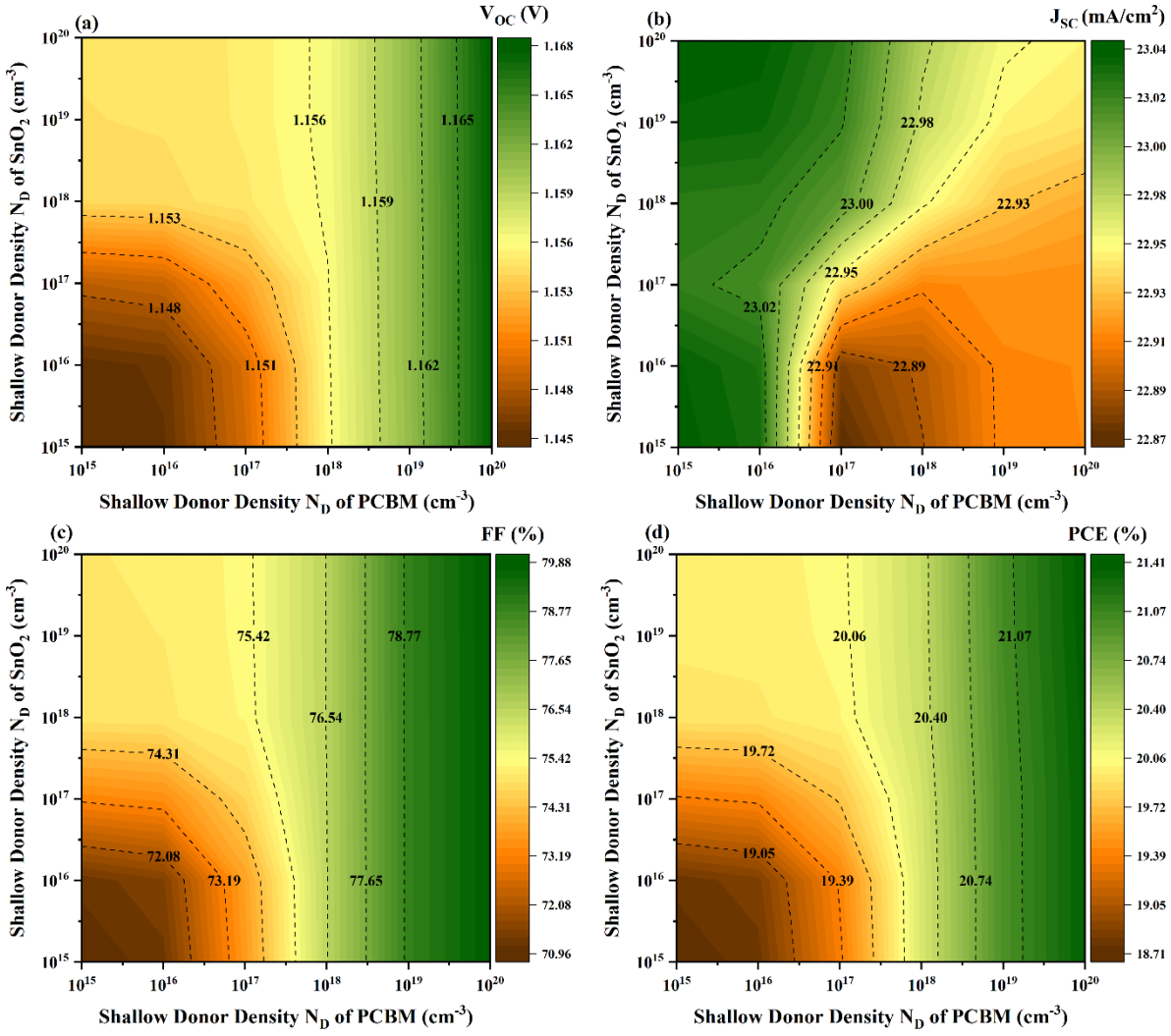

Figure IV. 2: Contour Analysis of Key Photovoltaic Parameters in PCBM/SnO_2 Dual Transport Layer Devices :(a) V_{OC}, (b) J_{SC}, (c) FF, and (d) PCE.

In conclusion, the results demonstrate that doping PCBM has a more pronounced impact on enhancing the overall performance of the solar cell compared to doping the metal oxide layers. An optimal configuration is achieved by combining high doping levels in the PCBM with moderate doping in the metal oxides, which leads to significant improvements in V_{OC}, FF, and PCE while limiting current losses. However, excessive doping beyond a certain threshold can be detrimental, as it increases carrier trapping and introduces parasitic effects such as the Burstein–

Moss shift, which alters the band structure and may hinder efficient carrier extraction. Therefore, precise control and balance of the doping levels in both ETLs are essential to ensure high performance without compromising device stability and charge transport efficiency.

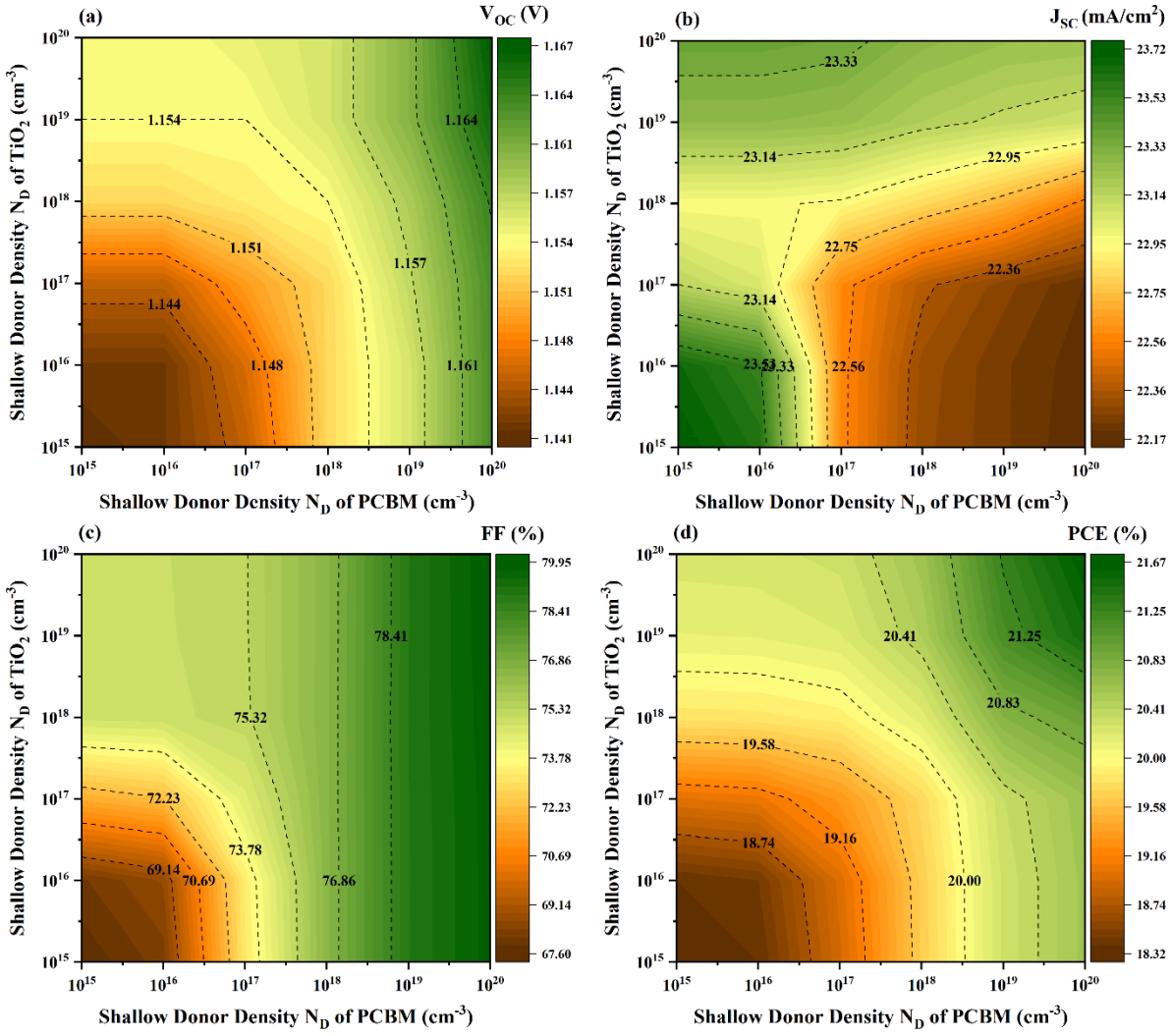

Figure IV. 3: Contour Analysis of Key Photovoltaic Parameters in PCBM/TiO_2 Dual Transport Layer Devices :(a) V_{OC}, (b) J_{SC}, (c) FF, and (d) PCE.

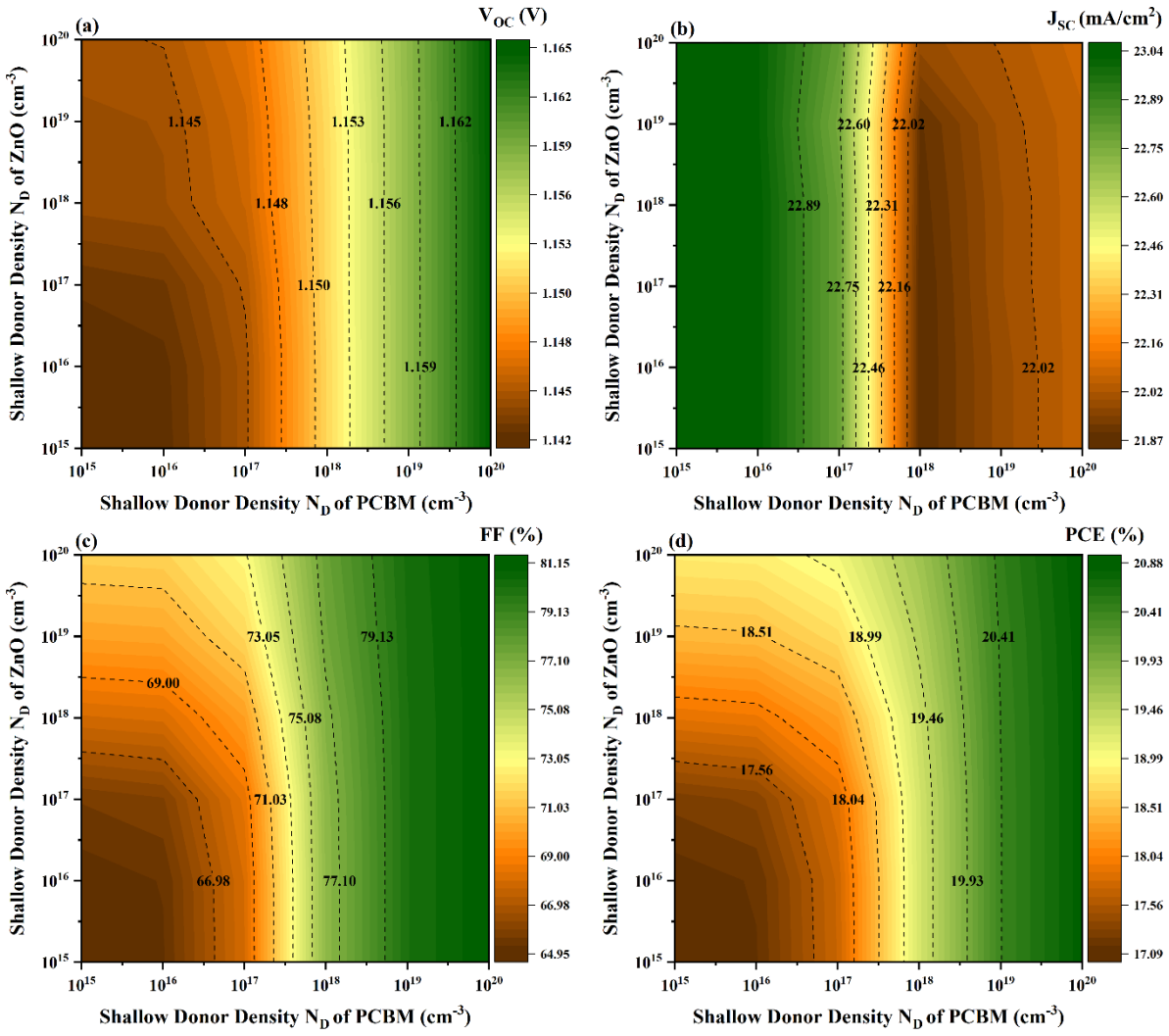

Figure IV. 4: Contour Mapping of the Effects of PCBM/ZnO Dual Layer Donor Doping Density on OSC Output Parameters.

IV.3.2 Role of Interface Defects in Charge Transport and Solar Cell Efficiency

Interfacial defects are structural or electronic irregularities located at the junction between two materials, generally between the organic absorber and the transport layers. They result from poor alignment of crystal lattices, chemical incompatibility, or the adsorption of residues or residual solvents. These defects can act as carrier traps, promoting non-radiative recombination mechanisms, thereby reducing the efficiency of solar cells. In the case studied, the interfacial defects at the PCBM/SnO_2, PCBM/ZnO, and PCBM/TiO_2 depict in **Figure IV.5, 6 and 7.**

The interfaces are of the neutral type, with an effective capture cross-section for electrons and holes of 1×10^{-19} cm^2, which implies a moderate probability of recombination. Their energy level, situated 0.6 eV above the valence band (Ev), corresponds to deep traps, likely to significantly affect the dynamics of minority carriers. At low density ($Nt \leq 10^{11}$ cm^{-3}), their impact remains negligible.

However, when the density exceeds 10^{12} to 10^{13} cm^{-3}, a gradual decrease in conversion efficiency is observed, particularly a reduction in the fill factor, indicating an increase in interfacial recombination and a deterioration in charge transport. Although the open-circuit voltage is relatively stable for the PCBM/TiO_2 and PCBM/SnO_2 interfaces, it decreases slightly for PCBM/ZnO, indicating increased sensitivity to deep defects. Interestingly, a transient improvement in the FF at low density is observed for PCBM/ZnO, suggesting a partial passivation effect by shallow defects that temporarily reduce leakage current losses. Nevertheless, at higher densities, these defects become clearly detrimental, promoting SRH recombination, limiting charge extraction, and overall degrading the solar cell performance [25,26].

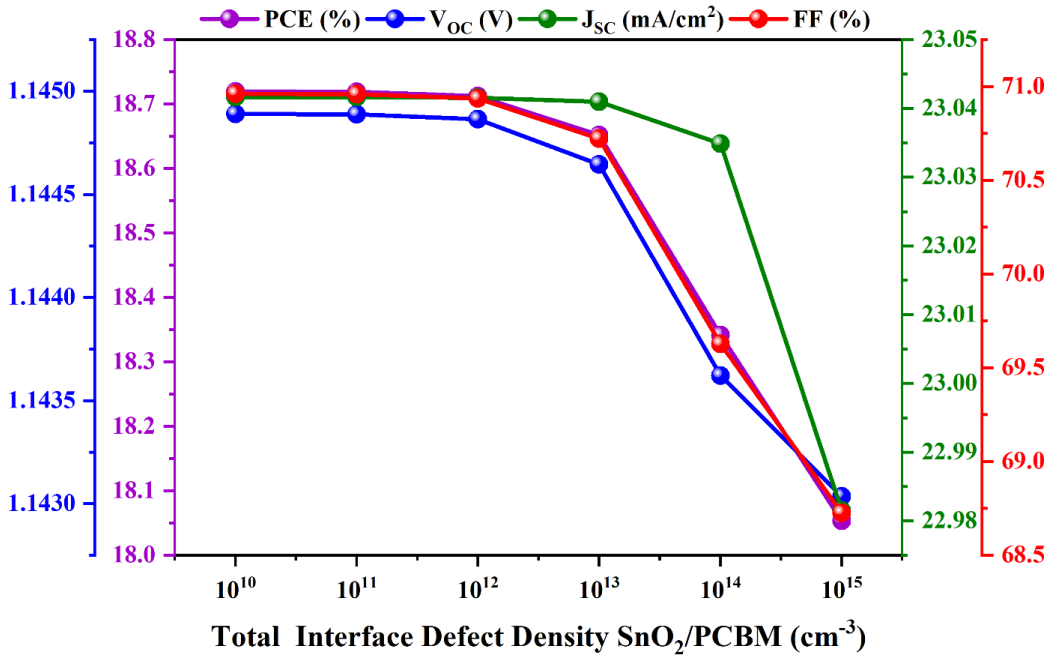

Figure IV. 5: Impact of Interface Defect Density at the SnO_2/PCBM Junction on Organic Solar Cell Performance.

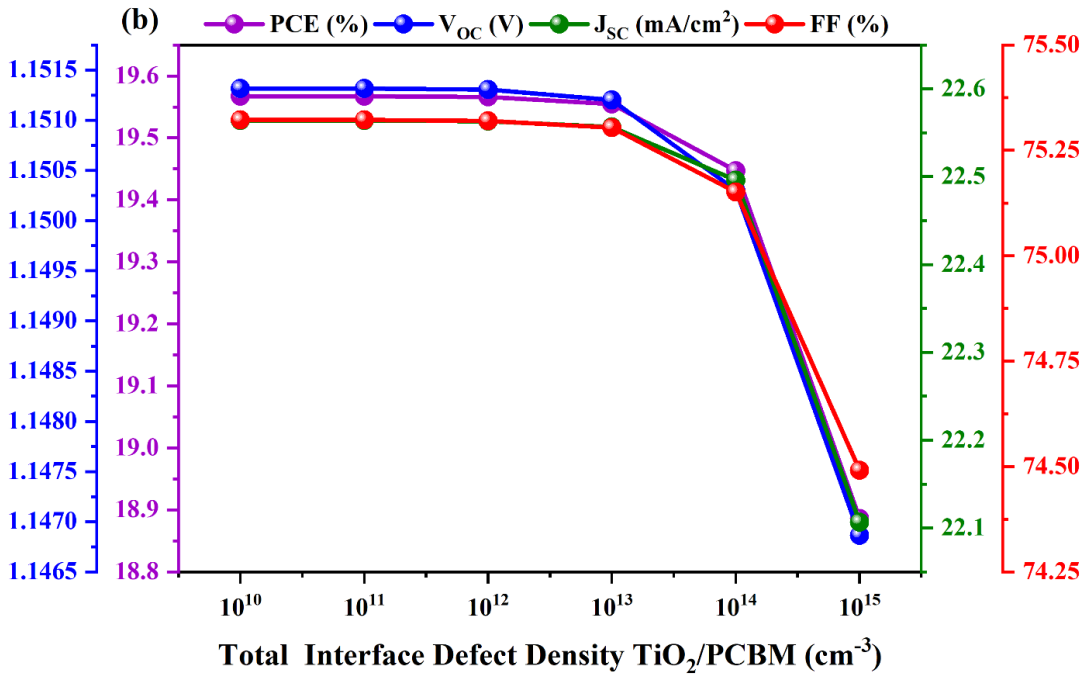

Figure IV. 6: Effect of Interfacial Defects at the TiO_2/PCBM Layer on the Electrical Characteristics of Organic Photovoltaics.

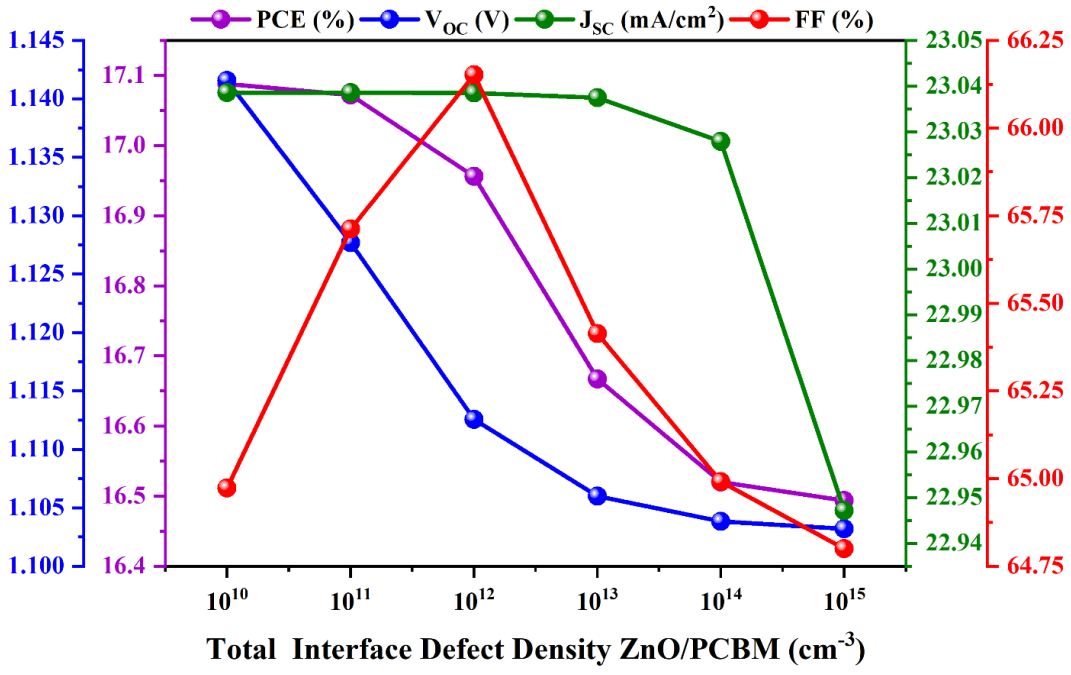

Figure IV. 7: Performance Degradation Induced by Interface Defects at the ZnO/PCBM Electron Transport Layer.

IV.3.3 Frequency-Dependent Impedance Response of Dual-ETL Architectures

Electrochemical Impedance Spectroscopy (EIS) is a powerful technique used to probe the interfacial and dynamic properties of solar cells, particularly organic solar cells (OSCs). It relies on the application of a low-amplitude sinusoidal signal (typically ≤10 mV) superimposed on a direct current voltage, usually the open-circuit voltage, over a wide range of frequencies ranging from a few mHz to several MHz. This frequency sweep is essential because each physicochemical process within the cell manifests at different time scales and thus at distinct frequency ranges: high frequencies are associated with rapid electronic transport and contact resistances, while low frequencies reveal slower phenomena such as charge accumulation, ionic diffusion, or slow recombination**[27,28].**

The system's response is recorded in the form **(IV.1)** of a complex spectrum

$$\boldsymbol{Z(\omega) = Z' + jZ''} \qquad \textbf{(IV.1)}$$

where $\boldsymbol{Z'}$ represents the real part (pure resistance) and $\boldsymbol{Z''}$ the imaginary part, associated with capacitive or inductive behaviors.

This response is generally represented in a Nyquist diagram, where each semicircle reflects a dominant process.

To analyze these spectra, an equivalent circuit is used **(Figure IV.8)**, modeling the cell with elements such as series resistance **(R_s)**, transport resistance **(R_t)**, geometric capacitance **(C_g)**, and recombination resistance **(R_{rec})** coupled with a chemical capacitance **(C_μ)**. The size of the semicircle, particularly at low frequency, is proportional to **R_{rec}**: the larger it is, the lower recombination, which is favorable to the cell's efficiency **[29,30]**.

The results illustrated in **Figure IV.9** reveal that, the devices integrating different hybrid ETLs (PCBM/SnO_2, PCBM/ZnO, PCBM/TiO_2) show distinct impedance profiles. Notably, the PCBM/TiO_2 structure exhibits the largest Nyquist arc, indicating a higher recombination resistance, translating to an effective reduction of interfacial recombination. suggests better electronic selectivity at the interface, enhancing the overall photovoltaic performance of the device.

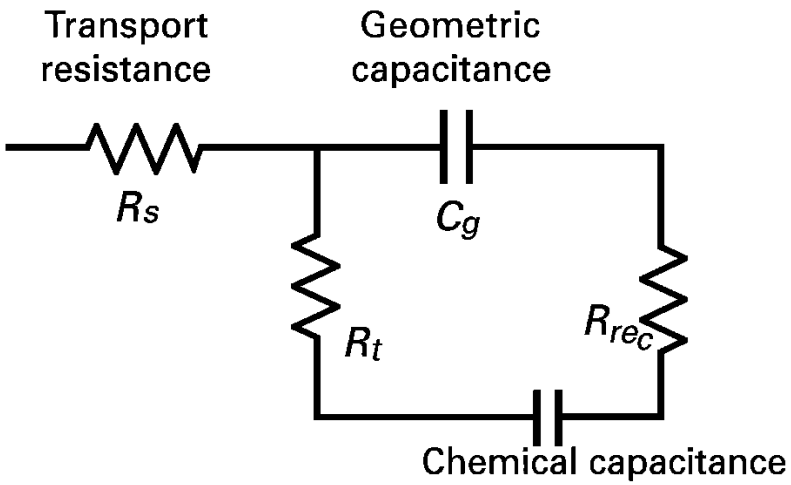

Figure IV. 8: Equivalent circuit model used in impedance spectroscopy.

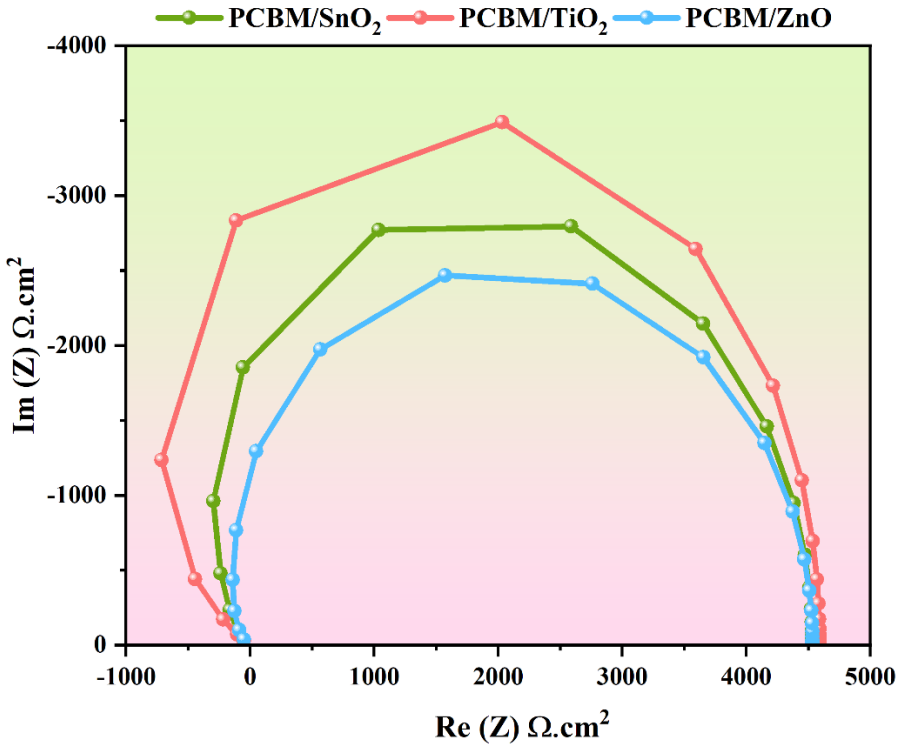

Figure IV. 9: Comparison of Nyquist Plots for Three Dual ETL-Based Organic Solar Cells.

IV.3.4 Role of Mott–Schottky Analysis in Understanding Device Operation

The Mott–Schottky technique is an essential electrochemical method for analyzing the internal properties of a solar cell, particularly the doping density and the built-in potential (V_{bi}). It involves applying a variable direct current (DC) voltage to the device while superimposing a small alternating current (AC) signal at a fixed frequency (usually 1 kHz) in order to measure the differential capacitance of the device**[27,31–33]**.

The results are then represented as a curve of $1/C^2$ as a function of the voltage (V), called the Mott–Schottky curve.
This curve allows us to extract two key pieces of information:

- The slope of the obtained line is proportional to the inverse of the doping density N_A. A steeper slope means a lower density of fixed charges (dopants) in the depletion region of the semiconductor.
- The intersection with the voltage axis gives the built-in potential (V_{bi}), which corresponds to the natural internal electric potential of the device in the absence of light. It is this voltage that separates the photogenerated electrons and holes in opposite directions, which is fundamental for the operation of a solar cell, mathematically, the relationship is given by:

$$\frac{1}{C^2} = \frac{2(V_{bi}-V)}{A^2 e \epsilon_0 N_A} \quad \textbf{(IV.2)}$$

where:

C is the measured capacity, **V** the applied voltage, **A** the surface of the device, **q** the elementary charge, $\boldsymbol{\epsilon_0}$ the dielectric constant of the material, the doping density is represented by $\mathbf{N_A}$.

In the case of your organic solar cell with a dual electron transport layer (dual ETL), such as PCBM/TiO_2, PCBM/SnO_2, or PCBM/ZnO the depletion zone forms at the interface between the active layer (the donor/acceptor blend like PM6:Y6) and the ETL layer.

It is in this region that the fixed charges (dopants) dominate, and where free carriers (electrons and holes) are almost absent. This zone plays a crucial role in the separation and extraction of charges.

Figure IV.10 presents the comparative Mott–Schottky plots, which demonstrate that:

- The PCBM/TiO_2 device exhibits the highest built-in potential (V_{bi}= 0.70V), indicating a stronger internal electric field. This enhances the separation of photogenerated charge carriers and reduces recombination losses, which can improve the open-circuit voltage (Voc) and overall device performance.
- The PCBM/SnO_2 device, with an intermediate V_{bi} of 0.55 V, shows moderate performance, with reasonably efficient charge collection, though less optimal than with TiO_2.
- In contrast, the PCBM/ZnO structure has the lowest V_{bi} (0.44 V), indicating a weaker internal field. This can hinder charge separation and increase recombination losses, ultimately leading to reduced solar cell efficiency.

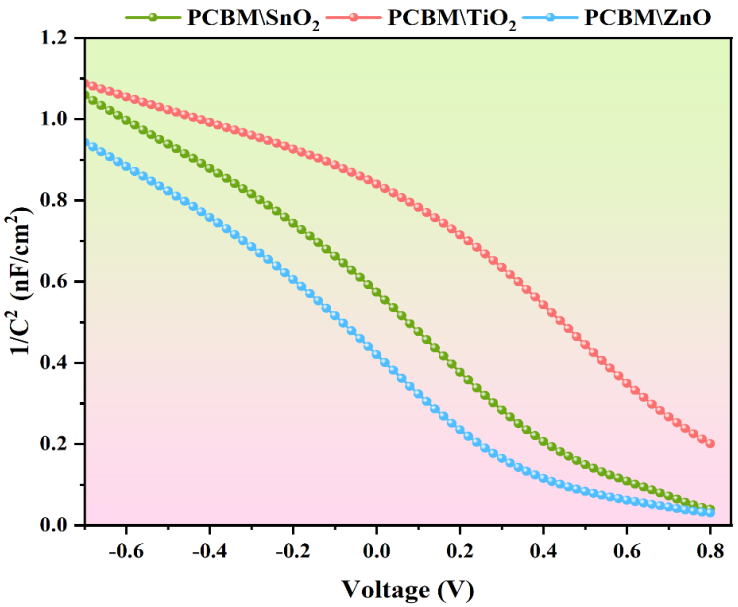

Figure IV. 10: Mott–Schottky ($1/C^2$) Analysis of Organic Solar Cells with Different Dual ETL Configurations

In conclusion, the Mott–Schottky technique not only allows for the quantification of doping density in the depletion region but also estimates the internal electric field (via V_{bi}), which is a direct indicator of the cell's ability to efficiently separate charges.

IV.3.5 Comparative Analysis of J–V Characteristics and External Quantum Efficiency

The current density–voltage (J–V) characteristic is a key tool for evaluating the performance of organic solar cells, as it provides direct insight into essential parameters such as open-circuit voltage, short-circuit current density, fill factor, and power conversion efficiency. **Table IV.2 and Figure IV.11** present a comparison between our device architectures integrating dual electron transport layers (ETLs) and single-ETL-based reference structures reported in the literature, all employing the same PM6:PY-IT active layer.

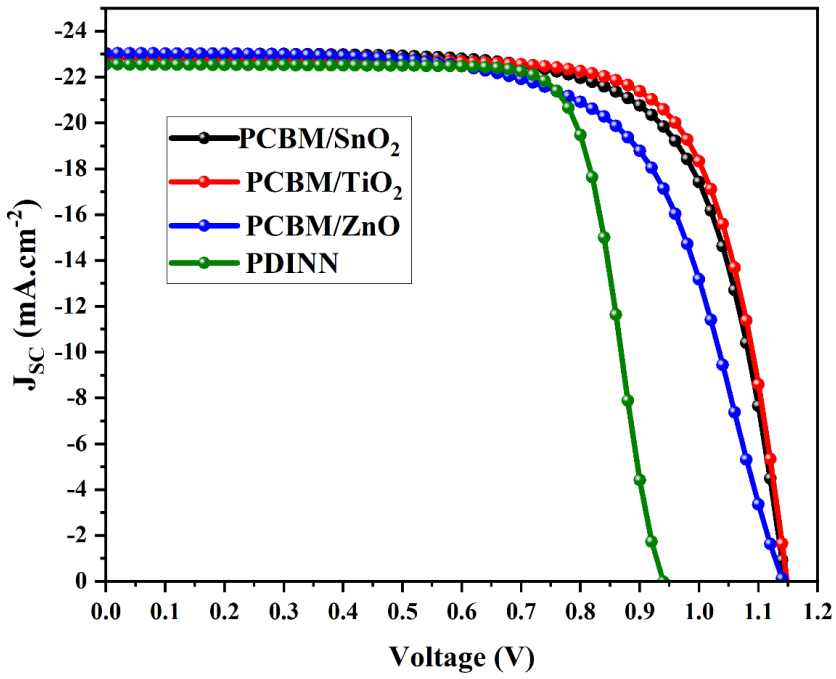

Figure IV. 11: Comparison of J–V Characteristics for Organic Solar Cells with Single and Dual ETL Structures.

Our configurations, namely ITO/PEDOT:PSS/PM6:PY-IT/PCBM/SnO_2/Ag and ITO/PEDOT:PSS/PM6:PY-IT/PCBM/TiO_2/Ag, demonstrate the highest efficiencies, reaching 18.72% and 19.35%, respectively. These devices benefit from elevated V_{OC} values

(~1.14 V), stable J_{SC}, and high fill factors ranging from 70% to 73%, indicating efficient charge collection and reduced losses. In comparison, the ITO/PEDOT:PSS/PM6:PY-IT/PCBM/ZnO/Ag structure also delivers a similar V_{OC} (1.1416 V) and J_{SC}, but its lower fill factor (64.97%) limits its PCE to 17.09%. This suggests that, although ZnO supports effective charge generation, it is less efficient in sustaining charge transport compared to SnO_2 and TiO_2.

Overall, our dual ETL architectures outperform the single ETL counterparts, highlighting the advantage of combining PCBM with a metal oxide. This hybrid strategy promotes improved charge extraction and reduced recombination, offering a promising pathway toward enhancing the performance of organic solar cells **[34,35]**.

Figure IV.12 illustrates the external quantum efficiency (EQE) spectra as a function of wavelength for devices incorporating four different electron transport layer configurations: PCBM/SnO_2, PCBM/TiO_2, PCBM/ZnO, and single-layer PDINN. All devices exhibit relatively high EQE values across the visible range (approximately 350–800 nm), with characteristic spectral peaks indicating efficient photo-response. Beyond 800 nm, a marked decrease in EQE is observed, corresponding to the limited absorption capacity of the active layer in the near-infrared region.

Notably, the device with a single PDINN layer shows lower EQE values compared to those based on dual ETLs. Among the latter, the PCBM/SnO_2, PCBM/TiO_2, and PCBM/ZnO configurations display comparable spectral responses, though slight variations in peak intensities are evident. These results confirm the beneficial impact of combining organic (PCBM) and inorganic ETLs on light harvesting and charge collection efficiency, leading to enhanced overall device performance.

Table IV. 3: Metrics Performance of different dual ETL OSCs.

Devices	V_{OC} (V)	J_{SC} (mA.cm^{-2})	FF (%)	PCE (%)	Reference
ITO/PEDOT:PSS/PM6:PY-IT/PDINN/Ag	0.9396	22.552	76.75	16.26	**This work**
ITO/PEDOT:PSS/PM6:PY-IT/PCBM/SnO2/Ag	1.1449	23.041	70.96	18.72	**This work**
ITO/PEDOT:PSS/PM6:PY-IT/ PCBM/TiO2/Ag	1.1483	22.848	73.76	19.35	**This work**
ITO/PEDOT:PSS/PM6:PY-IT/PCBM/ZnO/Ag	1.1416	23.038	64.97	17.09	**This work**
ITO/PEDOT:PSS/PM6:PY-IT/PDINN/Ag	0.94	23.70	74.19	16.52	**[36]**
ITO/MoO3/PM6:PY-IT/ZnO/Ag	0.928	23.40	67.70	14.68	**[37]**
ITO/MoO3/PM6:PY-IT/IZO/Ag	0.931	24.13	67.43	15.11	**[37]**
ITO/PEDOT:PSS/PM6:PY-IT/PFN-Br/Ag	0.924	22.96	70.6	14.93	**[38]**

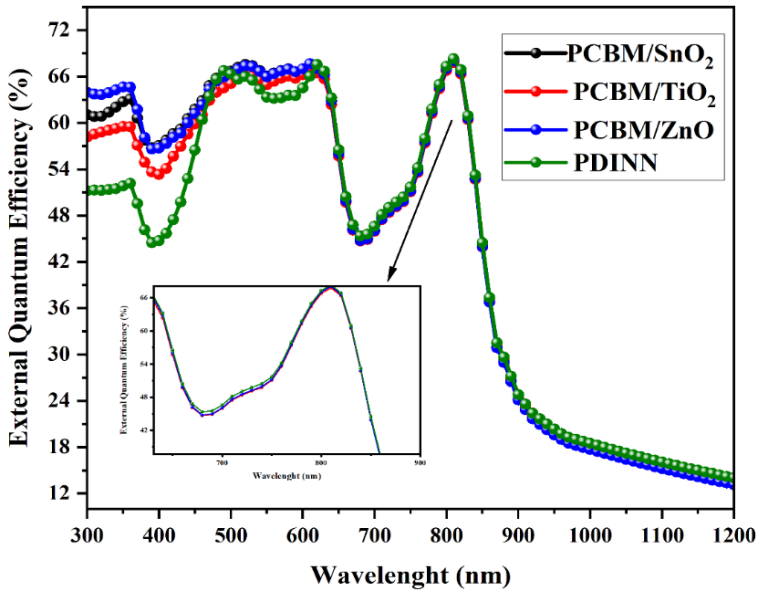

Figure IV. 12: External Quantum Efficiency Spectra of Organic Solar Cells with Single and Dual ETLs.

IV.3.6 Modeling and Prediction of Photovoltaic Performance Using ML

Following the application of various machine learning algorithms, the predictive performance of each model is summarized in **Table IV.3** and **Figure IV.13**. The results show that the linear regression model exhibits limited performance, with a coefficient of determination R^2 = 0.6589 and a root mean square error (RMSE) of 2.1818, indicating a low predictive capability for solar cell performance.

In contrast, models based on decision trees and boosting techniques such as Random Forest, XGBoost, and Gradient Boosting demonstrate significantly better accuracy. The XGBoost Regressor stands out as the most effective model, achieving an R^2 of 0.9957 and a very low RMSE of 0.2446. It is closely followed by the Random Forest Regressor (R^2 = 0.9955, RMSE = 0.2509), while the Gradient Boosting Regressor reaches an R^2 of 0.9590, with a slightly higher RMSE (0.7568).

The K-Nearest Neighbours (k-NN) model also yields strong results (R^2 = 0.9855), although its error is somewhat higher. Finally, the Decision Tree Regressor, despite achieving perfect accuracy on the training data (R^2 = 1), presents a notable risk of overfitting, as reflected by a slightly lower selection R^2 value (0.9950).

Table IV. 4: Evaluating the Performance of the ML Model.

Models	R^2 (Test)	RMSE (Test)	R^2 (Train)	R^2(Selection)
Linear Regression	0.6589	2.1818	0.6664	0.658914
Random Forest Regressor	0.9955	0.2509	0.9996	0.994876
K-Neighbors Regressor	0.9855	0.4494	0.9948	0.985531
Gradient Boosting	0.959	0.7568	0.9715	0.958958
XGBoost Regressor	0.9957	0.2446	1	0.995713
Decision Tree Regressor	0.995	0.265	1	0.995003

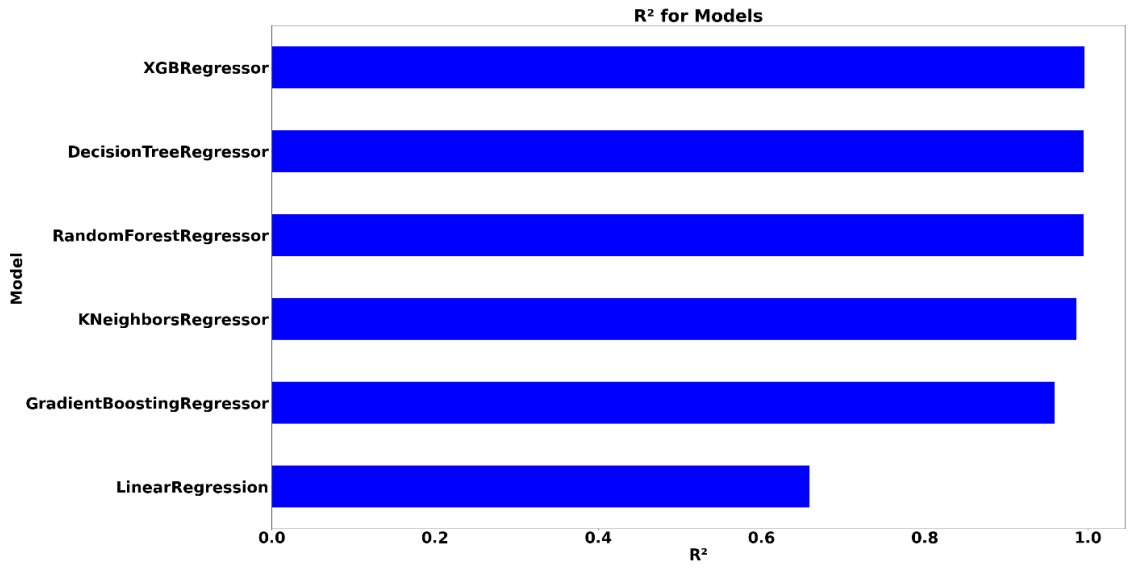

Figure IV. 13: R^2 Scores for Various Regression Models Applied to Solar Cell Performance Prediction.

IV.3.6.1 Correlation Analysis Between PCE and Input Parameters

The correlation matrix is used to analyze the relationships between the different variables in the dataset. As shown in **Figure IV.14**, certain variables exhibit strong positive or negative correlations with the power conversion efficiency (PCE), providing valuable insights into their influence on device performance. For instance, the electron affinity of the inorganic ETL layer (*electron_affinity2*) shows a strong negative correlation with PCE (–0.74), indicating that a higher electron affinity tends to reduce the efficiency of the solar cell. Similarly, the bandgap of the organic material (*bandgap2*) shows a moderate negative correlation (–0.097), suggesting a relatively weaker influence on PCE.

On the other hand, parameters such as *electron_mobility2* and *hole_mobility1.1* show an almost perfect positive correlation (≈1), reflecting that they vary in a very similar way, likely due to material properties or model assumptions. Regarding the layer thicknesses, *thickness1* corresponds to the inorganic ETL and *thickness2* to the organic ETL. Both show negligible correlation with PCE, indicating that within the studied range, variations in layer thicknesses have limited direct impact on overall device performance.

These correlation trends help to identify the key physical and chemical parameters that influence solar cell efficiency, guiding future optimization efforts in the design of dual ETL architectures.

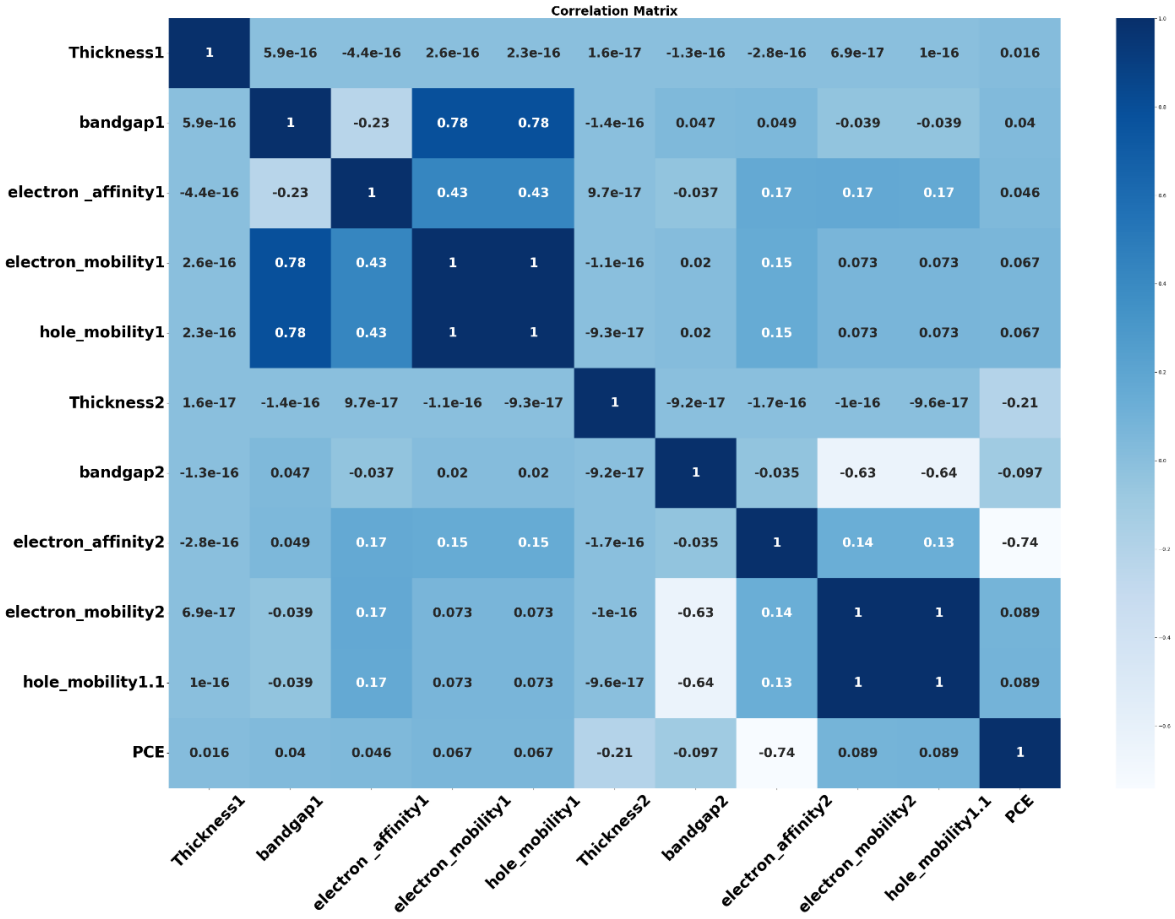

Figure IV. 14: Interrelationship Between Power Conversion Efficiency and Input Variables.

IV.4 Conclusion

This chapter demonstrated the significant impact of integrating dual electron transport layers (ETLs) on the performance of photovoltaic devices compared to single ETL configurations. The PCBM/TiO_2 combination delivered the highest performance, achieving a PCE of 19.35%, an open-circuit voltage of 1.14 V, and a fill factor of 73.76%, confirming the benefit of dual ETLs in improving charge extraction and interface quality.

Additionally, machine learning techniques were applied to predict and analyze device performance. Using SCAPS-1D simulations, multiple regression models were trained and evaluated. Among them, XGBoost achieved the best predictive accuracy ($R^2 = 0.9957$; RMSE = 0.2446), demonstrating the effectiveness of ML in capturing the complex relationships between material parameters and device efficiency.

This method enables the prediction of device efficiency and the identification of the optimal combination of organic/inorganic dual ETLs.

Despite these promising outcomes, further experimental validation is necessary to confirm the reliability and generalizability of the predicted results.

Bibliography

[**1**] A. El Khalfi, K. Ridani, L. Et-Taya, A. El Boukili, N. Mansour, L. Elmaimouni, M. F. Rahman and A. Benami, *Langmuir*, 2024, 40, 20352–20367.

[**2**] H. Dahiya, R. Suthar, K. Khandelwal, S. Karak and G. D. Sharma, *ACS Appl Electron Mater*, 2022, 4, 5119–5143.

[**3**] X. Liu, Y. Ji, Z. Xia, D. Zhang, Y. Cheng, X. Liu, X. Ren, X. Liu, H. Huang, Y. Zhu, X. Yang, X. Liao, L. Ren, W. Tan, Z. Jiang, J. Lu, C. McNeill and W. Huang, *Advanced Science*, 2024, 11, 2402158.

[**4**] Dr. R. Kumar, A. Dhar, Dr. A. Banerjee and Dr. S. Mondal, Eds., DOI:10.22271/ED.BOOK.2938.

[**5**] S. Chapagain, *Electronic Theses and Dissertations*, DOI:10.18297/etd/4297.

[**6**] V. Magnin and K. N'konou, *EPJ Photovoltaics*, 2024, 15, 29.

[**7**] J. Hu, X. Xiong, W. Guan and H. Long, *Mater Today Energy*, 2021, 21, 100769.

[**8**] S. Y. Zhang, X. Guo, Y. M. Xu, Y. Jiao, Z. H. Lin, J. C. Zhang, J. Y. Ouyang, L. X. Guo, Y. Hao and J. J. Chang, *Rare Metals*, 2025, 44, 3069–3079.

[**9**] Z. Chen, M. El, A. Boudia and C. Zhao, *Energies 2025, Vol. 18, Page 167*, 2025, 18, 167.

[**10**] W. B. Tarique, M. H. Rahaman, S. S. Dipta, A. H. Howlader and A. Uddin, *Nanomanufacturing 2024, Vol. 4, Pages 81-98*, 2024, 4, 81–98.

[**11**] U. K. Aryal, V. M. Arivunithi, S. S. Reddy, J. Kim, Y. S. Gal and S. H. Jin, *Org Electron*, 2018, 63, 222–230.

[**12**] Y. Li, M. Sha and S. Huang, *Coatings 2024, Vol. 14, Page 1031*, 2024, 14, 1031.

[**13**] F. Li, X. Peng, Z. Wang, Y. Zhou, Y. Wu, M. Jiang and M. Xu, *Energy & Environmental Materials*, 2019, 2, 280–291.

[**14**] S. Moulebhar, C. Bendenia, H. Merad-Dib, S. Bendenia, S. Merabet and S. A. Khantar, *Physica Status Solidi (A) Applications and Materials Science*, 2024, 222, 2400654.

[**15**] D. Zong, L. Zhu, Z. Yu, Y. Liu, Y. Li and Y. Wang, *Results Phys*, 2023, 50, 106559.

[**16**] T. M. Khan, O. Saidani and S. R. Al Ahmed, *RSC Adv*, 2024, 14, 27749–27763.

[**17**] P. Subudhi and D. Punetha, *Sci Rep*, DOI:10.1038/S41598-023-33419-1.

[**18**] T. I. Alanazi, *Polymers 2023, Vol. 15, Page 2217*, 2023, 15, 2217.

[**19**] T. I. Alanazi, *Polymers (Basel)*, 2023, 15, 2217.

[**20**] Y. K. Singh, D. K. Dwivedi, P. Lohia, R. Pandey, J. Madan, M. K. Hossain, S. Agarwal, S. Rai and E. A. Al-Almar, *Journal of Physics and Chemistry of Solids*, 2024, 192, 112096.

[**21**] A. Pandya, A. K. Sharma, M. Bhatt, P. K. Jha, K. Sangani, N. K. Chourasia and R. K. Chourasia, *Energy Storage*, DOI:10.1002/EST2.70001.

[**22**] Z. Khan, M. Noman, S. Tariq Jan and A. Daud Khan, *Solar Energy*, 2023, 257, 58–87.

[**23**] W. Zhao, S. Li, H. Yao, S. Zhang, Y. Zhang, B. Yang and J. Hou, *J Am Chem Soc*, 2017, 139, 7148–7151.

[**24**] W. Abdelaziz, A. Shaker, M. Abouelatta and A. Zekry, *Opt Mater (Amst)*, 2019, 91, 239–245.

[**25**] K. S. Nithya and K. S. Sudheer, *Optik (Stuttg)*, 2020, 217, 164790.

[**26**] P. K. Dakua, R. K. Dash, A. Laidouci, S. Bhattarai, U. Dudekula, S. Kashyap, V. Agarwal and A. N. Z. Rashed, *J Electron Mater*, 2024, 53, 2015–2025.

[**27**] M. A. Benatallah, A. Elmohri, Y. I. Bouderbala, M. W. Alam and S. Rabhi, *Adv Theory Simul*, 2025, 8, 2401161.

[**28**] A. Mortadi, E. El Hafidi, M. Monkade and R. El Moznine, *Mater Sci Energy Technol*, 2024, 7, 158–165.

[**29**] V. H. Tran, S. H. Eom, S. C. Yoon, S. K. Kim and S. H. Lee, *Org Electron*, 2019, 68, 85–95.

[**30**] F. Pirri, W. Binte Tarique, H. Rahaman, S. Safat Dipta, A. H. Howlader and A. Uddin, *Nanomanufacturing 2024, Vol. 4, Pages 81-98*, 2024, 4, 81–98.

[**31**] T. Kirchartz, W. Gong, S. A. Hawks, T. Agostinelli, R. C. I. MacKenzie, Y. Yang and J. Nelson, *Journal of Physical Chemistry C*, 2012, 116, 7672–7680.

[**32**] T. A. Kareem, DOI:10.12693/APhysPolA.129.409.

[**33**] B. Qi, Z. G. Zhang and J. Wang, *Sci Rep*, 2015, 5, 1–8.

[**34**] H. Dahiya, R. Suthar, K. Khandelwal, S. Karak and G. D. Sharma, *ACS Appl Electron Mater*, 2022, 4, 5119–5143.

[**35**] S. Shoaee, M. Stolterfoht and D. Neher, *Adv Energy Mater*, 2018, 8, 1703355.

[**36**] Q. Ma, Z. Jia, L. Meng, H. Yang, J. Zhang, W. Lai, J. Guo, X. Jiang, C. Cui and Y. Li, *Adv Funct Mater*, 2023, 33, 2210733.

[**37**] X. Liu, Y. Ji, Z. Xia, D. Zhang, Y. Cheng, X. Liu, X. Ren, X. Liu, H. Huang, Y. Zhu, X. Yang, X. Liao, L. Ren, W. Tan, Z. Jiang, J. Lu, C. McNeill and W. Huang, *Advanced Science*, 2024, 11, 2402158.

[**38**] Z. Luo, T. Liu, R. Ma, Y. Xiao, L. Zhan, G. Zhang, H. Sun, F. Ni, G. Chai, J. Wang, C. Zhong, Y. Zou, X. Guo, X. Lu, H. Chen, H. Yan and C. Yang, *Advanced Materials*, 2020, 32, 2005942.

CHAPTER V

ORGANIC ELECTRONICS FOR EMBEDDED AND PORTABLE APPLICATIONS

V.1 Introduction

In a world where portable electronic devices such as smartphones, smartwatches, and smart glasses are increasingly integrated into our daily lives, the issue of their power supply has become a major challenge **[1]**. Traditionally, these devices rely on replaceable or rechargeable batteries, but this solution presents several drawbacks, including limited lifespan and environmental impacts related to their production and disposal. It is in this context that self-powered technology comes into play **[2]**.

Self-powered technology enables a device to operate autonomously by harvesting energy directly from its environment, thereby eliminating the need for an external power source. Among the various forms of energy available for powering portable devices, solar energy stands out as one of the most promising. Indeed, sunlight is an abundant and renewable resource capable of providing enough energy to power small electronic devices **[3]**.

Solar panels, which convert light energy into electricity, are one of the most efficient solutions for charging portable devices autonomously. Thanks to advancements in photovoltaic materials and storage technologies, it is now possible to integrate solar panels into compact and portable systems capable of providing continuous power to smartphones and other electronic devices **[4,5]**. **Figure V.1** presents various applications of the self-powered module.

This chapter focuses on the use of solar energy to charge a smartphone via a solar panel. The goal is to demonstrate how self-powered technology based on solar energy can offer a sustainable and efficient solution for powering portable devices while overcoming the limitations of traditional battery systems.

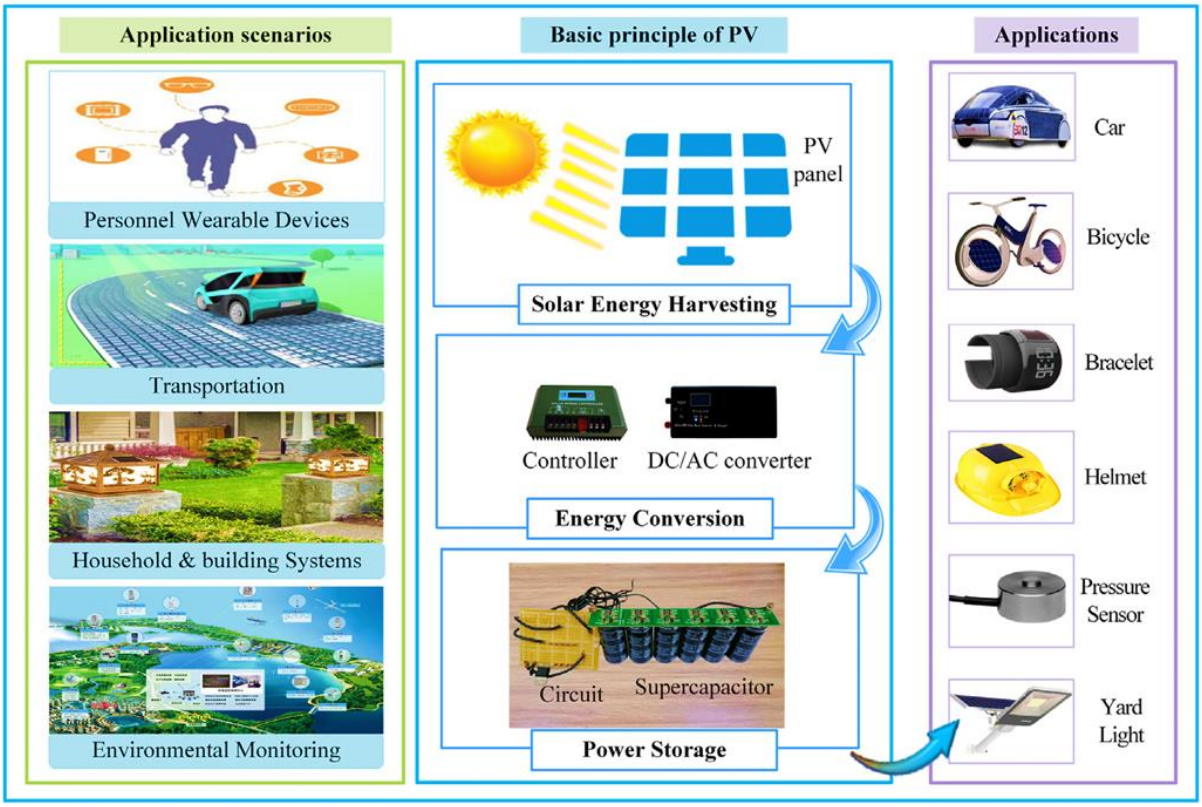

Figure V. 1: System Architecture of the Photovoltaic Self-Powered Module [6].

V.2 Description of the Cell Used

In this project, the organic solar cell studied in detail in Chapter IV shows promising performance, with an open-circuit voltage of 1.43 V, a short-circuit current density of 23.03 mA/cm², and a fill factor of 73.76%, all on an active area of 1 cm² under standard irradiance of 1000 W/m². These parameters suggest a theoretical maximum output power of approximately 24 mW per cell.

To power the target system, a smartphone charger, an output voltage of 5 V and a current of at least 100 mA (corresponding to about 0.5 W) are required.

This implies connecting multiple cells in series and/or parallel to achieve the necessary voltage and power, along with a DC-DC converter to adapt the voltage to the charging electronics' requirements.

V.3 Simulation Tools

MATLAB (MATrix LABoratory) is an interactive numerical computing environment widely used in scientific and technical fields. It is primarily designed for matrix manipulation, algorithm development, data visualization, and the modeling and simulation of complex systems. Thanks to its user-friendly interface and integrated libraries, MATLAB has become an essential tool for engineers, researchers, and scientists [7].

In this work, we used MATLAB version 2023 to develop and execute a series of custom simulation scripts. These scripts were essential for performing advanced numerical calculations, interpreting modeling data, and simulating the behavior of various components of the studied system, including solar cells and power supply circuits.

The scripting approach offers outstanding flexibility in automating repetitive tasks, managing input parameters, and conducting comparative result analyses. It also ensures clear traceability of the simulation process, which facilitates adjustments and optimizations according to the specific needs of the project. As such, the use of MATLAB in this context significantly contributed to the reliability and accuracy of the results obtained.

V.4 Sizing of the OPV Panel

To size the organic photovoltaic (OPV) module based on the individual cell's performance studied in Chapter V, we start by estimating the maximum current provided by a single cell**:**

$$\mathbf{I_{cell} = J_{sc} \times area = 23.03\ mA/cm^2 \times 1\ cm^2 = 23.03\ mA} \qquad \textbf{(V.1)}$$

and its theoretical maximum power:

$$\mathbf{P_{cell} = V_{oc} \times I_{cell} \times FF = 1.43\ V \times 23.03\ mA \times 0.7376 \approx 24\ mW} \qquad \textbf{(V.2)}$$

To reach the target voltage of 5 V, the number of cells to connect in series is calculated as:

$$\mathbf{n_{series} = \left\lceil \frac{V_{target}}{V_{oc}} \right\rceil = \left\lceil \frac{5}{1.43} \right\rceil = 4} \qquad \textbf{(V.3)}$$

and to achieve a current of at least 100 mA, the number of parallel strings required is:

$$\mathbf{n_{parallel} = \left\lceil \frac{I_{target}}{I_{cell}} \right\rceil = \left\lceil \frac{100}{23.03} \right\rceil = 5} \quad \textbf{(V.4)}$$

Leading to a total number of cells:

$$\mathbf{n_{total} = n_{series} \times n_{parallel} = 4 \times 5 = 20} \quad \textbf{(V.5)}$$

resulting in a total active area of 20 cm² (e.g., 4.0 cm × 5.0 cm).

The estimated theoretical output of the module dimensioned this way is:

- Open-circuit voltage (V_{OC} total): 5.72 V (4 × 1.43 V)
- Maximum current: 115.2 mA (5 × 23.03 mA)
- Estimated maximum power: 485.83 mW calculated using

$$\mathbf{P_{total} = V_{total} \times I_{total} \times FF} \quad \textbf{(V.6)}$$

These results show that the module can meet the objective of supplying at least 100 mA at 5 V for a smartphone charger, provided a DC-DC converter is integrated to regulate the output voltage precisely to 5.0 V, as illustrated by the 5S×4P solar panel configuration in **Figure V.2**.

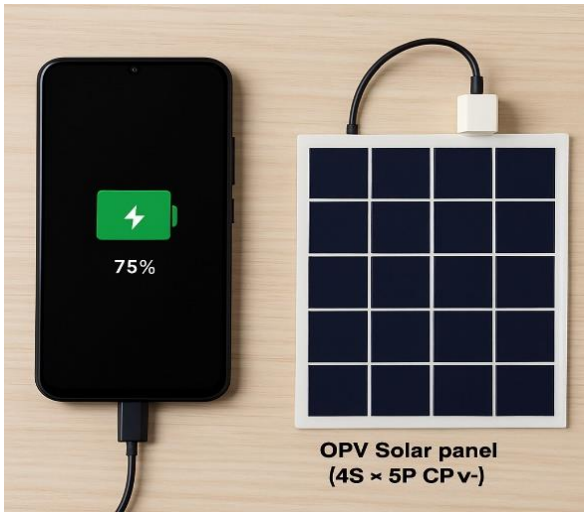

Figure V. 2: Smartphone Charging Using an Organic Photovoltaic (OPV) Solar Panel in a 4-Series × 5-Parallel Configuration.

V.5 Charging System Design

V.5.1 System Diagram

The circuit depict in **Figure V.3** presents an efficient solution for charging batteries using solar power. By harnessing energy from a photovoltaic (PV) panel, the system ensures optimal performance while maintaining peak efficiency throughout the charging process.

With the integration of key components such as a MPPT controller and a DC-DC converter, this solar charging circuit maximizes energy transfer, making it an ideal choice for sustainable and reliable battery charging in various applications.

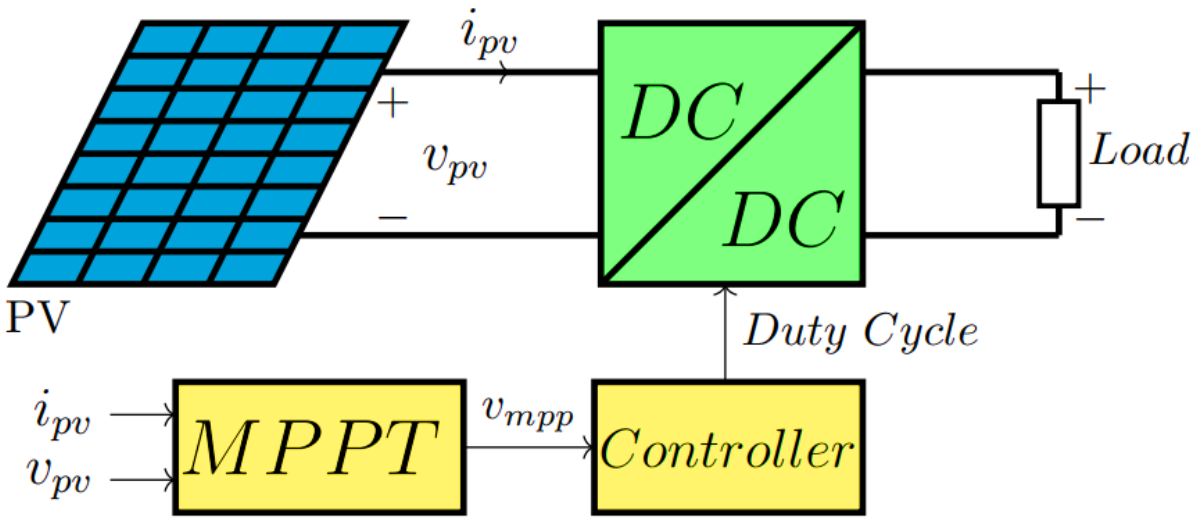

Figure V. 3: Schematic representation of the PV-based charging circuit implementing Maximum Power Point Tracking (MPPT).

V.5.2 Component Selection

To ensure the stability and efficiency of the system, it is essential to carefully select the components. Here is a selection suitable for the needs of this solar charging system:

- **DC-DC Converter (Buck-Boost):** A buck-boost regulator such as the LM2596 or LTC3780 is recommended. These regulators are capable of handling the wide voltage range supplied by the solar panel (depending on sunlight conditions) while providing a stable 5 V output,

ideal for charging devices via the USB port. Block Diagram of the Buck–Boost Converter is depicted in **Figure V.4**.

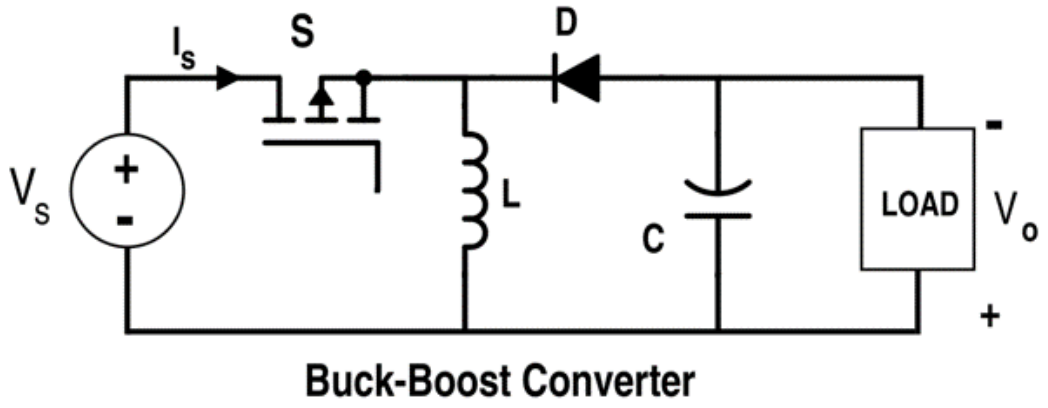

Figure V. 4: Buck–Boost Converter System Layout.

- **MOSFET (Transistor):** The IRF540N transistor is an excellent choice for the converter. With a low R_{ds}(on) resistance, it minimizes conduction losses and optimizes the energy efficiency of the system. It can handle high currents, which is crucial for managing the constant current flows in the system.
- **Schottky Diode:** The 1N5819 Schottky diode is ideal for this type of system. It offers a low forward voltage drop and reduced switching losses, helping improve system efficiency. This diode is particularly well-suited for applications involving high current levels.
- **Inductor & Capacitor:** Passive components such as the inductor and capacitor are essential for smoothing the output current and filtering out fluctuations due to the converter's switching. The values of these components are chosen based on the switching frequency, typically between 50 kHz and 100 kHz, to ensure effective and stable voltage regulation.
- **Battery**: A Li-ion battery with a nominal voltage of 3.7 V and a capacity of 1200–2000 mAh is ideal for storing the energy generated by the solar panel. It is recommended to use a Battery Management System (BMS) module to protect the battery from overcharging, deep discharging, and short circuits, thereby ensuring extended lifespan and enhanced safety.
- **USB Port**: For charging electronic devices, a 5 V USB module with a 1 A output current is standard. This module ensures compatibility with most devices, including smartphones and small electronic gadgets.

V.6 Performance Analysis: I-V, P-V Curves, Output Voltage, and Overall System Efficiency

The simulated I-V and P-V characteristics shown in **Figure V.5** demonstrate that the designed OPV module can deliver a maximum open-circuit voltage of 5.72 V and a short-circuit current of 115.2 mA, matching the requirements of a 5 V, 100 mA USB charger. The P-V curve confirms that the maximum power point is near the designed operating voltage, indicating efficient power extraction under standard illumination conditions.

The calculated overall system efficiency, including converter and battery losses, reaches approximately 19.68%. As illustrated in **Figure V.6**, the power flow analysis and overall system efficiency demonstrate that despite the limited efficiency of organic solar cells, the system can deliver sufficient power for low-power devices such as smartphones or sensors, provided sufficient sunlight and an adequate storage strategy.

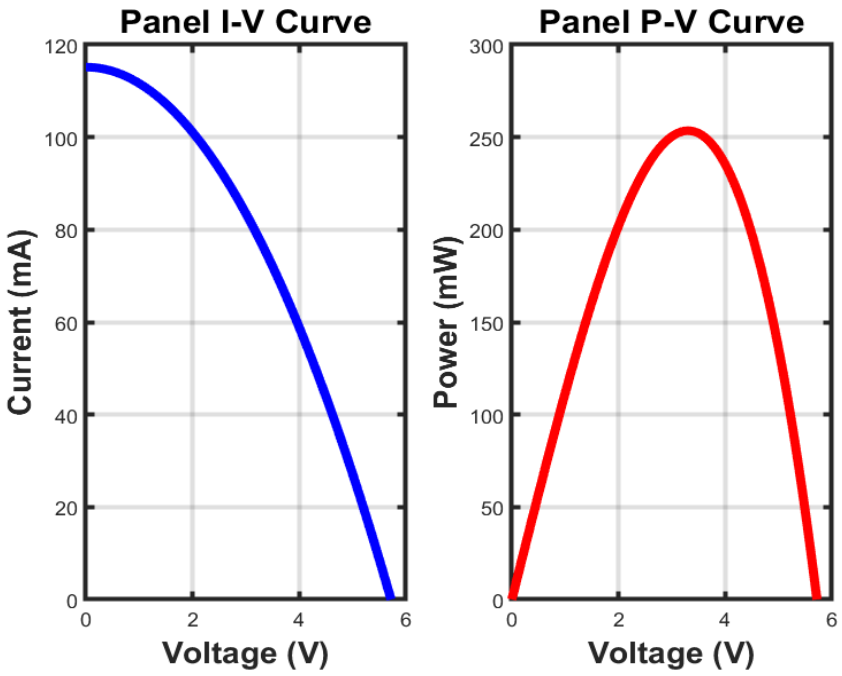

Figure V. 5: I–V and P–V Characteristics of the OPV Solar Panel under Standard Test Conditions.

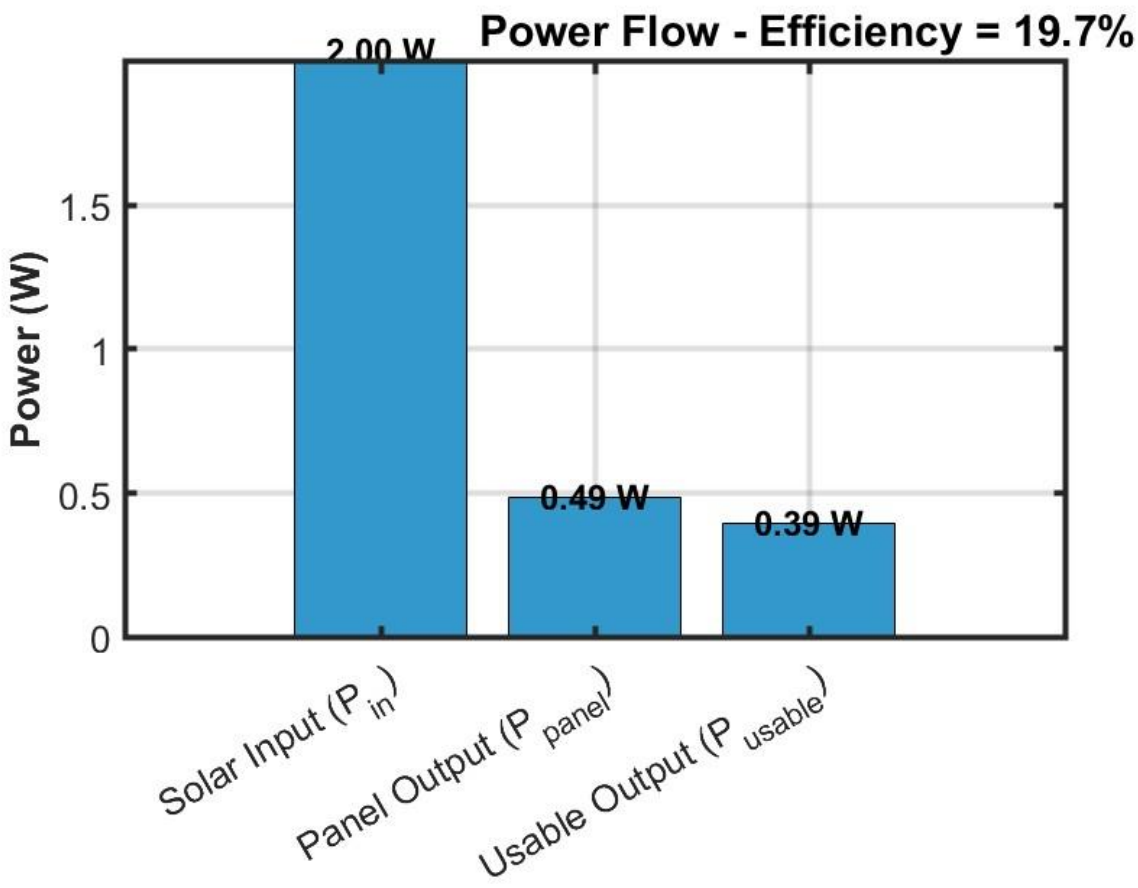

Figure V. 6: Power Flow Analysis and Overall System Efficiency.

V.7 Experimental Feasibility and Technical Limitations

From a practical standpoint, the feasibility of building this system experimentally is realistic using commercially available OPV materials and standard DC-DC converters. However, technical limitations include the inherent stability issues of OPV cells under prolonged UV exposure, potential performance degradation at elevated temperatures, and the need for precise charge control circuitry to prevent overcharging or deep discharging of the battery[8–10].

In summary, while the simulation confirms the system's ability to meet basic charging requirements, further experimental validation is necessary to account for environmental variations, long-term reliability, and to optimize the electrical and thermal design for real-world deployment.

V.8 Conclusion

This chapter has demonstrated the feasibility of using organic photovoltaic (OPV) technology to power a smartphone charging system, highlighting the potential of self-powered solutions based on solar energy for portable devices.

By carefully designing and dimensioning the OPV module to meet the voltage and current requirements of a typical USB charger, and by incorporating efficient power conversion and storage elements, it is possible to create a compact, sustainable, and autonomous charging system.

This approach not only reduces dependence on grid electricity but also extends the usability of mobile devices in off-grid or remote locations. However, challenges such as the long-term stability of organic solar cells and the need for precise power management must still be addressed to fully realize the potential of this technology in commercial applications.

Overall, the integration of OPV systems for charging portable electronics represents a promising step toward more sustainable and energy-independent solutions.

Bibliography

[**1**] C. Xu, Y. Song, M. Han and H. Zhang, *Microsystems & Nanoengineering 2021 7:1*, 2021, 7, 1–14.

[**2**] M. Jahandar, S. Kim and D. C. Lim, *ChemSusChem*, 2021, 14, 3449–3474.

[**3**] E. A. da Silva, W. M. C. Filho, M. R. Cavallari and O. H. Ando Junior, *Electronics 2024, Vol. 13, Page 2518*, 2024, 13, 2518.

[**4**] M. O. Qays, Y. Buswig, M. L. Hossain and A. Abu-Siada, *Energies 2020, Vol. 13, Page 3434*, 2020, 13, 3434.

[**5**] H. Ling, S. Liu, Z. Zheng and F. Yan, *Small Methods*, 2018, 2, 1800070.

[**6**] D. Hao, L. Qi, A. M. Tairab, A. Ahmed, A. Azam, D. Luo, Y. Pan, Z. Zhang and J. Yan, *Renew Energy*, 2022, 188, 678–697.

[**7**] MATLAB, https://www.mathworks.com/products/matlab.html, (accessed 8 August 2025).

[**8**] S. H. Kim, H. J. Son, S. H. Park, J. S. Hahn and D. H. Kim, *Solar Energy Materials and Solar Cells*, 2016, 144, 187–193.

[**9**] B. Fan, W. Gao, X. Wu, X. Xia, Y. Wu, F. R. Lin, Q. Fan, X. Lu, W. J. Li, W. Ma and A. K. Y. Jen, *Nat Commun*, 2022, 13, 1–11.

[**10**] H. Zhao, N. Prine, S. Kundu, G. Ma and X. Gu, *JACS Au*, 2024, 4, 4334–4344.

General Conclusion & Perspectives

Conclusion and Perspectives

This research is set within the current context of the energy transition, where the pursuit of efficient, lightweight, flexible, and low-cost photovoltaic solutions has become a major challenge. Organic solar cells (OSCs) stand out for their adaptability and potential for integration into innovative applications, but their performance and stability still require improvement.

The main objective of this thesis was to explore, through numerical approach, various strategies aimed at improving the performance of multilayer, flexible OSCs, while considering concrete applications through the design of self-powered modules.

First, an in-depth state-of-the-art review positioned OSCs in relation to other photovoltaic technologies, highlighting their advantages and limitations. Then, the use of the SCAPS-1D simulator, coupled with optimization methods and Machine Learning, made it possible to identify solar cell configurations offering higher efficiencies.

In **Chapter III**, tandem OSCs were optimized using two strategies. The first strategy focused on adjusting the thickness and defect density of the top and bottom active layers, which significantly enhanced charge generation and transport, leading to a **PCE** of **24.5% (J_{SC} = 15.1 mA/cm², V_{OC} = 2.11 V, FF = 76.7%)**. The second strategy involved the modification and optimization of transport layers, which achieved a **PCE** of **22.83%,** with a high V_{OC} of **2.34 V** and an excellent fill factor of **83%**. These results demonstrate the strong potential of tandem structures when combining active-layer engineering with optimized transport interfaces.

In **Chapter IV**, a Machine Learning-based approach was developed to predict the compatibility between organic and metal oxide electron transport layers (ETLs). This predictive modeling identified optimal combinations, and the **PCBM/TiO_2** bilayer ETL delivered the best performance, reaching a **PCE** of **19.35%**, an open-circuit voltage of **1.14 V**, and a fill factor of **73.76%.** This confirmed the role of dual ETLs in improving charge extraction and reducing interfacial recombination.

Finally, the practical integration of an OPV solar panel into a smartphone charging system illustrated the application potential of these devices using MATLAB. The prototype achieved an overall system efficiency of ~19.7% (including converter and storage losses), validating the feasibility of autonomous organic photovoltaic modules for powering portable electronics and embedded systems.

The results obtained underline the value of a multidisciplinary approach combining modeling, algorithmic optimization, artificial intelligence, and experimental validation. This synergy paves the way for new perspectives, such as the exploration of emerging materials, the optimization of long-term OSC stability, and their large-scale deployment in flexible and integrated energy applications.

✓ **Perspectives**

The results obtained open several avenues for research and development:

- **Improving long-term stability**: study OSC degradation under real conditions (UV, humidity, extreme temperatures) and develop more effective encapsulations.
- **Exploring new active materials**: investigate next-generation non-fullerene donors and acceptors to broaden the absorbed spectral range and increase efficiency.
- **Large-scale multi-objective optimization**: use artificial intelligence algorithms to simultaneously optimize PCE, cost, stability, and recyclability.
- **Integration into intelligent embedded systems**: couple OSCs with sensors, IoT systems, or autonomous medical devices.
- **Development of transparent or semi-transparent modules**: for applications in BIPV (Building Integrated Photovoltaics) and flexible electronics.
- **Transition to roll-to-roll manufacturing**: validate the industrial feasibility of optimized architectures in a large-scale production context.

This integrated approach, combining modeling, optimization, and experimental validation, provides a solid foundation for the next generation of organic photovoltaic devices capable of meeting growing demands for efficiency, durability, and integration into everyday life.

Appendix - A

Appendix A: Dataset for Machine Learning Prediction

The following dataset was generated from numerical simulations (SCAPS-1D). It includes the main physical and electrical parameters of the two electron transport layers **(thickness, bandgap, electron affinity, charge carrier mobilities**) as well as the corresponding **power conversion efficiencies (PCE)**. This dataset was used as the **input data** for training, validation, and prediction with the machine learning models developed in this thesis.

N	Thickness1	bandgap1	electron _affinity1	electron_ mobility1	hole_ mobility1	Thickness2	bandgap2	electron_ affinity2	electron_ mobility2	hole_ mobility1	PCE
1	0.02	3.2	4	20	10	0.02	2	3.9	0.2	0.2	**1.91E+01**
2	0.02	3.2	4	20	10	0.03	2	3.9	0.2	0.2	**1.90E+01**
3	0.02	3.2	4	20	10	0.04	2	3.9	0.2	0.2	**1.87E+01**
4	0.02	3.2	4	20	10	0.05	2	3.9	0.2	0.2	**1.85E+01**
5	0.02	3.2	4	20	10	0.06	2	3.9	0.2	0.2	**1.82E+01**
6	0.02	3.2	4	20	10	0.07	2	3.9	0.2	0.2	**1.81E+01**
7	0.02	3.2	4	20	10	0.08	2	3.9	0.2	0.2	**1.79E+01**
8	0.03	3.2	4	20	10	0.02	2	3.9	0.2	0.2	**1.92E+01**
9	0.03	3.2	4	20	10	0.03	2	3.9	0.2	0.2	**1.94E+01**
10	0.03	3.2	4	20	10	0.04	2	3.9	0.2	0.2	**1.93E+01**
	.	.	.	.	.	.	.	.	.	.	.
	.	.	.	.	.	.	.	.	.	.	.
	.	.	.	.	.	.	.	.	.	.	.
	.	.	.	.	.	.	.	.	.	.	.
881	0.06	3.3	4.4	100	25	0.06	2.8	4.17	0.000019	0.0000002	**1.59E+01**
882	0.08	3.3	4.4	100	25	0.07	2.8	4.17	0.000019	0.0000002	**1.64E+01**
883	0.06	3.3	4.4	100	25	0.07	2.8	4.17	0.000019	0.0000002	**1.56E+01**

Appendix - B

Appendix B : PV System Model for Battery Charging

The following Simulink model illustrates the photovoltaic (PV) system used for charging a battery.

The system consists of a **PV** array connected to a **DC–DC converter** (**MOSFET switch, diode, and RLC filter**) controlled through a **maximum power point tracking (MPPT)** algorithm.The output of the converter is used to charge a battery, while key parameters such as voltage, current, power, and state of charge (**SOC**) are monitored**.**This configuration was employed to analyze the dynamic behavior of the PV–battery system under different irradiance and temperature conditions.

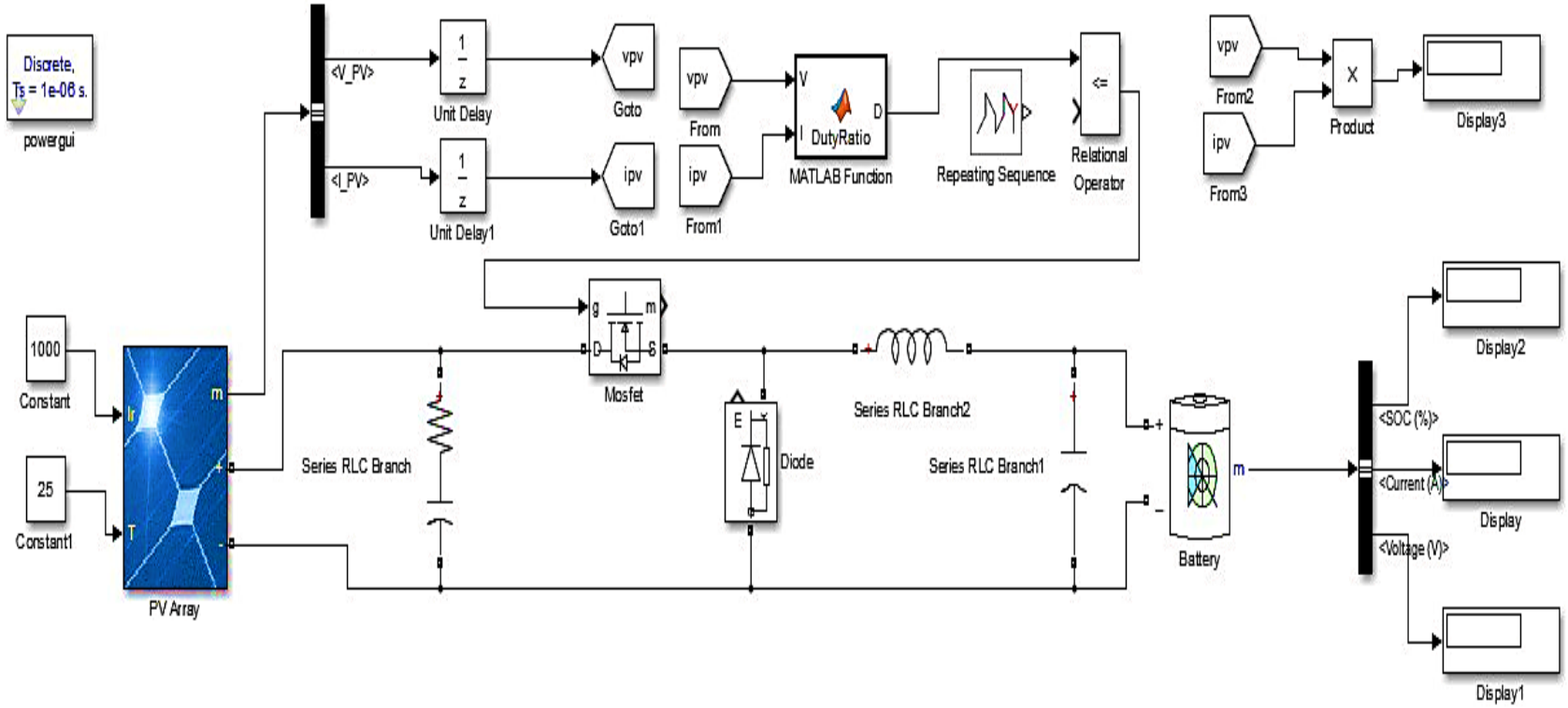

ECS Journal of Solid State Science and Technology, 2025 **14** 086002
2162-8777/2025/14(8)/086002/12/$40.00

Modeling and Performance Improvement of Organic Tandem Solar Cells Using SCAPS-1D Simulator

Samia Moulebhar,[1,2,z] Chahrazed Bendenia,[1,2] Souhila Bendenia,[2] Hanaa Merad-Dib,[2] Sarra Merabet,[1,2] and Sid Ahmed Khantar[1,2]

[1]*Laboratory of Electromagnetism and Guided Optics, Faculty of Science and Technology, University Abd El Hamid Ibn Badis, Mostaganem, 27000, Algeria*
[2]*Analysis, Modeling, Advanced Materials for Renewable Energies Laboratory, Faculty of Science and Technology, University Abd El Hamid Ibn Badis, Mostaganem, 27000, Algeria*

This study presents a simulation-based optimization of a two-terminal (2 T) all-polymer tandem solar cell using SCAPS-1D. The structure incorporates PM7:PIDT as the top sub-cell and PM6:PY-IT as the bottom sub-cell. Two key optimization strategies were investigated to enhance device performance. The first involved adjusting the top absorber's thickness and defect concentration, with optimal values of 200 nm and 10^{11} cm^{-3}, respectively. This configuration yielded a Jsc of 15.1 mA cm^{-2}, Voc of 2.11 V, FF of 76.7%, and a PCE of 24.5%. The second strategy focused on interfacial engineering by replacing the electron transport layers: TiO_2 was used in the bottom cell and PDINN in the top cell, resulting in Jsc = 11.77 mA cm^{-2}, Voc = 2.34 V, FF = 83.0%, and PCE = 22.8%. Both approaches outperformed the unoptimized reference device (PCE = 17.2%) and surpassed reported experimental benchmarks (∼17.6%). The thickness-defect optimization alone led to a PCE gain of nearly 9%, underlining the importance of finely tuning material parameters and structure. These findings demonstrate the strong potential of all-polymer tandem solar cells for future flexible and lightweight photovoltaic applications, while offering valuable design guidelines for experimental implementation.
 [DOI: 10.1149/2162-8777/adfb2b]

Manuscript submitted June 11, 2025; revised manuscript received August 2, 2025. Published August 26, 2025.

In response to environmental challenges and the necessity of a sustainable energy transition, the development of renewable energy sources has become a global priority.[1] Among the various sources of clean energy, solar energy holds a prominent position, particularly due to advances in photovoltaic (PV) technology.[2,3] Over the past decades, the optimization of PV technologies has led to the emergence of new materials and structures aimed at enhancing solar cell efficiency while reducing manufacturing costs.[4,5]

In this context, all-polymer solar cells (all-PSCs) have emerged as a promising solution. They are distinguished by their low cost, lightweight nature, flexibility, and improved stability compared to conventional organic solar cells.[6,7] By 2022, organic tandem solar cells had reached a PCE of about 20.3%, marking a significant advancement in their performance.[6,8] However, despite these advancements, their performance remains inferior to other photovoltaic technologies, primarily due to high voltage losses (V_{loss}), which limit the open-circuit voltage (V_{OC}).[9] A promising approach to enhance their performance involves employing a tandem architecture, which enables better utilization of the solar spectrum.

Tandem architecture is an effective strategy for improving the performance of organic solar cells (OSCs). A tandem device consists of multiple stacked cells, each featuring an absorber layer with a specific energy band gap (E_g).[10,11] The top cell, characterized by a wider E_g, absorbs high-energy photons, while the bottom cell captures lower-energy photons. This configuration allows for a broader wavelength spectrum to be utilized, thereby increasing photocurrent generation compared to single-junction cells.[12,13] Furthermore, the open-circuit voltage of tandem OSCs corresponds to the sum of the V_{OC} values of the sub-cells, which can contribute to overall higher efficiency.[12]

However, despite these theoretical advantages, tandem cells have not yet demonstrated a significant gain in PCE compared to single-junction cells. One of the main challenges lies in the lack of efficient low-bandgap materials for rear cells, which limits optimal utilization of the near-infrared (NIR) spectrum.[12,14]

Recently, significant progress has been made with low-bandgap polymer acceptors (PSMAs) derived from Y6-type small-molecule acceptors (SMAs).[15] Notably, Luo et al. demonstrated that PSMAs such as PY-IT, with a bandgap of 1.4 eV, enable more balanced charge transport and a more favorable morphology.[16] When combined with the wide-bandgap donor polymer PM6, these materials achieved an efficiency of 15.05% in all-PSCs.[17] These findings pave the way for new strategies to optimize all-PSCs, particularly through refined material selection and device engineering, to fully exploit the potential of tandem architectures.

This work focuses on the study and optimization of a fully organic tandem solar cell. The reference structure, which has been studied experimentally, is as follows ITO/PEDOT:PSS/PM7:PIDT/C60/Ag/Interlayer/PEDOT:PSS/PM6:PY-IT/PDINN/Ag. The aim of this study is to improve the performance of this architecture through two complementary optimization strategies. The first approach involves adjusting the thickness of the active layers and the defect density, resulting in a power conversion efficiency (PCE) of 26%, which represents a 9% improvement over the original cell. The second strategy is based on the selection and integration of optimal charge transport materials, taking into account their electronic affinity with the active layers. This method resulted in a PCE of 22%, an increase of 6% over the reference device.

These results pave the way for new strategies to optimize all-polymer solar cells (all-PSCs), in particular through refined material selection and advanced device engineering, in order to fully exploit the potential of tandem architectures.

Modeling Framework and Structural Design of the Tandem Cell

Device modeling with SCAPS-1D software.—In this study, tandem solar cells were simulated using SCAPS-1D software. Since SCAPS-1D does not allow direct simulation of a tandem device, the two sub-cells were modeled individually. This approach is commonly used to evaluate the performance of tandem solar cells. The top sub-cell is subjected to standard AM1.5 G illumination, while the bottom sub-cell receives a filtered spectrum representing the optical behavior of the top cell. This filtered spectrum is defined by an optical transmission filter, calculated according to Eqs. 1, 2.[18–20]

$$S(\lambda) = S_0(\lambda)\cdot\exp(-\alpha_{PEDOT:PSS}d_{PEDOT:PSS})\cdot \times \exp(-\alpha_{PM7:PIDT}d_{PM7:PIDT})\cdot\exp(-\alpha_{C60}d_{C60}) \quad [1]$$

$$\alpha(E) = A\cdot\sqrt{h\nu - Eg} \quad [2]$$

This estimate does not take into account reflection losses due to thin-film interference. Figure 1 shows the filtered spectrum

[z]E-mail: samiamoulebhar@gmail.com

physica status solidi a
www.pss-a.com

Enhancing Organic Solar Cells through Dual Electron Transport Layers: A Machine Learning Approach for Prediction of Organic and Metal Oxide Electron Transport Layer Compatibility

Samia Moulebhar, Chahrazed Bendenia, Souhila Bendenia, Hanaa Merad-Dib, Sid Ahmed Khantar, and Sarra Merabet*

This research investigates the effect of incorporating dual cathode buffer layers on the performance of photovoltaic devices, focusing on ITO/PEDOT:PSS/PM6:PY-IT/PCBM/metal oxide/Ag architectures where PCBM is combined with ZnO, TiO_2, and SnO_2 as inorganic electron transport layers (ETLs). Key parameters such as film thickness, doping concentration, interfacial defects, Mott–Schottky behavior, and impedance characteristics are thoroughly analyzed. Among the tested configurations, the most efficient structure is PCBM/TiO_2, which achieves an efficiency of 19.35% with an open circuit voltage of 1.14 V and a fill factor of 73.76%. To improve device optimization, this study introduces an artificial intelligence (AI)-based approach using the SCAPS-1D simulator. This method enables accurate efficiency prediction and optimal selection of double organic/inorganic ETL combinations. Various regression models are applied, including linear regression, decision tree regressor, random forest regressor, gradient boosting regressor, XGBoost regressor, and K-neighbors regressor. Among them, XGBoost regressor shows the highest precision with R^2 (test) = 0.9957, root-mean-square error = 0.2446, and R^2 (train) = 1, highlighting the potential of AI in refining photovoltaic design.

1. Introduction

Organic solar cells (OSCs) have emerged as a promising clean and renewable energy technology, garnering significant attention due to their unique advantages, including low-cost solution-based production, lightweight design, flexibility, and semitransparency.[1,2] These attributes make OSCs highly suitable for large-scale industrial applications and integration into a variety of innovative photovoltaic devices.[3–6] For instance, the power conversion efficiency (PCE) of rigid single-junction OSCs has now surpassed 20%,[7] demonstrating their potential as a viable approach to harnessing sustainable and eco-friendly solar energy.[8,9] However, despite these achievements, the efficiency of flexible OSCs continues to lag behind their rigid counterparts, posing a significant challenge to the commercialization of this emerging technology.[10] Improving both efficiency and stability remains a critical focus for researchers aiming to unlock the full potential of flexible OSCs.[11,12]

Over the years, considerable progress has been made in the development of new active materials and the optimization of device structures and morphology, leading to remarkable advancements in PCE.[8]

Conventional OSCs typically consist of a photoactive layer sandwiched between a hole-transporting layer, such as poly(3,4ethylenedioxylenethiophene):poly (styrenesulfonic acid) (PEDOT:PSS) and a low work-function metal cathode (e.g., Ca, Al, Mg) on an indium tin oxide (ITO) substrate. However, this conventional architecture is highly sensitive to environmental factors such as moisture and oxygen, which can lead to the slow deterioration of acidic PEDOT:PSS and the oxidation of the metal cathode. These issues significantly impact the air stability and operational lifetime of the devices, highlighting the need for more robust materials and designs.[13,14]

The electron transport layer (ETL) plays a pivotal role in determining the performance of OSCs.[15] It not only enhances charge carrier extraction but also influences the morphology of the active layer, thereby affecting overall device efficiency and stability.[16,17] Existing ETL materials can be broadly categorized into three types: polymers (e.g., PFN, PEI, and PEIE), organic small molecules (e.g., PDINN and PDINO), and inorganic materials (e.g., ZnO, TiOx, and SnOx).[8] Among these, metal oxides such as zinc oxide (ZnO), titanium dioxide (TiO_2), and tin oxide (SnO_2) have gained

S. Moulebhar, C. Bendenia, S. A. Khantar, S. Merabet
Laboratory of Electromagnetism and Guided Optics
Faculty of Science and Technology ,University Abd El Hamid Ibn Badis Mostaganem 27 000, Algeria
E-mail: samia.moulebhar.etu@univ-mosta.dz

S. Moulebhar, C. Bendenia, S. Bendenia, H. Merad-Dib, S. A. Khantar, S. Merabet
Analysis, Modeling, Advanced Materials for Renewable Energies Laboratory
Faculty of Science and Technology, University Abd El Hamid Ibn Badis Mostaganem 27 000, Algeria

The ORCID identification number(s) for the author(s) of this article can be found under https://doi.org/10.1002/pssa.202500317.

DOI: 10.1002/pssa.202500317

Physica Scripta

PAPER

High-efficiency design and optimization of 2 T monolithic polymer/polymer tandem solar cells using SCAPS-1D simulations

Samia Moulebhar[1,2], **Chahrazed Bendenia**[1,2], **Souhila Bendenia**[2], **Hanaa Merad-Dib**[2], **Sid Ahmed Khantar**[1,2] **and Sarra Merabet**[1,2]

[1] Laboratory of Electromagnetism and Guided Optics, Faculty of Science and Technology University Abd El Hamid Ibn Badis, Mostaganem 27000, Algeria

[2] Analysis, Modeling,Advanced Materials for Renewable Energies Laboratory, Faculty of Science and Technology, University Abd El Hamid Ibn Badis, Mostaganem 27000, Algeria

E-mail: samiamoulebhar@gmail.com

RECEIVED
25 December 2024

REVISED
17 February 2025

ACCEPTED FOR PUBLICATION
7 March 2025

PUBLISHED
20 March 2025

Keywords: organic solar cell, tandem, performances, SCAPS 1D

Abstract

In this study, we present a novel 2 T monolithic polymer/polymer tandem solar cell (TSC) model based on experimentally validated sub-cell designs composed entirely of OSC/OSC polymers. The individual sub-cells have been calibrated against experimental data, resulting in power conversion efficiencies (PCE) of 10.33% for the front cell and 21.72% for the back cell. The lower cell contains a PM6:Y6 active layer in an ITO/Cu2O/PM6:Y6/SnO2/Ag configuration, while the upper polymer cell is designed with a conventional ITO/PEDOT:PSS/PM7:PIDT/PDINN/Ag structure, with PM7:PIDT as the absorber layer. Simulations were performed using the 1D SCAPS tool to individually optimize the performance of each sub-cell. Extensive investigation was carried out on band alignment, defect density, active layer thickness and the selection of electron and hole transport layers (ETLs and HTLs). The effects of temperature, shunt resistance and series resistance on the two sub-cells were also analyzed to improve stability and performance. The resulting tandem structure exhibited a short circuit current density (J_{SC}) of 11.685 mA cm^{-2}, an open circuit voltage (V_{OC}) of 2.0721 V, a fill factor of 82.823% and a PCE of 20.054%, positioning it as a promising candidate for flexible, green and highly efficient tandem solar cells. These results highlight the potential of our design to advance the performance benchmarks of organic tandem solar cells.

Nomenclature table with units.

Nomenclature	Meaning	Units
HTL	Hole Transport Layer	
ETL	Electron Transport Layer	
E_g	Energy Bandgap	(eV)
χ	Electron Affinity	(eV)
ε	Relative Permittivity	
N_c	Effective Density of States in Conduction Band	$(1/cm^3)$
N_v	Effective Density of States in Valence Band	$(1/cm^3)$
μ_e	Electron Mobility	$(cm^2/V{\cdot}s)$
μ_h	Hole Mobility	$(cm^2/V{\cdot}s)$
N_A	Acceptor Concentration	$(1/cm^3)$
N_d	Donor Concentration	$(1/cm^3)$
N_t	Trap Density	$(1/cm^3)$
PCE	Efficiency	(%)
J_{SC}	Short circuit density	$(mA.cm^{-2})$
FF	Fill Factor	(%)
V_{OC}	Open Circuit voltage	(V)

physica status solidi a
www.pss-a.com

Hybrid Optimization Approach Using Multiobjective Genetic Algorithm NSGA-II, SCAPS-1D Simulation, and Response Surface Methodology for Organic Solar Cell Analysis

Samia Moulebhar, Chahrazed Bendenia,* Hanaa Merad-Dib, Souhila Bendenia, Sarra Merabet, and Sid Ahmed Khantar*

In the field of simulation, it is difficult to find the relevant values for the properties of materials and in this context this approach has been proposed on optimizing the performance of organic solar cells, a promising technology in the field of renewable energy, to increase their efficiency. It adopts a hybrid approach combining the response surface methodology (RSM) with a Box–Behnken design (BBD) and the nondominated sorting genetic algorithm II (NSGA-II). The RSM BBD method is used to identify objective functions to be optimized, considering interactions between selected parameters such as the thickness of the active layer, electron-transport layer (ETL), hole-transport layer (HTL), and the doping of these layers. Concurrently, the NSGA-II genetic algorithm aims to maximize the performance of the solar cell based on these parameters. The specific importance of NSGA-II lies in its ability to solve complex multiobjective optimization problems. Indeed, NSGA-II is designed to simultaneously manage several performance objectives, which is crucial for organic solar cells. Its ability to generate a diverse set of optimal solutions enables efficient configurations to be found that may not be obvious with simpler optimization approaches. The results of this study show that optimum solar cell performance is achieved with active layer, ETL layer, and HTL layer thicknesses of 100.86, 79.9, and 20.24 nm, respectively, and active layer doping of $8.71E+21\ cm^{-3}$, HTL layer doping of $9.90E+21\ cm^{-3}$, and ETL layer doping of $9.49E+21\ cm^{-3}$. Analysis using Solar Cell Capacitance Simulator-1D (SCAPS-1D) software shows that optimum performance is achieved with these specific parameter values. After optimization with NSGA-II, the power conversion efficiency increases by 39% compared to previous work. This study provides evidence of the effectiveness of the proposed hybrid approach for optimizing the performance of organic solar cells. By showing remarkable agreement between the results obtained by NSGA-II and SCAPS-1D, this approach opens up promising prospects for the future of renewable energy.

1. Introduction

Organic solar cells (OSCs) are emerging as one of the most promising photovoltaic technologies in an era of increasingly scarce resources. Their appeal lies in several significant advantages: low cost, remarkable lightness, the ability to be printed on large surfaces, and increased flexibility.[1–3] The power conversion efficiency (PCE) of nonfullerene organic photovoltaic cells has improved significantly in recent years, rising from about 3% in 2007[4] to over 10% in 2013,[5] reaching 14% in 2018,[6] and achieving 19% in 2023.[7] These improvements have been driven by the exploration of new and varied structures aimed at overcoming the main obstacles to enhancing OSC performance.[8] Although numerous research projects have focused on the fabrication and analysis of nonfullerene bulk heterojunction organic photovoltaic cells, significant challenges remain.[9,10] A notable example is the PBDB-T:ITIC blend, which has achieved a PCE of up to 11.25%.[11] This blend consists of 3,9-bis(2-methylene-(3-(1,1-dicyanomethylene)-indanone)-5,5,11,11-tetrakis(4-hexylphenyl)-dithieno[2,3-*d*:2,3-*d*]-*s*-indaceno[1,2-*b*:5,6-*b*]dithiophene (ITIC), developed by Zhan and colleagues in 2015,[12] and is considered an ideal acceptor. Poly[(2,6-(4,8-bis(5-(2-ethylhexyl)thiophen-2-yl) benzo[1,2-*b*:4,5-*b*′]dithiophene)-*co*-(1,3-di(5-thiophene-2-yl)-5,7-bis(2-ethylhexyl)benzo[1,2-*c*:4,5-*c*′] dithiophene-4,8-dione)] (PBDB-T) serves as the electron donor.[13] However, the effects of different materials and technological parameters on OSC performance have yet to be thoroughly simulated to find optimized techniques for improving their efficiency.[10] In addition, for the same type of structure, numerous journal articles have used different parameter values, leading to varying performance outcomes. This variability has made it challenging to identify the ideal parameters for practical applications. Therefore, integrating data from a large number of articles was crucial for our work. We analyzed these articles to identify the parameters that could enhance the performance of

S. Moulebhar, C. Bendenia, H. Merad-Dib, S. Bendenia, S. Merabet, S. A. Khantar
Laboratory of Electromagnetism and Guided Optics
Faculty of Science and Technology
University Abd El Hamid Ibn Badis
Mostaganem 27000, Algeria
E-mail: samia.moulebhar.etu@univ-mosta.dz; chahrazed.bendenia@univ-mosta.dz

The ORCID identification number(s) for the author(s) of this article can be found under https://doi.org/10.1002/pssa.202400654.

DOI: 10.1002/pssa.202400654

Abstract: This thesis is set within the current context of the energy transition, where the optimization of lightweight, flexible, and low-cost photovoltaic technologies represents a major challenge. It explores organic solar cells (OSCs) through an approach that combines numerical modeling, algorithmic optimization, artificial intelligence, and experimental validation. First, a state-of-the-art review positioned OSCs among other photovoltaic technologies and identified their main challenges in terms of efficiency and stability. Then, using the **SCAPS-1D** simulator, different optimization strategies were investigated. For tandem cells, we focused on the **PM6:PY-IT** (bottom cell) and **PM7:PIDT** (top cell) systems. Adjusting the thickness and defect density of the active layers, as well as engineering the electron transport layers (ETLs), enabled us to achieve remarkable efficiencies **(PCE = 24.5% and 22.83%)**. Furthermore, we studied the engineering of transport layers in a single-junction cell based on the PM6:PY-IT absorber, where several ETL combinations were tested. Among them, the PCBM/TiO_2 configuration showed a significant improvement in charge extraction **(PCE = 19.35%, V_{OC} = 1.14 V, FF = 73.76%)**. Machine Learning models, particularly **XGBoost**, were then employed to predict the compatibility and performance of materials with high accuracy **(R^2 = 0.9957)**. Finally, a practical demonstration was carried out by integrating an OPV module into a smartphone charging system, illustrating the potential of autonomous organic photovoltaic solutions for portable electronics and embedded systems. The results highlight the relevance of a multidisciplinary approach and open up new perspectives, particularly in improving long-term stability, exploring new materials, and integrating OSCs into smart systems and large-scale applications.
Keywords: Organic Materials, Renewable energy, Embedded systems, Photovoltaic efficiency, SCAPS-1D simulation, Machine Learning.

الملخص: تندرج هذه الأطروحة في سياق التحول الطاقوي الحالي، حيث يُعد تحسين تقنيات الخلايا الكهروضوئية الخفيفة، المرنة ومنخفضة التكلفة تحدياً رئيسياً. وهي تستكشف الخلايا الشمسية العضوية **(OSCs)** من خلال مقاربة تجمع بين النمذجة العددية، والتحسين الخوارزمي، والذكاء الاصطناعي، والتحقق التجريبي.في البداية، سمح استعراض شامل بتحديد مكانة الخلايا الشمسية العضوية مقارنةً بالتقنيات الكهروضوئية الأخرى، مع إبراز التحديات الرئيسية المرتبطة بالكفاءة والاستقرار. بعد ذلك، وباستخدام برنامج **SCAPS-1D**، تم اختبار عدة استراتيجيات للتحسين. بالنسبة للخلايا ثنائية الوصلة **(Tandem)**، عملنا على أنظمة **PM6:PY-IT** (الخلية السفلية) و **PM7:PIDT** (الخلية العلوية). حيث أدى ضبط سمك وكثافة العيوب في الطبقات الفعالة، بالإضافة إلى هندسة طبقات نقل الإلكترونات (ETL)، إلى تحقيق كفاءات مميزة **PCE = 24.5%** و **22.83%**.كما درسنا هندسة طبقات النقل في خلية أحادية الوصلة تعتمد على الممتص **PM6:PY-IT**، حيث تم اختبار عدة أزواج من طبقات **ETL**. من بينها، أظهرت البنية **PCBM/TiO_2** تحسناً ملحوظاً في استخلاص الشحنات (**PCE = 19.35%**، **V_{OC} = 1.14 V**، **FF = 73.76%**). وقد تم بعد ذلك استخدام نماذج التعلم الآلي، وخاصة **XGBoost** ، للتنبؤ بتوافق وأداء المواد بدقة عالي **R^2 = 0.995** وأخيراً، تم إجراء تجربة عملية من خلال دمج وحدة كهروضوئية عضوية في نظام لشحن الهواتف الذكية، مما يبرز إمكانات الحلول الكهروضوئية العضوية المستقلة في مجال الإلكترونيات المحمولة والأنظمة المدمجة. تُظهر النتائج أهمية المقاربة متعددة التخصصات، وتفتح آفاقاً جديدة، خصوصاً فيما يتعلق بتحسين الاستقرار طويل الأمد، واستكشاف مواد جديدة، ودمج الخلايا الشمسية العضوية في الأنظمة الذكية والتطبيقات واسعة النطاق..
الكلمات الرئيسية :المواد العضوية، ا لطاقة المتجددة، الأنظمة المدمجة، الكفاءة الكهروضوئية، محاكاة SCAPS-1D

Résumé : Cette thèse s'inscrit dans le contexte actuel de la transition énergétique, où l'optimisation des technologies photovoltaïques légères, flexibles et à faible coût constitue un enjeu majeur. Elle explore les cellules solaires organiques (OSC) à travers une approche combinant modélisation numérique, optimisation algorithmique, intelligence artificielle et validation expérimentale. Dans un premier temps, un état de l'art a permis de situer les OSC parmi les autres technologies photovoltaïques et d'identifier leurs principaux défis en termes de rendement et de stabilité. Ensuite, à l'aide du simulateur **SCAPS-1D**, différentes stratégies d'optimisation ont été testées. Pour les cellules tandem, nous avons travaillé sur les systèmes **PM6:PY-IT** (cellule inférieure) et **PM7:PIDT** (cellule supérieure). L'ajustement de l'épaisseur et de la densité de défauts des couches actives, ainsi que l'ingénierie des couches de transport d'électrons (ETL), ont permis d'atteindre des rendements remarquables **(PCE = 24,5% et 22,83%)**. Par ailleurs, nous avons étudié l'ingénierie des couches de transport dans une cellule monojonction basée sur l'absorbeur **PM6:PY-IT**, où nous avons testé plusieurs couples d'ETL. Parmi eux, la configuration **PCBM/TiO_2** a montré une amélioration notable de l'extraction de charges (**PCE = 19,35%, V_{OC} = 1,14 V, FF = 73,76%)**. Des modèles de Machine Learning, notamment **XGBoost**, ont ensuite été utilisés pour prédire la compatibilité et la performance des matériaux avec une précision élevée **(R^2 = 0,9957)**. Enfin, une démonstration pratique a été réalisée en intégrant un module OPV dans un système de recharge de smartphone, illustrant le potentiel des solutions photovoltaïques organiques autonomes pour l'électronique portable et les systèmes embarqués. Les résultats obtenus mettent en évidence l'intérêt d'une approche multidisciplinaire et ouvrent de nouvelles perspectives, notamment l'amélioration de la stabilité à long terme,

l’exploration de nouveaux matériaux, et l’intégration des OSC dans des systèmes intelligents et des applications de grande échelle.

Mots-clés: Matériaux organiques, Énergie renouvelable, Systèmes embarqués, Rendement photovoltaïque Simulation SCAPS-1D, Apprentissage automatique.